RIGA TECHNICAL UNIVERSITY

Jānis Eidaks

RF POWERING OF AUTONOMOUS WIRELESS SENSOR NETWORK NODES

Doctoral Thesis

RTU Press
Riga 2022

RIGA TECHNICAL UNIVERSITY
Faculty of Electronics and Telecommunications

Jānis Eidaks
Doctoral Student of the Study Programme "Electronics"

RF POWERING OF AUTONOMOUS WIRELESS SENSOR NETWORK NODES

Doctoral Thesis

Scientific supervisors
Assoc. Professor Dr. sc. Ing.
DMITRIJS PIKULINS
Assoc. Professor Dr. sc. Ing.
ANNA LITVINENKO

RTU Press
Riga 2022

Eidaks, J. RF Powering of Autonomous Wireless

Sensor Network Nodes. Doctoral Thesis.

Riga: RTU Press, 2022. — 104 p.

Published in accordance with the decision

of the Promotion Council ”RTU P-08”

of March 4 ,2022, Minutes No. 9.

The research was partially performed within the framework and with the financial support of SAM 8.2.2. “Stiprināt augstākās izglītības institūciju akadēmisko personālu stratēģiskās specializācijas jomās” project of Riga Technical University No.8.2.2.0/18/A/017.

DOCTORAL THESIS PROPOSED TO RIGA TECHNICAL UNIVERSITY FOR THE PROMOTION TO THE SCIENTIFIC DEGREE OF DOCTOR OF SCIENCE

To be granted the scientific degree of Doctor of Science (Ph. D.), the present Doctoral Thesis has been submitted for the defence at the open meeting of RTU Promotion Council on 10th of June 2022 at the Faculty of Electronics and Telecommunications of Riga Technical University, 12 Āzenes Street, Room 201.

OFFICIAL REVIEWERS

Professor Dr. sc. ing. Vjačeslavs Bobrovs
Riga Technical University

Professor Dr.-Ing. habil. Andreas Ahrens
Hochschule Wismar, University of Applied Sciences Technology, Business and Design, Germany

Professor Dr. sc. ing Andrius Katkevičius
Vilnius Gediminas Technical University, Lithuania

DECLARATION OF ACADEMIC INTEGRITY

I hereby declare that the Doctoral Thesis submitted for the review to Riga Technical University for the promotion to the scientific degree of Doctor of Science (Ph. D.) is my own. I confirm that this Doctoral Thesis had not been submitted to any other university for the promotion to a scientific degree.

Janis Eidaks ……. (signature)
Date: ……

The Doctoral Thesis has been written in English. It consists of an Introduction, 4 chapters, Conclusions, 63 figures, 10 Tables, 3 appendices, the total number of pages is 104, including Appendices. The Bibliography contains 91 titles.

Annotation

This work is dedicated to the experimental study of RF powering of autonomous wireless sensor network nodes. The impact of powering signal properties on the RF-DC conversion efficiency and wireless power transfer performance is investigated. The impact of average input power level, peak-to-average power ratio (PAPR) level, different modulation types, signals' spectral properties, numbers of sub-carriers, and bandwidth are examined. The most popular RF-DC converter topologies and off-the-shelf solutions in the sub-GHz frequency range have been studied in detail. The study is performed in four parts: theoretical analysis of WPT technology, RF-DC converter prototyping, an experimental survey on RF-DC conversion efficiency and experimental study on WPT performance. The work results are partly developed within research projects "Radio Frequency Power Transmission for Wireless Sensor Network Use" and "Advanced Techniques for Wireless Power Transfer" and published in 13 scientific articles.

The Thesis consists of four chapters, 63 figures, 10 tables, and 3 appendices. The total number of pages is 85, not including appendices. The Bibliography contains 91 references.

Anotācija

Darbs ir veltīts autonomo bezvadu sensoru tīkla mezglu RF barošanas eksperimentālai izpētei. Tiek pētīta barošanas signāla īpašību ietekme uz RF-DC pārveidojuma efektivitāti un bezvadu jaudas pārvades (WPT) veiktspēju. Tiek pētīta vidējā ieejas jaudas līmeņa, maksimālās un vidējās jaudas attiecības (PAPR) līmeņa, dažādu modulācijas veidu, signālu spektrālo īpašību, apakšnesēju skaita, joslas platuma ietekme. Plašāk izmantotas RF-DC pārveidotāju topoloģijas, kā arī tirgū esošie risinājumi ir atlasīti pētījuma veikšanai populārākā un perspektīvāka sub-GHz frekvenču diapazonā. Pētījums tiek veikts četrās daļās: WPT tehnoloģijas teorētiskā analīze, RF-DC pārveidotāja prototipēšana, eksperimentāls pētījums par RF-DC pārveidošanas efektivitāti, eksperimentāls pētījums par WPT veiktspēju. Darba rezultāti daļēji izstrādāti pētniecības projektu "Radiofrekvenču jaudas pārraide bezvadu sensoru tīkla lietošanai", "Advancētas tehnoloģijas bezvadu enerģijas parvādei " ietveros un publicēti 13 zinātniskajos rakstos.

Darbs sastāv no četrām nodaļām, 63 attēliem, 10 tabulām, 3 pielikumiem. Kopējais lappušu skaits ir 85, neskaitot pielikumus. Bibliogrāfija satur 91 atsauci.

Contents

LIST OF TABLES 10
List of Abbreviations 11
Introduction 12
1. Theoretical analysis of WPT technology 20
1.1. WPT techniques 20
1.2. Overview of RF WPT studies 22
1.3. Conclusions on theoretical analysis of WPT technology 26
2. RF-DC circuit prototyping 27
2.1. Model development and simulation 27
2.2. Modelling 30
2.3. Measurements of rectifier's input impedance 35
2.4. Conclusions on RF-DC circuit prototyping 38
3. Experimental study on RF-DC conversion efficiency 39
3.1. Signal waveform impact on the power conversion efficiency 45
3.1.1. Objective 45
3.1.2. Tasks 45
3.1.3. Measurement setup and experiments 46
3.1.4. Experimental results 47
3.1.5. Summary of the signal waveform impact on the power conversion efficiency 51
3.2. Impact of the number of multitone signal subcarriers on power conversion efficiency 51
3.2.1. Objective 51
3.2.2. Tasks 51
3.2.3. Measurement setup 51
3.2.4. Experimental results 52
3.2.5. Summary of impact of the number of multitone signal subcarriers on the power conversion efficiency 59
3.3. Matching network impact on the RF-DC conversion efficiency 60
3.3.1. Objective 60
3.3.2. Tasks 60
3.3.3. Measurement setup and experiments 60
3.3.4. Experimental results 60

3.3.5. Summary of impact of matching network on the RF-DC conversion efficiency 66
3.4. Conclusions on experimental study on RF-DC conversion efficiency 66
4. Experimental study on WPT performance 68
4.1. MEASUREMENT SETUP 68
4.2. Study of the factors influencing the WPT efficiency 69
4.2.1. Signal frequency impact on the WPT efficiency. 70
4.2.2 Signal waveform impact on the WPT efficiency 72
4.2.3. Impact of constant envelope signal waveform on the WPT efficiency..... 75
4.3. Conclusions of experimental study on WPT performance..... 77
Conclusions 79
Bibliography..... 80
Annex 1. 86
Annex 2. 99
Annex 3. 102

LIST OF TABLES

Table 1.1 Comparison of Different RF-DC Rectifier Topologies…….23
Table 2.1 High-frequency RF diode SPICE parameters ……...28
Table 2.2 RF-DC Voltage Doubler with the Matching Network Simulation Parameters..30
Table 3.1 Characteristics of the Employed Signal ……39
Table 3.2 RF signal parameters ……41
Table 3.3 Parameters of Experimental RF-DC Rectifiers ……43
Table 3.4 RF Signal Parameters ……46
Table 3.5 RF-DC Rectifier Frequency Characterization Parameters ……46
Table 3.6 RF Signal Parameters…… 52
Table 3.7. Mean squared difference of the rectified voltage with different signal waveforms ……54
Table 3.8. RF-DC voltage doubler with the matching network peak voltage and power parameters depending on the load resistance. …….. 59
Table 3.6 RF Signal Parameters ……60

List of Abbreviations

Abbreviation	Explanation
ADS	advanced design system
CHIRP	sweep signal with periodic linearly increasing frequency
DC	direct current
EH	energy harvesting
EM	electromagnetic
EOL	end-of-life
FM	frequency modulation
HBM	harmonic balance method
HPAPR	high PAPR
IFFT	inverse fast Fourier transform
IoT	Internet of Things
LPAPR	low PAPR
NB-IoT	narrow-band Internet of Things
PAPR	peak-to-average power ratio
PCB	printed circuit board
PSMU	power source measure unit
RF	radio-frequency
RPAPR	random PAPR
SDR	software-defined radio
SN	sensor node
USB	universal serial bus
USRP	universal software radio peripheral
VNA	vector network analyzer
WPT	wireless power transfer
WSN	wireless sensor network

Introduction

Relevance

In this millennium, we are slowly entering the age where smartphones, smart appliances, houses, environment, transportation, medicinal and welfare, infrastructure, and supply chains are becoming more entwined in our lives regardless of our choice. Big data and machine learning make our lives more convenient, and predictable and make data-based probabilistic choices to provide continuity to our fast-paced lives. The information around us is overwhelming, and all kinds of devices are used to collect data around us and give us control of our environment and schedule and even remotely control it. The ability to do so is achieved by employing wired and wireless sensor network devices connected to the internet, the so-called IoT devices, or other devices that use gateway devices to send data through the ethernet. Useful and green lifestyle features of smart houses include smart heating, which can be adapted to the user's work schedule and decrease the temperature when no one is at home, smart lighting that switches off to reduce lighting when no people in are detected, automated motorized curtain and motorized window opener devices, that are performing depending on the weather conditions.

Electronic voice assistant devices have been developed to perform tasks directly and control household devices in the last decade. These and other similar devices are used around us. Some work with the same wireless information transfer protocol and form a wireless sensor network (WSN). The devices that create such networks are called WSN devices. The powering of such WSN devices varies. Some of these devices that serve as a gateway are power-hungry and some devices that consume very little power. The devices occasionally wake to perform some tasks or send data while being in a deep sleep state the rest of the time. Therefore, the operation from the primary power sources batteries, can be maintained for a long time. However, as the number of such devices increases rapidly and generally consumes little power, a more relevant issue is the replacement of the depleted energy source. The battery replacement could be unfeasible if the device is placed in hard-to-reach places or is embedded in the building and has become an integral part of it. The trend of the WSN device use in everyday life is increasing every year, and these devices' convenience is undeniable. Therefore, one of the problems that should be addressed is the sustainable power solution for such devices and prolonging the operation time without expensive and time-consuming battery replacement operations, as the number of such devices is expected only to increase [1].

Historically, low-power WSN devices are powered using non-rechargeable or chargeable batteries. This provides a solid amount of power that can be considered while calculating the device's lifetime and/or planning the battery replacement. Nowadays, there are other power solutions other than single-use or rechargeable batteries, for example, that take the environment's energy and convert it to DC power. Next, there is a list of alternative power sources from the environment that can be converted to electricity:

- vibration energy,
- heat energy,
- wind energy,

- light energy,
- radiofrequency energy.

Of the mentioned power sources, few are not controllable. They may vary in the intensity of the received and converted energy depending on the time of day, month and year, or even not be available for a long time, therefore unpredictable. The ambient radiofrequency power harvesting amount of the mentioned energy sources in the environment depends on multiple factors, such as the density of the surrounding transceiver devices, the average radiated power levels, and the directivity.

The harvestable energy power levels from sources such as heat, wind, and light depend on the weather conditions in outdoor locations and the building environment control algorithm in indoor areas. The harvestable energy from the ambient radiofrequency sources is limited. So is the harvested energy from the light, wind, and the operating conditions indoors regarding the lighting schedule, heating, and ventilation/air conditioning settings. The energy harvested from the vibration energy is dependable on the conditions such as the amplitude of vibrations, acceleration, etc. There is limited ability to regulate the energy amount from the available environment energy sources, and therefore, they are not flexible. Thus, to provide a continuous operation of the device, multiple design choices have to be made: either over-engineer the ambient energy harvesting device that will work in even the worst operation conditions or select a different path: use a steerable energy source to provide and transfer energy wirelessly for the WSN nodes and make energy conversion at the WSN node side.

One of the possibilities of a steerable and controllable energy source is to use wireless power transfer. The wireless power transfer is divided into multiple subtypes, such as electromagnetic (EM) radiation, magnetic resonance, electrical resonance, or electromagnetic induction methods [2], [3]. Of the mentioned methods, the technique that can provide the most considerable WPT distance is the electromagnetic radiation method. Multiple experiments have been performed, and the corresponding scientific papers have been published on the effects of different signal parameters on WPT performance. However, available measurements and the resulting conclusions in some studies are contradictory. They cover only some of the signal parameter impact on the RF-DC power conversion and the converted power from the WPT. Therefore, the research on the signal parameter and waveform impact on the RF-DC power conversion efficiency has yet to be fully explored. There are optimal signal parameters that yield a higher power conversion efficiency with the specified RF-DC converter topology and in the WPT experiments under certain conditions. Therefore, the Thesis is dedicated to the investigation of the signal parameter impact on the RF-DC power conversion and the harvested and converted power with the WPT. As most studies are dedicated to the exploration of RF-DC power conversion with two diode rectifier topologies, this research also reviews this topology.

Research goals and tasks

The main objective of this work is to explore the RF signal parameter impact on the RF-DC power conversion efficiency and the wireless power transfer performance.

The following tasks have been set to reach the defined objective:

1. To develop the RF-DC rectifier models, and provide state-of-the-art analysis and optimisation of the model's parameters.

2. To design and fabricate prototypes for different RF-DC converter solutions.

3. To perform an experimental study on the RF-DC power conversion efficiency of the developed RF-DC converter modules, depending on the RF signal parameters.

4. To perform an experimental study on the wireless power transfer performance of the developed RF-DC converter modules depending on the RF signal parameters.

5. To perform an experimental study on the impact of wireless transmission channels on wireless power transfer performance with different RF-DC power converters.

Scientific novelty and the main results

The results obtained during the investigation are as follows:

- Optimized RF-DC converter models in Advanced Design Simulation (ADS) software have been created.
- The applicability of signals commonly used in communications to efficient RF-DC power conversion and wireless power transfer have been verified.
- RF-DC converter prototypes (voltage doubler topology with matching network, voltage doubler topology without matching network, RF-DC converter based on Powercast P2110B module) have been manufactured.
- A software-defined radio model in MATLAB/SIMULINK environment for RF signal generation has been created. The following signals were implemented:
    - FM tonal modulation;
    - CHIRP;
    - multitone signal with high PAPR level (same subcarrier amplitudes and phases);
    - multitone signal with low PAPR level (same subcarrier amplitudes, specifically selected phases);
    - multitone signal with random PAPR level (subcarrier amplitudes and phases are randomly chosen with the same random seed generator).
- Automated scripts for input signal power level, RF-DC converted DC voltage level measurements in MATLAB/SIMULINK environment, have been created employing selected hardware:
    - software-defined radio, Ettus USRP B210;
    - signal generator for specific measurements, Rohde & Schwarz R&S®SMC100A;
    - digital oscilloscope Tektronix 72004C;
    - universal power and measurement unit Keysight B2901A.
- Participation in the feasibility study for the scientific projects “Radio Frequency Power Transmission for Wireless Sensor Network Use” and “Advanced Techniques for Wireless Power Transfer”.

Theses for defence

In this promotion work, the following theses are proposed and put to defence:

1. The appropriate adjustment of the resistance load of voltage doubler converter to the number of subcarriers, in case of equal synphase multitone signals with uniformly distributed 32–256 subcarriers in the ISM 863–870 MHz frequency range, leads to the maximal RF-DC power conversion efficiency.
2. The exclusion of the matching network for the voltage doubler in the ISM 863-870 MHz frequency range, applying equal synphase multitone signals with uniformly distributed 32–256 subcarriers, increases the RF-DC power conversion efficiency up to 2 times.
3. CHIRP signals, tonally modulated FM, and the amplitude modulated signals with 4–256 subcarriers and PAPR level below 10dB in the ISM 863-870 MHz frequency range in case of the voltage doubler converter provides equal power conversion efficiency with the average squared voltage deviation for the converted voltage up to 2.5%.
4. The application of the CHIRP, FM tonally modulated, and the amplitude modulated signals with 4–256 subcarriers and PAPR level below 10dB to wireless power transfer and RF-DC conversion with voltage doubler in the case of the direct line of sight for distance range 1.7–8.7 wavelengths in the ISM 863–870 MHz frequency range ensures the same WPT performance as a sine signal with the average squared output voltage deviation of 4.5 %.

The research methodology

In order to reach the set goals, the research methodology consists of the current state-of-the-art analysis on the topic, simulation in the ADS environment, the manufacturing of the RF-DC converters, and the measurements of the RF-DC converters depending on various signal parameters.

The literature analysis is focused on 4 RF-DC conversion-related research directions:

- RF-DC power conversion efficiency depending on the signal frequency characteristics;
- RF-DC power conversion efficiency depending on the signal waveforms and envelope type;
- RF-DC power conversion efficiency depending on the input signal power level;
- Different RF-DC power conversion topologies.

The measurements include investigating the different signal parameters (signal input power level, signal bandwidth, number of subcarriers, signal waveform) impact on the power conversion efficiency of the manufactured RF-DC power converters and off-the-shelf available RF-DC power converter module.

The research objects

The research objects in this Thesis are the RF-DC power conversion efficiency and WPT performance of different RF-DC power converter implementations.

Practical application of the research

The results obtained in the experiments show the correlation of impact of different signal parameters on the RF-DC power conversion efficiency and allow the selection of the suitable

signal parameters to achieve maximum power conversion efficiency and evaluation of the obtained energy using selected RF-DC power converters.
The results of these measurements are included in the feasibility study for scientific projects “Radio Frequency Power Transmission for Wireless Sensor Network Use” and “Advanced Techniques for Wireless Power Transfer”.

Approbation

The results of the research are presented in 13 scientific papers, which have been published in the following conference proceedings and journals:

1. Litvinenko, J. Eidaks, and A. Aboltins, "Usage of Signals with a High PAPR Level for Efficient Wireless Power Transfer," 2018 IEEE 6th Workshop on Advances in Information, Electronic and Electrical Engineering (AIEEE), 2018, pp. 1–5, DOI: 10.1109/AIEEE.2018.8592043.
2. Litvinenko, J. Eidaks, S. Tjukovs, D. Pikulins, and A. Aboltins, "Experimental Study of the Impact of Waveforms on the Efficiency of RF-to-DC Conversion Using a Classical Voltage Doubler Circuit," 2018 Advances in Wireless and Optical Communications (RTUWO), 2018, pp. 257–262, DOI: 10.1109/RTUWO.2018.8587907.
3. S. Tjukovs, J. Eidaks, and D. Pikulins, "Experimental Verification of Wireless Power Transfer Ability to Sustain the Operation of LoRaWAN Based Wireless Sensor Node," 2018 Advances in Wireless and Optical Communications (RTUWO), 2018, pp. 83–88, DOI: 10.1109/RTUWO.2018.8587790.
4. J. Eidaks, A. Litvinenko, A. Aboltins, and D. Pikulins. (2019). Waveform Impact on Wireless Power transfer performance using Low-Power Harvesting Devices. Electrical, Control and Communication Engineering,15(2), 96–103. https://doi.org/10.2478/ecce-2019-0013.
5. J. Eidaks, A. Litvinenko, D. Pikulins, and S. Tjukovs, "The Impact of PAPR on the Wireless Power Transfer in IoT Applications," 2019 29th International Conference Radioelektronika (RADIOELEKTRONIKA), 2019, pp. 1–5, DOI: 10.1109/RADIOELEK.2019.8733534.
6. J. Eidaks, A. Litvinenko, J. P. Chiriyankandath, M. A. Varghese, D. D. Shah, and Y. K. T. Prathakota, "Impact of signal waveform on RF-harvesting device performance in wireless sensor network," 2019 IEEE 60th International Scientific Conference on Power and Electrical Engineering of Riga Technical University (RTUCON), 2019, pp. 1–5, DOI: 10.1109/RTUCON48111.2019.8982294.
7. J. Eidaks, A. Litvinenko, A. Aboltins, and D. Pikulins, "Signal Waveform Impact on Efficiency of Low Power Harvesting Devices in WSN," 2019 IEEE Microwave Theory and Techniques in Wireless Communications (MTTW), 2019, pp. 57–61, DOI: 10.1109/MTTW.2019.8897262.
8. S. Tjukovs, A. Litvinenko, D. Pikulins, A. Aboltins, and J. Eidaks, "Waveforms Impact on Performance of Prefabricated Energy Harvesting Device," 2019 IEEE Microwave Theory and Techniques in Wireless Communications (MTTW), 2019, pp. 62–67, DOI: 10.1109/MTTW.2019.8897230.

9. J. Eidaks, J. Sadovskis, A. Litvinenko, and D. Pikulins, "Experimental Analysis of LoRa Signals Employment for RF Energy Harvesting," 2020 IEEE Microwave Theory and Techniques in Wireless Communications (MTTW), 2020, pp. 201–205, DOI: 10.1109/MTTW51045.2020.9245073.
10. Litvinenko, R. Kusnins, A. Aboltins, J. Eidaks, D. Laksis, and J. Sadovksis, "About Simultaneous Information and Power Transfer in WSN using Frequency Modulation," 2020 IEEE 8th Workshop on Advances in Information, Electronic and Electrical Engineering (AIEEE), 2021, pp. 1–6, DOI: 10.1109/AIEEE51419.2021.9435778.
11. Eidaks, J., Kušņins, R., Laksis, D., Babajans, R., Litviņenko, A. "Signal Waveform Impact on RF-DC Conversion Efficiency for Different Energy Harvesting Circuits". 2021 2021 IEEE Workshop on Microwave Theory and Techniques in Wireless Communications (MTTW 2021): Conference Proceedings, Latvia, Riga, 7–8 October 2021. Piscataway: IEEE, 2021, pp.1–6. ISBN 978-1-6654-2470-7. e-ISBN 978-1-6654-2469-1. Available from: DOI:10.1109/MTTW53539.2021.9607090
12. Eidaks, J., Kušņins, R., Babajans, R., Čirjuļina, D., Semeņako, J., Litviņenko, A. "Fast and Accurate Approach to RF-DC Conversion Efficiency Estimation for Multi-Tone Signals". Sensors, 2022, Vol. 22, No. 3, Article number 787. ISSN 1424-8220. Available from: DOI:10.3390/s22030787
13. Kušņins, R., Babajans, R., Eidaks, J., Čirjuļina, D., Litviņenko, A. " Performance Estimation for RF Wireless Power Transfer Under Real-Life Scenario " 2022 IEEE 21st Mediterranean Electrotechnical Conference (MELECON). Submitted.

The author of the Thesis has presented the research results at the following international scientific conferences:

1. “2018 IEEE 6th Workshop on Advances in Information, Electronic and Electrical Engineering (AIEEE)”, Lithuania, Vilnius, 8–10 November 2018.
2. Riga Technical University 60th International Scientific conference (Section electronics), Latvia, Riga, 26 April 2019.
3. “29th International Conference Radioelektronika 2019”, Czech Republic, Pardubice, 16–18 April 2019.
4. “MTTW 2019: IEEE Workshop on Microwave Theory and Techniques in Wireless Communications 2019”, Latvia, Riga, 1–2. October 2019.
5. “2019 IEEE 60th International Scientific Conference on Power and Electrical Engineering of Riga Technical University (RTUCON)”, Latvia, Riga, 7–9 October 2019.
6. “MTTW 2020: IEEE Workshop on Microwave Theory and Techniques in Wireless Communications 2020”, Latvia, Riga, 1–2 October 2020.
7. “2021 IEEE 6th Workshop on Advances in Information, Electronic and Electrical Engineering (AIEEE)”, Lithuania, Vilnius, 22–24 April 2021.

Thesis structure

The thesis consists of an introduction, four chapters, conclusions, and 3 annexes, with a total number of pages 104.

The Introduction is dedicated to setting the goals and tasks required to achieve the research objective, the proposed theses, and the possible application of the achieved results.

Chapter 1 is dedicated to a short theoretical overview of WPT technology.

Chapter 2 is dedicated to the RF-DC converter parameter modelling and detection of the converter's optimal parameters for achieving the maximum power conversion efficiency impacted by the converter's component values.

Chapter 3 is devoted to the investigation of the impact of different signal parameters on the RF-DC converter performance. This research direction is further divided into several sub-topics:

- impact of the signal waveform on the power conversion efficiency;
- impact of the number of the multitone signal subcarriers on the power conversion efficiency;
- impact of the matching network on the RF-DC conversion efficiency;
- impact of the signal waveform on the WPT performance.

Chapter 4 is dedicated to the study of wireless power transfer and the impact of the channel and different signal waveforms on its performance. In this study, various rectifier boards are used, and the received WPT RF signal average input power and converted RF-DC power are analysed.

The Conclusions are summarising the RF-DC and WPT performance results and the corresponding trends observed from the experiments.

The research is divided into multiple steps, as shown in Fig.1.1. The first step is the theoretical analysis of the available solutions for the RF-DC converters. The next step is the prototyping step, where the RF-DC rectifier PCB is modelled, and the circuit parameter impact on power conversion efficiency is carried out. The third step is the RF-DC power conversion efficiency study, where the RF-DC converter performance is evaluated with different signals' parameters. The fourth step is the WPT performance study, where the RF-DC converters are evaluated in the wireless power transfer experiments.

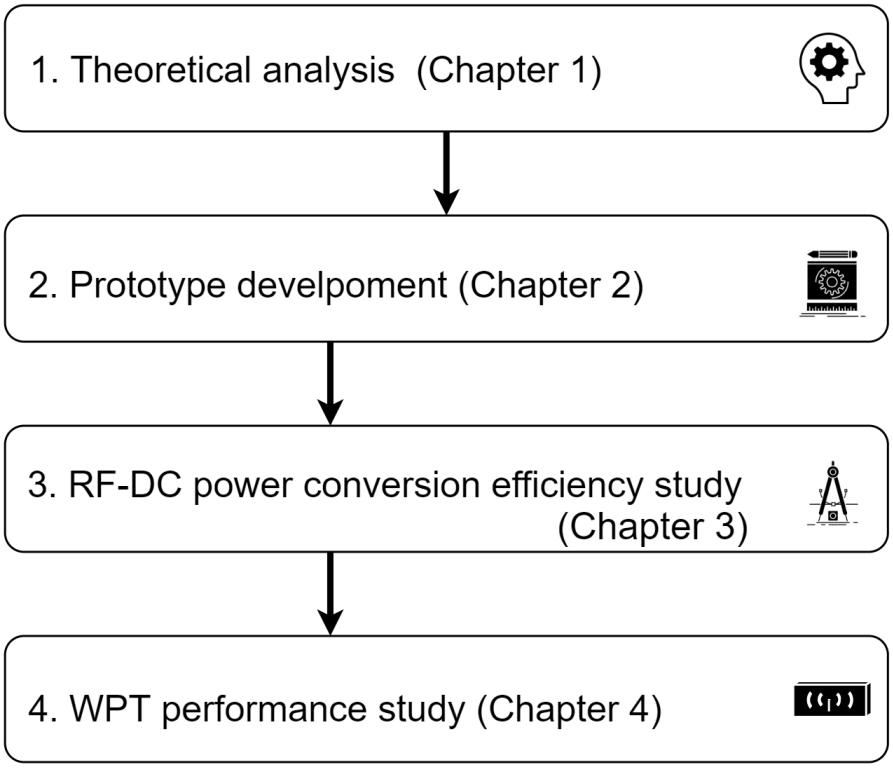

Fig. 1.1. The research step block scheme.

1. Theoretical analysis of WPT technology

Over the years, there has been a persistent trend toward smart environments such as smart homes [4], cars, cities [5], forestry, agriculture, and manufacturing. The facilitation of this trend is done by using different kinds of smart devices, low power sensors and wireless sensor networks, and wireless sensor network nodes [1], [6] [7]. The technology allows automation, smart and efficient resource usage, remote monitoring [8], and control [9], which is facilitated using IoT, 3G/4G/5G LORA/Sigfox gateways, and data aggregators and other devices. Multiple numbers of these technologies are used in conjunction to provide the necessary functionality in areas such as industrial, medical and welfare [10], traffic and logistics [11], infrastructure [12], life, and entertainment sectors.

The need for a sustainable energy source for powering wireless sensor nodes and sensors has become more relevant as the proliferation of these devices has increased over the years and is projected to increase even more over the years [1], [13]. The powering solutions may differ for small-scale sensor network nodes and include multiple options, but they usually are powered by batteries. For large-scale WSN nodes, the power solution that employs batteries may become unfeasible. The maintenance costs and the difficulties of accessing the device in hard-to-reach places and changing batteries can be even more challenging. The additional hardware required for the battery monitoring and the corresponding messaging over the WSN will also drain the power source. This, in turn, may cause the operation of the WSN network devices to switch off the network prematurely before the devices' end-of-life (EOL) and stop providing the necessary functionality. One of the solutions to provide energy to the WSN nodes over the distance independently of the environmental conditions is to employ wireless power transfer (WPT). This solution enables the WSN nodes to have a steady supply of energy and eliminates the use of batteries – therefore, also battery recycling. Depending on the conditions and the placement of the WSN nodes, under specified conditions, it is also possible for the WSN node to use ambient RF signal harvesting.

1.1. WPT techniques

The frequency range of the signal employed for the RF energy harvesting in the form of an electromagnetic radiation is 3 kHz to 300 GHz [14]. The RF energy transfer and harvesting can be divided into multiple groups depending on the properties, i.e., it can be characterized depending on the field region:

1) Near field region, where the systems load impedance of the receiver's sides affects the load impedance of the transmitter's sides [3], which can be classified into two groups:
    a. inductive power transfer and magnetically coupled resonance WPT, where the energy is transferred using the magnetic field generated from the current flowing through the transmitter coil to the receiver coil [15], schematically shown in Fig. 1.2 a),

b. capacitive power transfer, where the energy is transferred through the so-called displacement current through the capacitors [3], [15], schematically shown in Fig. 1.2 b),

2) The far-field region, where the system's load impedance of the receiver's sides does not affect the load impedance of the transmitter's sides [3], electromagnetic radiative radiation, schematically shown in Fig. 1.2 c).

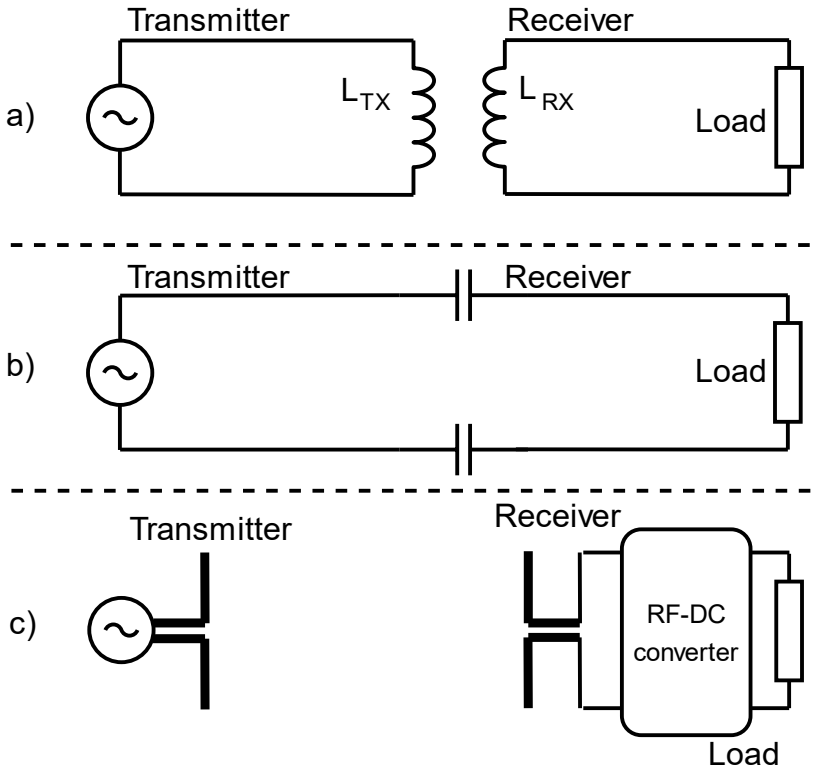

Fig. 1.2. The RF energy transfer methods schematic: a) near-field inductive power transfer, b) near-field capacitive power transfer, c) far-field electromagnetic radiation energy transfer.

The efficiency of the near-field WPT systems can reach more than 90% with the distances between the transmitter and receiver from a few millimetres up to a few centimetres [15]. The efficiency of the far-field WPT systems achieves much lower power conversion efficiency and is dependent on the distance, the antenna gains and the transmitter power level. Due to the limited distance that the near field WPT systems can power the receiver side, these systems will not be reviewed further. Therefore, the WPT system, which employs electromagnetic radiation for energy transfer, will be reviewed. The WPT system block diagram is shown in Fig 1.3.

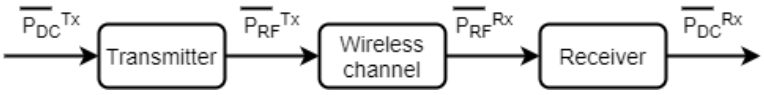

Fig. 1.3. The block diagram of the WPT system.

The WPT system consists of 3 different power conversion subsystems: energy transmitter, wireless channel, and energy receiver. In this system, power conversion is implemented as follows:

- the DC power is converted to the RF signal power, where the conversion efficiency is defined as η_1;
- the RF power is further transferred to the wireless channel and received at the energy receiver; this conversion efficiency is denoted as η_2;
- finally, the received RF power is converted from the RF signal to the DC power, characterized by another conversion efficiency η_3.

$$\eta_{\Pi} = \eta_1 \cdot \eta_2 \cdot \eta_3 \tag{1.1}$$

The overall efficiency of WPT can be expressed with the efficiencies of these three main components:

$$\eta_1 = \frac{\overline{P}_{RF}^{Tx}}{\overline{P}_{DC}^{Tx}}, \cdot \eta_2 = \frac{\overline{P}_{RF}^{Rx}}{\overline{P}_{RF}^{Tx}}, \eta_3 = \frac{\overline{P}_{DC}^{Rx}}{\overline{P}_{RF}^{Rx}}, \tag{1.2}$$

where η_{Π} – total efficiency of the WPT system; η_1 is efficiency of the transmitter; η_2 is efficiency of the wireless channel; and η_3 is efficiency of the receiver.

Equations (1.1)- (1.2) and Fig. 1.3 show that maximizing of the total efficiency η_{Π} requires maximizing of η_1, η_2, and η_3 combined, as the total efficiency depends on them.

1.2. Overview of RF WPT studies

This study will focus on RF-DC conversion efficiency and WPT performance consisting of wireless channel energy transfer efficiency and RF-DC conversion efficiency.

In free space, where are no other objects - only the transmitter and the receiver, the average received power level can be approximately determined using the Friis transmission equation. However, this equation is no longer valid in real-life situations where objects are around. The wireless channel is generally defined by path loss, multipath fading, and Doppler spread (or Doppler spectrum). All these characteristics are highly dependent on the physical environment between the transmitter and receiver and the system's parameters: antenna heights, beamwidths, polarization, and the distance between the antennas - the receiver and transmitter.

For the WPT and energy harvesting, one of the most important parts is the rectifier in conjunction with the antenna, also called the rectenna. The function of the rectenna is to convert the RF power signal to DC voltage for low power sensors and/or DC/DC converters for additional voltage boosting for sensors that require higher DC voltage. The performance of the rectenna and the distance between the transmitter and rectenna will also impact the converted power level and will affect the operation of the device. To perform efficient energy transfer or to create an accurate WPT model for the rectenna, the following considerations must be taken into account:

- the topology of RF-DC converter;
- the signal frequency;
- signal wavefrom;

- input power level.

Table 1.1

Comparison of Different RF-DC Rectifier Topologies [16].

Ref.	Substrate	RF–DC Topology	Frequency, GHz	RF Input Power, dBm	Waveform	PCE, %
[17]	-	1 diode	24	27	Single-tone [1]	43.6
				16		42.9
[18]	Custom [3]	4 diodes	5.8	30	Single-tone	92.8
[19]	FR4	2 diodes	5.76	20	Single-tone	84
[20]	RT/Duroid 5870	1 diode	5.8	16.9	Single-tone	82.7
			2.45	19.5		84.4
[21]	Custom [4]	1 diode	2.45	37	Single-tone	91
[22]	FR4	2 diodes	2.45	24.7	Single-tone	78
[23]	RO4003C	1 diode	2.45	3	Multi-tone [2]	54.5
[24]	FR4	4 diodes	2.4	27	Multi-tone	75
[25]	PTFE	4 diodes	2.4	26.2	Single-tone	80
[26]	FR4	2 diodes	2.4	22	Single-tone	82.3
[24]	RO4003C	1 diode	2.4	10	Single-tone	60
[27]	-	1 diode	2.4	−10	Multi-tone	42
[28]	FR4	4 diodes	2.15	0	Single-tone	70
[29]	Arlon A25N	1 diode	0.915	0	Multi-tone	67.8
[30]	RT/Duroid 5880	2 diodes	0.86	−4	Single-tone	60
[31]	-	1 diode	0.433	−10	Multi-tone	55

[1] All instances of "single-tone" refer to an unmodulated carrier.

[2] All instances of "multi-tone" refer to a sum of several subcarriers.

[3] Relative permittivity $\varepsilon_r = 3.4$, the dielectric loss tangent $\tan\delta = 0.0015$.

[4] Relative permittivity $\varepsilon_r = 2.55$, the dielectric loss tangent $\tan\delta = 0.0018$ [16].

The key properties of the proposed rectennas ordered by frequencies and input powers as well as topology, powering signals, and obtained conversion efficiency are summarized in Table 1.1 [16]. Multiple RF-DC rectenna measurements with the specified topology shows very high-power conversion efficiency, above 70% with a relatively high input power level above 15 dBm [18] –[22], [32] –[26]. In order to achieve such input power level at the RF-DC rectifier input, the transmitter side should generate a power level of two to three magnitudes higher, and even more, if the distance is increased, it would exceed the allowed specified effective isotropic radiated power (E.I.R.P.).

Some of the RF-DC topologies [18], [21] optimized for high input power level operation with GaAs diodes as rectifier diodes manage to achieve the power conversion efficiency that exceeds 90%. However, the specified input power level is not suitable for use in WSN nodes, as the transmitter E.I.R.P. exceeds the transmitter power regulation limit.

The use of input power in the range around 0 dBm implies the application of both sensor node and low-power technologies, such as RFID and E-ink [33], [34]. This range of input RF power was less frequently addressed in literature than high and low (<−15 dBm) power ranges. Comparing rectennas in terms of frequency, Table 1.1 demonstrates that rectennas were mainly developed for the 2.45 GHz ISM frequency band. The use of high frequency also limits the effective distance between the transmitter and the SN. Sub-GHz ranges, such as 433 MHz (ISM) and 860 MHz (GSM-850), allow the power transfer to greater distances [16].

Most of the reviewed studies use the sine wave signal as the input signal for the RF-DC rectifiers. However, some of the studies, such as [32], [27], [31], [35], [36], [37], [38], [39], revealed that the power conversion with the multitone signal yielded a higher percentage of efficiency than with the sine wave.

The topology of the RF-DC circuit is another crucial parameter of rectenna design. The topologies of the reviewed scientific papers revealed the most used topologies: one-diode-based (half-wave rectifier), two-diode-based (voltage doubler), and four-diode-based (diode bridge rectifier) topologies shown in Fig. 1.4. These topologies with slight variations were used in the studies listed in Table 1.1 [16]. After reviewing the power conversion efficiency performance of the rectifiers shown in Table 1.1, it can be concluded that a rectenna based on a voltage doubler RF-DC converter working at a sub-GHz frequency and multi-tone power-carrying signals proved to be the most well-balanced solution in terms of cost and efficiency for RF WPT applications targeted at powering SN and low power electronics [16].

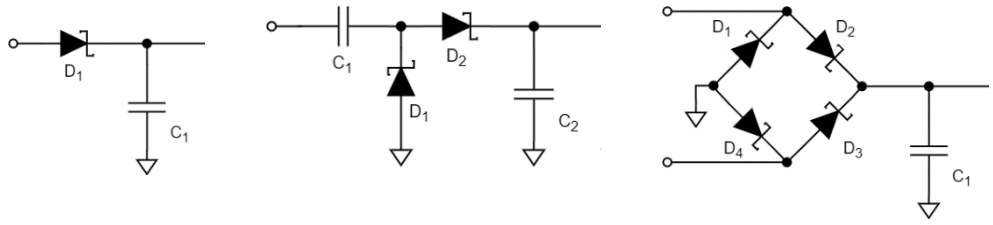

a) **b**) **c**)

Fig. 1.4. RF-DC rectifier topologies: single diode rectifier a), two-diode voltage doubler rectifier b), 4 diode bridge rectifier c) [16].

The studies reviewed were mainly focused on improving the performance of rectennas with experimental verification of the results to develop robust theoretical models for WPT and RF-DC converters. In the field of AC-DC [40] and DC-DC [41],[42]converters, various theoretical models have been developed. Several modelling approaches have also been proposed for RF-DC circuit precise simulations. Developing an accurate simulation model is a feasible alternative to experimental studies of RF-DC power converters, proposing a more convenient and cost-effective methodology, not requiring the fabrication of physical prototypes, especially when circuit design optimization is required.

The comprehensive analysis of non-linear circuits not amenable to linearization is usually a time-consuming and complicated task, despite recent advances. The application of complex input signals makes the issue even more pronounced. The inherent long transients of RF-DC converters make one of the most robust circuit analysis methods transient analysis (TA) [43] unsuitable due to disproportionally long simulation times [44]. Furthermore, a vast number of iterations is required in the case of narrow-band signals with periodic envelopes, as the simulation step must be much smaller in comparison to the period of the carrier wave. Despite the study results on speeding up the TA [45], the mentioned restriction on the simulation step size intrinsically limits the method's performance. The Volterra series method [46] is another widely used non-linear circuit analysis methodology. The method's main disadvantage is a prolonged convergence rate for circuits with highly pronounced non-linearity. The harmonic balance (HB) method was initially proposed in [47] to solve problems in mechanical engineering. Subsequently, it has been adapted to deal with various non-linear circuits under sinusoidal excitation [48]. The HB method allows computing the steady-state response directly, involving solving a system of non-linear equations [49], thus eliminating the issue of significant transient times. Another approach is based on the preliminary partitioning of the original system into linear and non-linear parts [50]. The resulting non-linear equations can be solved, e.g., utilizing Newton's method (NM) [51] or iteration relaxation method (IRM) [52],[53]. It has been shown that the evaluation of the Jacobian matrix for NM can be significantly accelerated using FFT algorithms [54]. The convergence at high input power levels could be ensured through the continuation method [55]. The multi-tone input signals could be handled by employing modified HB [56], [57]. However, a significant rise in computational burden is observed due to the necessity of calculating large Jacobian matrixes. One of the studies [58] shows how to mitigate the mentioned issue by exploiting the useful properties of multidimensional FFT algorithms. Recently, this approach has been successfully applied to a variety of applications, including autonomous and non-autonomous oscillators [59], [60], [61]. To reduce the simulation time even further, numerous variations of the HB have been proposed, namely: the hierarchical harmonic balance method [62], parallel versions of the HB [63], [64], the multi-level frequency decomposition-based HB [65], and the graph sparsification based HB [66].

Despite the methods' accuracy, their application is still resource and time-demanding. This led to the development of approximate closed-form expression-based models, applied to the analysis of rectennas sharing a common load [67], single diode rectifiers [68], [69], and Class-F rectifier converters. The simulations of the SPICE model, based on the parameters obtained

from experimental data through curve fitting, demonstrated the PCE up to 90% for the input power range of 30–35 dBm at 2.4 GHz [21]. Comparable results have been obtained in [70] for a single diode rectifier using an analytical model, including the transmission line effect. An approximate model was used in [71] to find PCE for multi-tone excitation with equally spaced frequencies. It has been proven that most analytical models, not taking into account the nonlinearity of the diodes and the possible influence of the PCB, give highly inaccurate results that are not sufficient for precise evaluation and circuit optimization [72].

Considering the required computational resources and complex methods for theoretical model creation for correct RF-DC conversion efficiency and WPT performance estimation, the current work is based on experimental studies.

1.3. Conclusions on theoretical analysis of WPT technology

The current chapter has summarises and analyses different WPT techniques in near-field and far-field regions. Electromagnetic radiative radiation has been selected as more suitable for autonomous powering of sensor nodes .

The theoretical analyses of studies on RF WPT have shown the following:

- The most popular and promising topology of the rectifier in terms of RF-DC conversion efficiency is the voltage doubler.
- The input power level in the case of autonomous powering of sensor nodes via RF WPT is sufficiently low; therefore, the circuit of the power harvester should be optimised to low input power levels around 0 dBm and lower.
- The lower frequency ranges used for WPT could provide large distance or higher average input power levels for autonomous powering of sensor nodes.
- The impact of the properties of the power-carrying signals on WPT performance is not sufficiently studied yet.
- The research approaches based only on a theoretical analysis could not give sufficiently accurate and calculation resource-saving results.

2. RF-DC circuit prototyping

This section is dedicated to the design of rectifiers voltage doublers and to the Powercast P2110B module accessible in the market. Modelling of the component impact on the power conversion performance, prototyping of the RF-DC converters, and comparing of the theoretical and experimental rectifier's performance have been performed. The parameters of rectifiers are optimised to the ISM 863-870 MHz frequency range, input power level around and below 0 dBm and input impedance of 50 Ω.

The first subsection consists of the rectifier modelling results in the ADS software environment and the evaluation of the parameter value impact on the power conversion performance.

The second subsection is dedicated to evaluating the rectifier's performance with the simulated parameters and assessing the prototyped rectifier's performance.

2.1. Model development and simulation

During the development of the rectifier, it is important to model it and evaluate the performance before making the prototype. The modelling results will allow us to select the components with an approximate value and perform fine-tuning during the testing if required.

One of the selection criteria for the rectifier's components was the price; the other was the availability of the components and materials. Therefore, from the chosen criteria, the most appropriate PCB material is RF-4 (flame retardant 4). It is one of the commonly available PCB materials whose performance is acceptable in the sub-GHz frequency range. When comparing the costs of PCB manufacturing material, for example, manufacturing 100mm by 100mm area PCB, the ten pieces of the FR-4 material will cost around 5$ [73]. However, when manufacturing PCB with the Rogers 4003C or 4350B material, the cost of the ten pieces of PCB will skyrocket up to 370$ or more, depending on the thickness of the substrate [73]. The different PCB material cost comparison is taken from the online instant quote calculator. The price increase when using the ceramic substrate over the FR-4; the cost of manufacturing PCB increases 74 or more times. Additionally, when searching the online electronic component catalogues, such as Digikey, TME, Farnell, Mouser, it is impossible to find the ceramic dielectric copper clad boards for those willing to manufacture PCB using PCB milling devices or perform chemical PCB etching. Still, the FR4 material is available in different sizes and thickness variants at select distributors, such as Digikey, Mouser.

The impact of PCB material on RF-DC conversion efficiency is summarised in Table 2.1. The performance of the FR-4 material in the selected frequency range in the ISM sub-GHz band of 863 to 870 MHz is admissible, and the dielectric losses will not substantially impact the RF-DC rectifier's performance. In this frequency range, the dielectric loss of the FR-4 material is worse than the ceramic substrate Rogers RO4350B PCB; however, for the current application, it is acceptable [74], [75].

The main parameters of the RF diodes are the operating frequency range, the input power level range, and the maximum input voltage level, which in this case is the breakdown voltage level of the diode, series resistance and the diode capacitance. There is a wide range of diodes with similar parameters that are suitable for the RF-DC power conversion in the sub-GHz frequency range, such as Infineon BAT 63-02V [76], Skyworks SMS7630 [77], HSMS-2850/285C [78], with price ranging from 0.5 Euros up to multiple Euros depending on the number of the diodes inside the package and the manufacturer. Theoretical calculations in the source [3] show that to increase the RF-DC power conversion efficiency, it is necessary to select the diode with the low diode junction capacitance C_{j0} and low series resistance R_s. The characteristic parameters of the diodes are summarized in Table 2.1.

Table 2.1

High-frequency RF diode SPICE parameters

Manufacturer	AVAGO		Skyworks	Infineon
Diode model	HSMS-285x[78]	HSMS-286x [79]	SMS7630 [77]	BAT17 [80]
BV, V	3.8	7	2	7
C_{j0}, pF	0.15	0.18	0.14	0.398
Rs, Ω	25	6	20	2.65
EG, eV	0.69	0.69	0.69	0.69
IBV, A	3E-04	1E-05	1E-04	1E-05
I_S, A	3E-06	5E-08	5E-06	3E-09
N	1.06	1.08	1.05	1.009
PB (Vj), V	0.35	0.65	0.34	0.224
PT (XTI)	2	2	2	2
M	0.5	0.5	0.4	0.21

Therefore, taking into account the previous considerations, the selection of the model is as follows: the simulation model contains 2-layer PCB material, and the specified dielectric material dielectric constant of FR4 is set to 4.2. The distance between the copper plates is set to 1.6mm. The size and length of PCB traces are kept short. The length of the traces is set according to the necessary minimum space for the component placement and soldering. The PCB traces in the simulation are substituted with the transmission line segments and the corresponding model, and the diode model is taken from the built-in library. The rectifier component values were simulated in a wide range to see the trend of the impact of the component's on the rectification's efficiency and, therefore, find the optimal values for achieving the highest power conversion efficiency. The component value range for the simulation was selected in a wide range to find values that will allow maximum rectifier performance.

The schematic of the RF-DC converter with the matching network is shown in Fig. 2.1 and consists of the matching network, the clamper, rectifying diode and the low pass filter and load resistance. The copper top layer PCB traces are shown in Fig. 2.2.

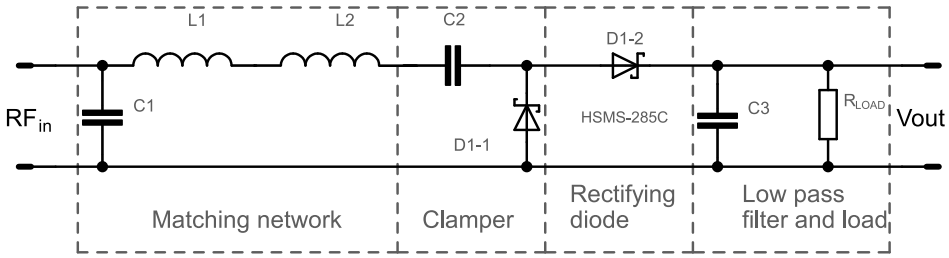

Fig. 2.1. Schematic of the voltage doubler with the matching network.

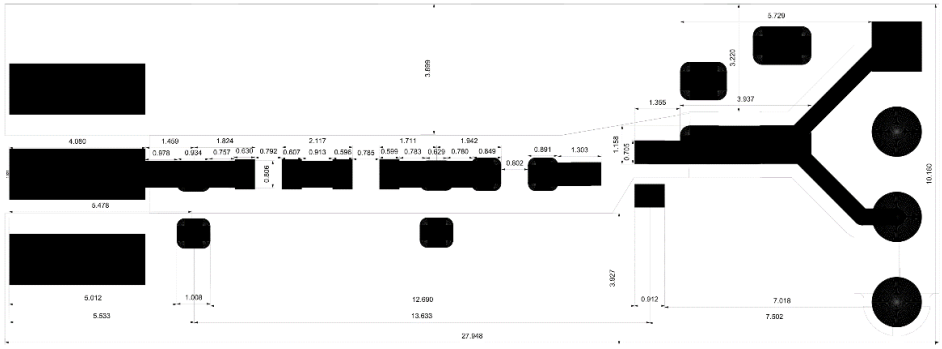

Fig. 2.2. PCB layout of the voltage doubler with the matching network.

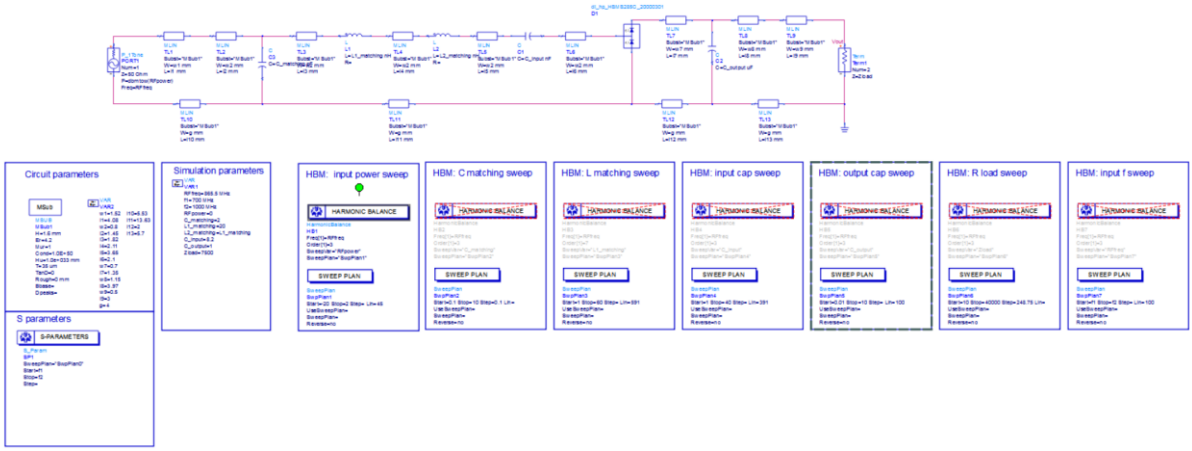

Fig. 2.3. The modelling schematic in the ADS software environment with the RF-DC voltage doubler rectifier with the matching network.

The model in the ADS software environment includes multiple parametric modelling settings. The outline preview of the PCB model and simultaneously enabled HBM settings is active, as shown in Fig. 2.3. The circuit PCB traces from Fig. 2.2. in the simulation model are substituted with transmission line elements, where the length and width of each wire segment were measured on the prepared layout.

However, the Powercast module P2110B simulation was not performed due to the un-accessible schematic; therefore, the simulation model cannot be created. According to the datasheet [81], this module provides a good match to the 50 Ω impedance antennas. The device starts to operate from -12 dBm input power level up to 10 dBm input power level. The module also has a controllable built-in DC-DC converter. The module frequency characteristics vary

and depend on the input signal power level: at a low input power level, -6 dBm reaches the maximum power conversion efficiency of 55 % at 868 MHz and 12% efficiency at the -10 dBm input power level. The module includes programmable inputs that can be used to switch to measuring the input power level [81].

2.2. Modelling

The modelling of the RF-DC converter was performed in the ADS software using the RF simulation package, employing the harmonic balance method (HBM) solver. This solver was selected due to its fast calculation time to reach the steady-state of the circuit's parameters instead of the time-domain-based solvers. The HBM solver works in both - the time and frequency domain - to acquire the steady state. The RF-DC converter topology for the rectifier was selected to be the voltage multiplier design. The schematic for the rectifier is given in Fig. 2.1. Additional components were added for the matching network to allow more tuning capabilities after manufacturing the prototype.

After a study of the corresponding scientific publications [31], [82], [83] and books [2], [84], it has been concluded that the RF-DC rectifier optimal parameter selection was vague in so many literature reviews due to many factors to take under-consideration: different PCB dielectric materials, the thickness of the dielectric material, diode parameters and parasitic parameters, operating frequency range, dielectric loss tangent, or relied on numerical methods to derive optimal parameters in the iterative process [3]. An approximate component value range was obtained from iterative simulation results. Therefore, multiple simulations were performed with varying parameter values until the trend of the component value impact was obtained.

Table 2.2

RF-DC Voltage Doubler with the Matching Network Simulation Parameters

Input power level, dBm	–20 to +2
Frequency range, MHz	863–870
C_2, pF	1–40
C_3, µF	0.01–10
L (L_1 + L_2) matching at specified C (C_1) matching values (0.1 to 10) pF; nH	10, 20, 30, 40, 50, 60
C (C_1) matching at specified L (L_1 + L_2) matching values (1 to 120) nH; pF	0.5, 1, 2, 3, 4, 5
R Load resistor, kΩ	0.01–40

Therefore, in the simulation, the rectifier's component values were swept in a wide range to find the combination that would provide optimal performance. The range of the values is shown in Table 2.2. Some parameter values must be selected beforehand, such as the load resistor value. The rectifier will need to supply power to the sensor or device with a defined input impedance. Therefore, the load resistor value in the circuit was set to 7.5 kΩ, as similar input impedance is usually set for the low input power DC-DC converters. The input capacitor value was set to 8.2pF and the output capacitor of 1µF, later refined in the simulations. The matching

capacitor and inductor sweep values were selected from a broad range. Multiple iterations of the simulation model should show the combination of matching network component values that will provide the highest power conversion efficiency.

After multiple iterations of component value sweep, the following component values were selected as in simulation: the matching inductor value sweep range was from 10 nH to 60nH with the step of 10 nH value. The matching capacitor value sweep was performed from 0.1pF to 10 pF.

The rectified voltage and power conversion efficiency simulation with parametric matching capacitance values sweep at the specified 6 inductor matching values are shown in Fig. 2.4. The matching network inductance simulation indicates that inductor values, for example, 10 or 20, or 30 nH are not the optimal values. The peak rectified voltage cannot be achieved by varying the matching capacitance value. Additionally, with these inductor values, the increase of the matching capacitance will decrease the rectified voltage.

In these sweeping component value simulation series, the highest rectified voltage, shown in Fig. 2.4, is achieved with the matching network inductor value of 40 nH and the matching capacitor value of approximately 1.8 pF value. There is only one voltage peak in the graph. For the inductor values that are much higher than 40 nH, the rectified voltage peaks decrease significantly and produce multiple local maximum peaks. Therefore, the optimal value for the matching inductor is 40nH. The efficiency of the rectifier is calculated by dividing the power across the resistor by the signal input power level at the rectifier's input—the highest efficiency with the most optimal results in simulation yield 82.5 %.

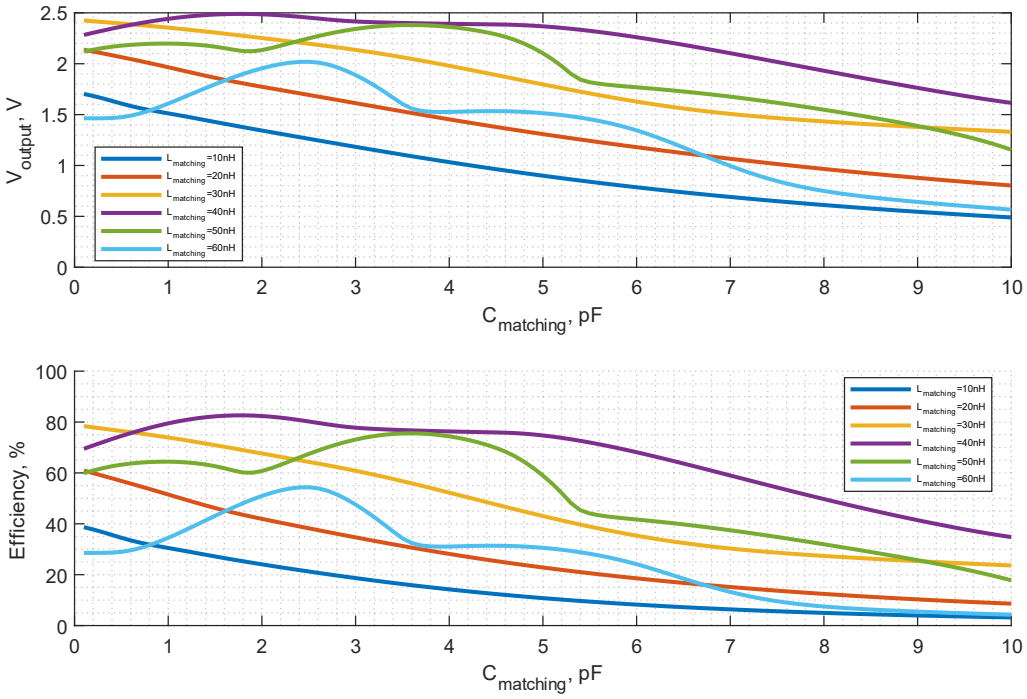

Fig. 2.4. Matched RF-DC voltage doubler output voltage and conversion efficiency depending on the matching capacitor value, C_2 = 8.2 pF; C_3 = 1 µF; R_{load} = 7.5 kΩ; frequency is 865.5 MHz; input power is 0 dBm.

The following graphs include the results from the sweep simulation, where the matching network capacitance is constant, and the matching network inductance is swept in the defined range. In this simulation, the matching network inductance is swept from 1nH to 120 nH at constant matching network capacitance values of 0.5, 1, 2, 3, 4, 5 pF. The results of the simulation are shown in Fig. 2.5.

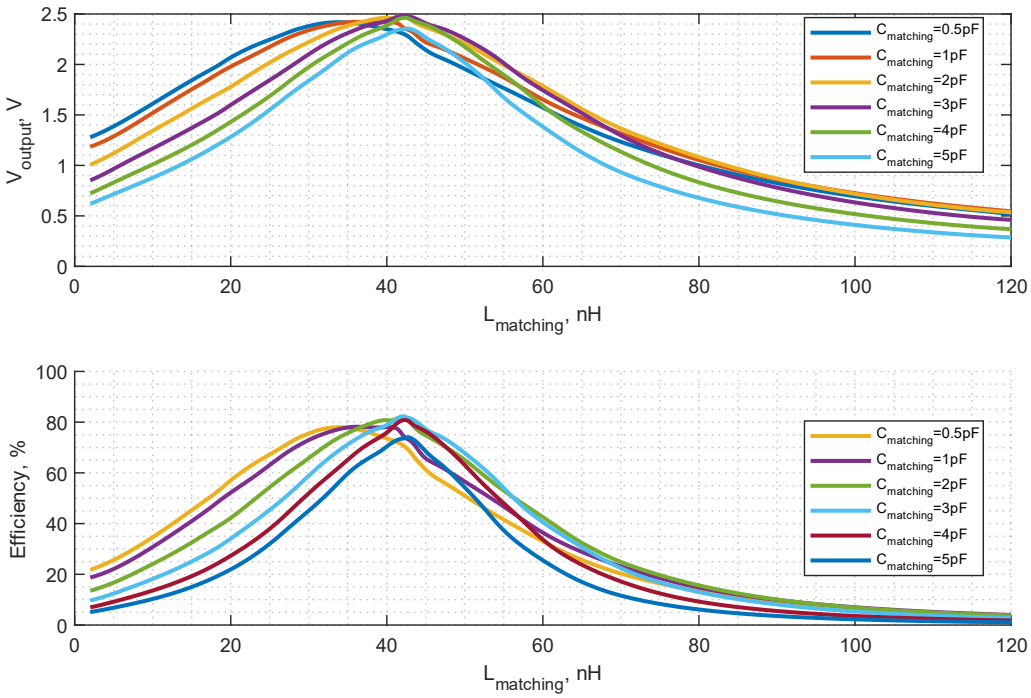

Fig. 2.5. Matched RF-DC voltage doubler output voltage and conversion efficiency depending on the matching inductor value, $C_2 = 8.2$ pF; $C_3 = 1$ µF; $R_{load} = 7.5$ kΩ; frequency is 865.5 MHz; input power is 0 dBm.

The rectified voltage dependence from the exact value of the matching network inductance is more dominant, and the matching network capacitance has a much less impact on the rectified voltage level. The near-maximum rectified voltage can be achieved with multiple combinations of matching network capacitance and inductance values with all tested matching network capacitance values. However, the highest rectified voltage is obtained using matching networks capacitance of 3 pF and inductance of 41 nH when the voltage level reaches 2.5 V and the efficiency reaches 83%; therefore, these values are used in the following simulations.

After obtaining the matching network's optimal parameters, the impact of the remaining rectifier's circuit component values was analysed. Therefore, the impact of the input capacitor C2 was evaluated, where the value was varied from 1pF to 40 pF, as shown in Fig. 2.6. The simulation shows that the input capacitor value has a minor impact on the rectified DC voltage level in the modelled capacitance range. The same is also true for the power conversion efficiency.

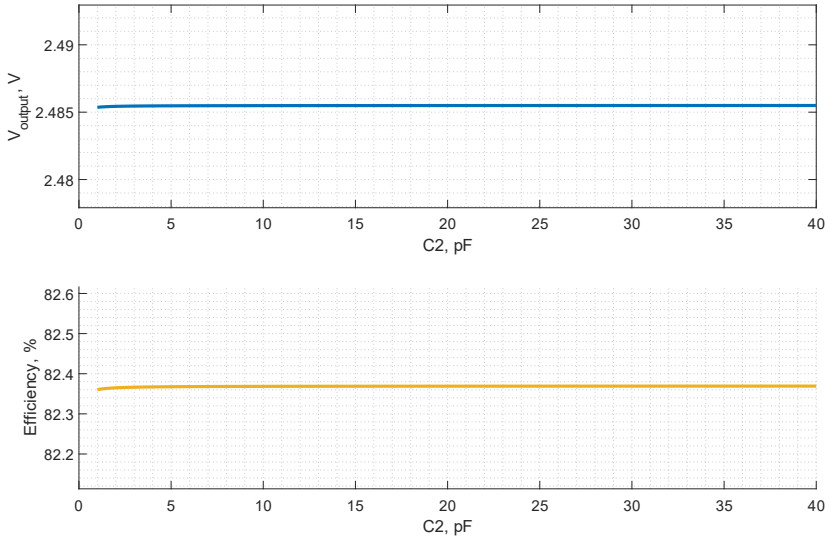

Fig. 2.6. Matched RF-DC voltage doubler output voltage and conversion efficiency depending on the input capacitor value, C_1 = 2pF, L_1=L_2=20nH, C_3 = 1µF, R_{load} = 7.5 kΩ, frequency is 865.5 MHz, input power is 0 dBm.

The impact of the capacitor C3 value on the rectified voltage level and the power conversion efficiency was also evaluated. The capacitance varied from 100 pF to 10 µF, as shown in Fig. 2.7. The simulation results show that the capacitance C5 in the selected value range has little impact on the power conversion efficiency. However, the larger capacitance will provide rectified voltage with lower ripples for the signals with a high peak to average power ratio.

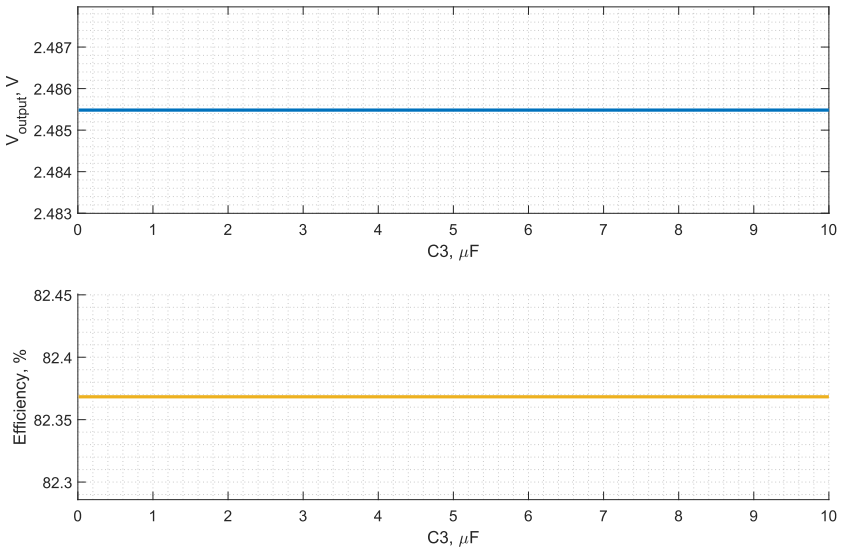

Fig. 2.7. Matched RF-DC voltage doubler output voltage and conversion efficiency depending on the output capacitor value, C_1 = 2pF, L_1=L_2=20nH, C_2 = 8.2pF, R_{load} = 7.5 kΩ, frequency is 865.5 MHz, input power is 0 dBm.

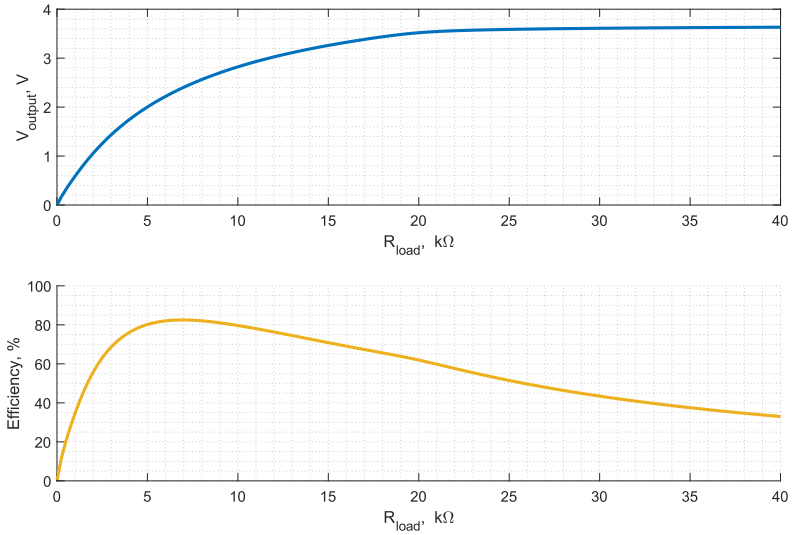

Fig. 2.8. Matched RF-DC voltage doubler output voltage and conversion efficiency depending on the load resistance value, C_2 = 2pF, L_1=L_2=20nH, C_2 = 8.2pF, frequency is 865.5MHz, input power is 0 dBm.

The load resistor is one of the parameters that impact the rectified voltage level and the input impedance level. The rectified voltage level and the power conversion efficiency depending on the load resistance are shown in Fig.2.8. As the load resistance increases, the rectified output voltage also increases, starting from 0 V with very low impedance to 3.6 V at 40 kΩ load resistance. However, the most efficient power conversion is achieved with the 8.5 kΩ load resistance.

The simulation where the impact of the signal frequency on the rectifier circuit performance was also evaluated in an extensive frequency range. Although the rectifier will be used in the sub-GHz frequency range, this is performed to see if the rectifier's best performance is achieved at precisely the needed frequency range. The rectified voltage level and efficiency dependence is shown in Fig. 2.9. As can be seen from the graph, at the desired frequency range from 863-870 MHz, the rectifier performs the best and achieves the highest rectified voltage level.

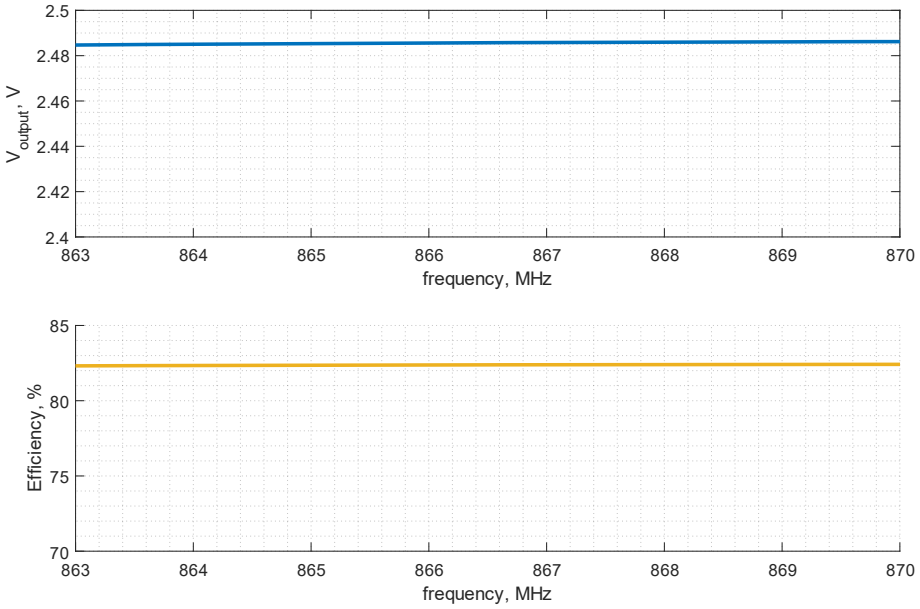

Fig. 2.9. Matched RF-DC voltage doubler output voltage and conversion efficiency depending on the signals input frequency, R_{load} = 7.5 kΩ, C_4 = 1µF, C_2= 8.2pF, C_1 = 2pF, L_1=L_2=20nH, C_1 = 1pF, input power is 0 dBm.

2.3. Measurements of rectifier's input impedance

The prototype of the RF-DC converter circuit was fabricated using a milling machine LPKF Proto Mat S103. The circuit components were mounted on the top layer of PCB (see Fig.2.9.) made of FR-4 with a dielectric constant of 4.3 (manufacturer-specified). The thickness of the substrate was 1.6 mm.

As the RF-DC rectifiers will use an antenna with the 50 Ω impedance and be used in measurements with a 50 Ω input impedance, the RF-DC converters must also have a 50 Ω input impedance to achieve the highest power conversion efficiency.

After initial modelling and prototyping of the RF-DC converter with optimal component values for the rectifier, the prototype performance did not match the results in the simulation.

Therefore, additional matching network tuning was required to achieve better power conversion efficiency.

The evaluation of the prototype input impedance to the required 50 Ω was performed with the vector network analyser (VNA) device, and the evaluating parameter was the scattering parameter S11, which is the input impedance parameter and shows how much of the signal power will be reflected back to the antenna or measuring device.

During the tuning, the most optimal matching parameters for achieving the highest rectified voltage for the prototyped rectifier with the matching network were 36 nH inductance and 3 pF capacitance, which differed from the simulated best matching network parameters. The selected circuit parameters are shown in Fig. 2.10. The final component values are as follows: C_1 = 3 pF; C_2 = 8.2 pF; C_3 = 1 µF; R_1 = 7.5 kΩ; L_1 = L_2 = 18 nF.

The circuit was driven using a coaxial cable with the characteristic impedance of 50 Ω. The 50 Ω impedance value was chosen to match the readily accessible antenna's impedance and the measurement equipment's input impedance. For the prototype, Schottky diode HSMS-285C was selected for D1 and D2.

Another RF-DC rectifier was prototyped without the matching network to investigate the matching network's impact on power conversion efficiency. The schematic is shown in Fig. 2.11. The commercially available off the shelf RF-DC converter module Powercast P2110B was also used for comparison. The prototyped RF-DC converters are shown in Fig. 2.12.

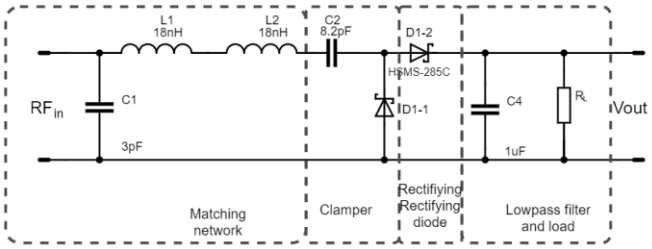

Fig. 2.10. Matched RF-DC voltage doubler schematic with matching network with the component nominals.

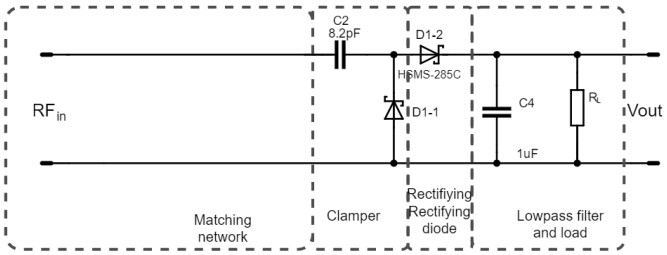

Fig. 2.11. Matched RF-DC voltage doubler schematic without matching network with the component nominals.

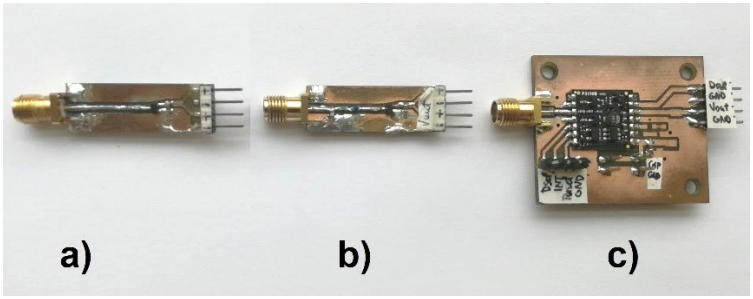

Fig. 2.12. RF-DC converters: a) voltage doubler converter without the matching network, a) voltage doubler converter with the matching network, Powercast P2110B module

Generally, it is considered proper matching if the |S11| scattering parameter is below –10 dB or lower. The Smith chart S11 input impedance and the |S11| parameter module are given in Fig. 2.13 for the voltage doubler rectifier with matching network, in Fig. 2.14 for the voltage doubler rectifier without matching network, and in Fig. 2.15 for the Powercast P2110B module. The results of the input impedance of the voltage doubler rectifier with matching network at different input power levels show a proper matching in the frequency range from 863–870

MHz: at the input power level of -2 dBm the |S11| is lower than the –32 dB, at –10 dBm, the |S11| is below –19 dB, –6 dBm, the |S11| is below –25 dB, at 0 dBm, the |S11| is below –27 dB.

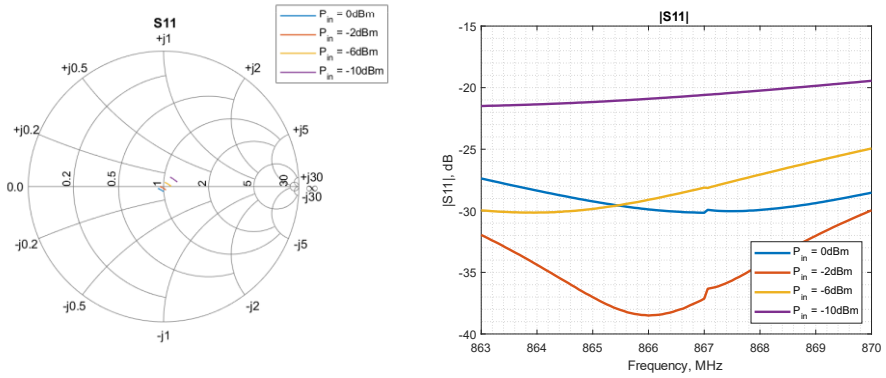

Fig. 2.13. The voltage doubler rectifiers with the matching network S11 Smith chart and |S11| frequency response at different power levels.

The |S11| measurement result for the voltage doubler rectifier without the matching network shows poor matching, the |S11| does not exceed –0.78 dB at all of the tested signal input power levels. This device will reflect a lot of the received signal from the input port. The input impedance of this converter may damage the signal generator output at high input power levels.

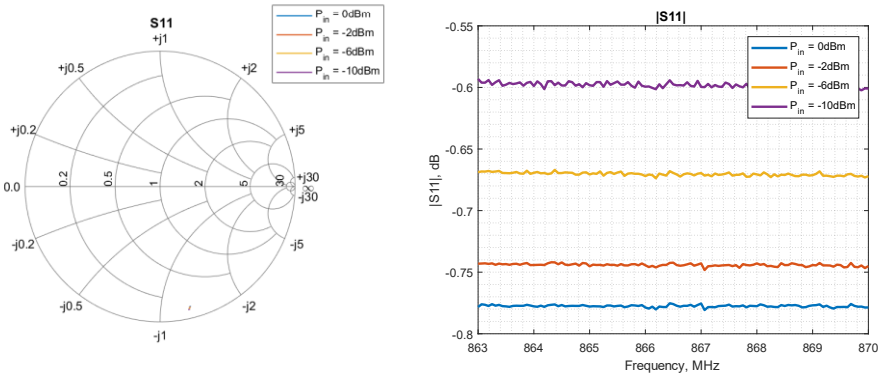

Fig. 2.14. The voltage doubler rectifiers without the matching network S11 Smith and |S11| frequency response at different power levels.

The same input impedance measurements were also performed with the Powercast P2110B module, where the measured |S11| parameter at all of the tested input power levels were below –15 dB. This rectifier with the signal input power level at -10 dBm will provide |S11| below –17.5 dB, at –6 dBm will provide |S11| below –15.5 dB, at –2 dBm will provide |S11| below –18 dB, at 0 dBm will provide |S11| below –18 dB, which overall is good matching.

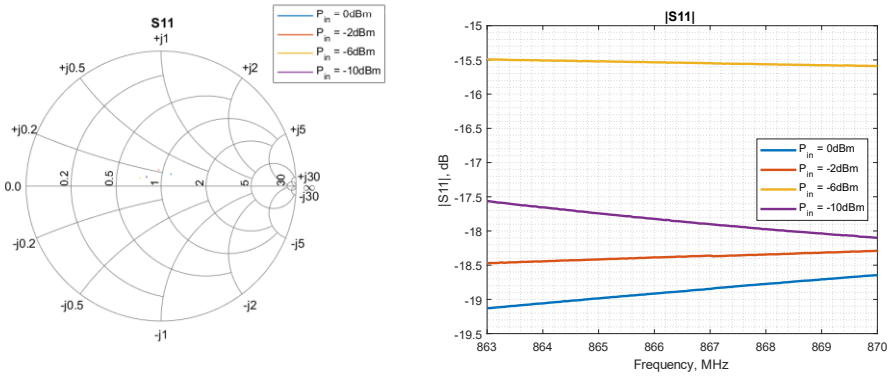

Fig. 2.15. The Powercast P2110B modules S11 Smith and |S11| frequency response at different power levels.

2.4. Conclusions on RF-DC circuit prototyping

In this chapter, simulations and prototyping for ISM 863–870 MHz frequency range, input power level below 0 dBm, and input impedance of 50 Ω have been performed. Several prototypes have been fabricated voltage doubler with and without the matching network and Powercast P2110B module. The performance of the rectifiers has also been compared.

The simulation results for the voltage doubler rectifier with the matching network show similar performance to the manufactured prototype. The impedance matching network component values used in the prototype differ from the simulated values; however, no more than 10%. The RF-DC rectifier power conversion efficiency depends on the correctly selected matching network component values and the load resistance values at the specified input power level and the signal frequency. The values of the voltage doubler with the matching network were selected for the operation in the sub-GHz frequency range at a relatively low input power level. The load resistance value is equivalent to the DC-DC converter's input impedance. The input impedance is matched to be compatible with the 50 Ω antennas.

The Smith charts and the corresponding S11 module frequency response graphs show that the voltage doubler with the matching network and the Powercast module has an adequate input impedance matched to the 50 Ω measurement equipment. Respectively, the signal frequency in the ISM 863-870 MHz band will have little impact on RF-DC conversion performance.

3. Experimental study on RF-DC conversion efficiency

Historically, the signals used in the RF-DC power conversion and WPT were the sine waveform. However, as technology and communications systems advance, the waveforms used in these areas also advance. Nowadays, different RF signal power densities in surrounding areas are increasing due to telecommunication towers, transceivers, and low-power wireless sensor networks. The increase in the RF signal power density is more prevalent in densely populated areas and can be used for energy harvesting.

Multiple published scientific papers have explored different signal parameter influences on the RF-DC power conversion efficiency, such as signal waveforms [31], signal average input power level, signal bandwidth [71], [29], signal peak to average power ratio [85], [86]. However, these investigations are usually limited and often focus on just a few listed parameters. The studies' results are not comparable as the testing conditions, the selected frequency range, rectifier designs, and input power levels differ too much. Therefore, this study is devoted to the investigation of the signal parameters that impact the RF-DC power conversion and are evaluated with multiple RF-DC converters. The parameters that will be investigated are as follows:

- signal average input power level;
- signal frequency;
- signal bandwidth;
- the number of signal subcarriers.

The investigation includes constant envelope waveforms such as sine wave, FM modulated signals, CHIRP, and variable envelope signal waveforms such as multitone signals with different PAPR levels, shown in Table 3.1.

Table 3.1

Characteristics of the Employed Signal

Signal envelope	Signal waveform
Constant envelope	sine
	FM tonal modulated signals
	CHIRP (linearly increasing frequency in the selected frequency range)
Variable envelope	multitone signals with a high PAPR level (HPAPR)
	multitone signals with low PAPR level (LPAPR)
	multitone signals sub-carriers generated with random seed (RPAPR)

The multitone signals are generated by summing up uniformly distributed subcarriers with selected amplitudes and phases. The baseband multitone signal with a high PAPR level, created by summing all subcarriers with the same amplitudes and phases, will be denoted as the HPAPR multitone. The baseband multitone signal with a low PAPR level is created by summing all subcarriers with the same amplitudes and different phases. The Zadoff-Chu sequence is used to generate the phases through IFFT [86], further denoted as the LPAPR multitone. The baseband multitone signal with random subcarrier amplitudes and phases, further denoted as the RPAPR, is created using the same random seed generator to generate subcarrier amplitudes and phases [5].

The signal waveforms for the multitone signal with subcarriers range from 5 to 256 with an average input power level of -10 dBm are shown in Fig. 3.1.

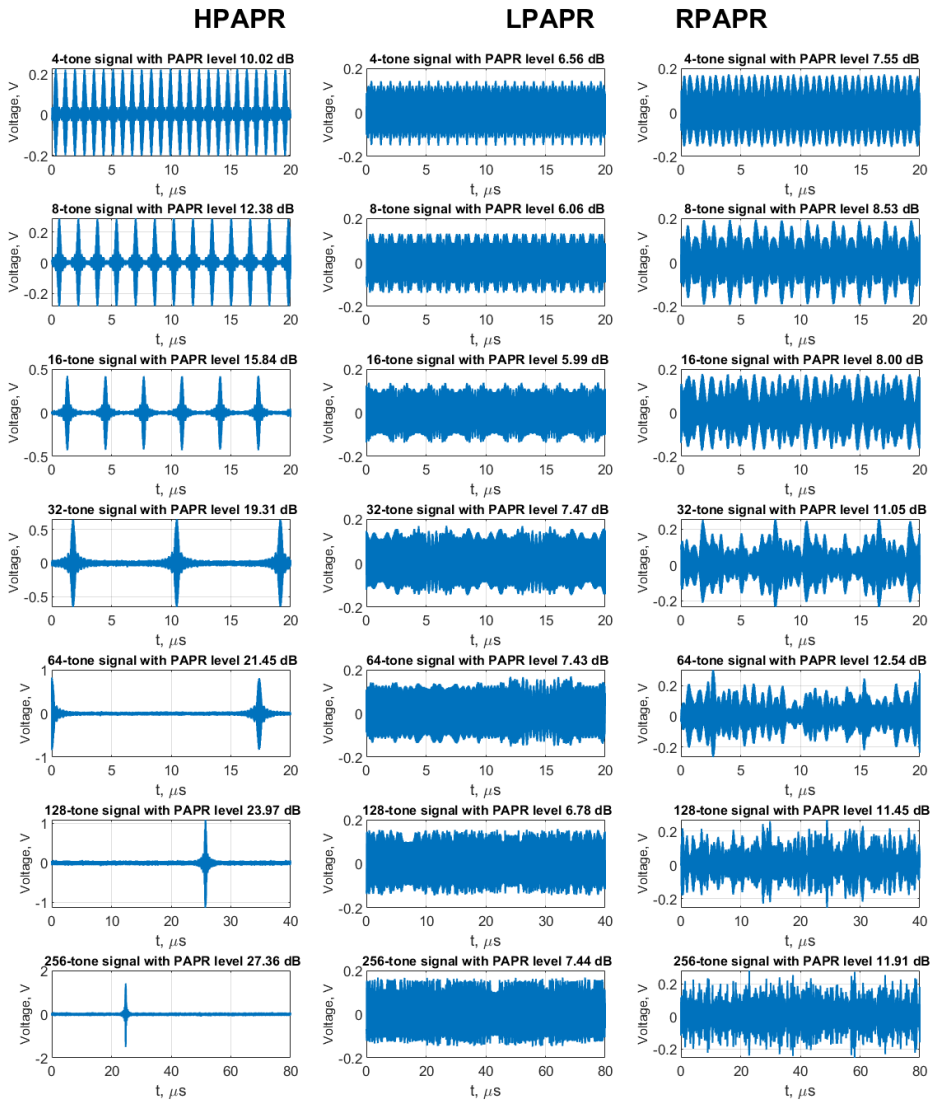

Fig. 3.1. Generated multitone signal waveforms with subcarriers ranging from 4 to 256 at the input power level of -10 dBm power level.

The CHIRP waveform generation was performed by MATLAB/SIMULINK software. The signal parameters were as follows: central frequency = 868.1MHz, spreading factor SF = 9, signal bandwidth BW =150KHz, Tsymb = 4 ms [15]. The signal waveform waterfall is displayed in Fig. 3.2.

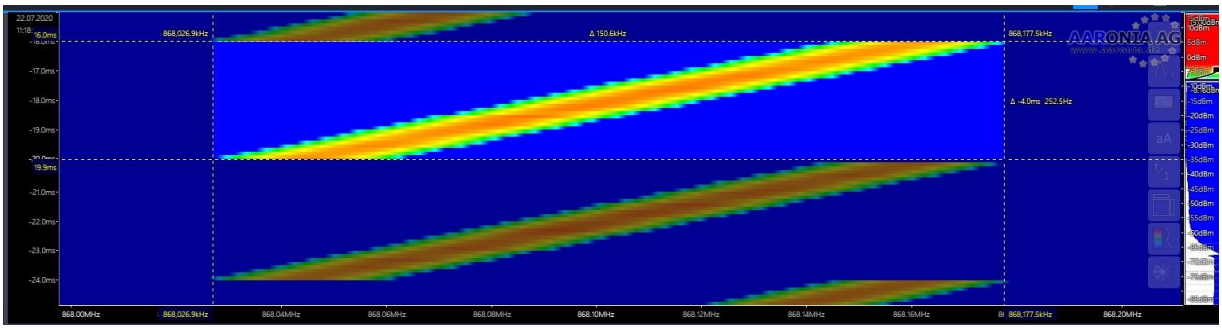

Fig. 3.2.Waterfall of the CHIRP signal waveform.

The frequency of the carrier signal is 865.5 MHz. The deviation frequency is 4.8 MHz, and modulating frequencies were 100 kHz and 1 MHz, corresponding to 4.8 (low) and 48 (high) FM modulation indexes. The spectra of the used FM signals are demonstrated in Figure 3.3. This study was performed with the voltage doubler-based and Powercast RF-DC converters.

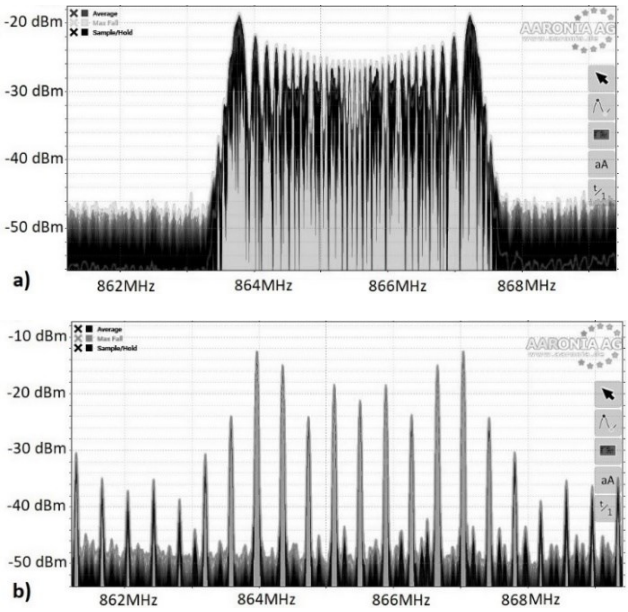

Fig. 3.3. Spectra of FM waveforms: a) with 100kHz modulating signal (high modulation index), b) with 1MHz modulating signal (low modulation index).

Table 3.2.

RF signal parameters.

Signal waveform	Sine	HPAPR	LPAPR	RPAPR	FM	CHIRP
Average power level	-25 dBm to 0 dBm					
Signal bandwidth	-	50KHz, 500KHz, 5MHz			5MHz	*150KHz*
Subcarriers	1	4 - 256			Mod ind 4.8,48	-
PAPR level, dB	3	10-33	6-7.5	7.6-12	3	3

The signal parameters used in the RF-DC power conversion measurements are summarized in Table 3.2. The employed signal average input power level ranges from -25 dBm to around 0

dBm, with the constant envelope signals (sine, CHIRP, FM modulated signals) and multitone signals (HPAPR, LPAPR, and RPAPR). The multitone signal has been employed with three different bandwidths: 50 kHz, 500 kHz, and 5 MHz. The PAPR level for all these signals is as follows: the constant envelope PAPR level is 3 dB; for the multitone signals, it differs, starting from 6 dB to 33 dB, depending on the subcarrier value and the multitone signal generation scheme.

Another factor influencing the RF-DC power conversion efficiency is the RF-DC topology.

Two RF-DC rectifier procurement approaches were selected for this study to investigate the signal parameter impact on the RF-DC power conversion. One was to create the RF-DC power converter using the discrete components (RF diodes, RF inductors, RF capacitors), and another - to employ the already manufactured rectifiers that are popular and are freely available for purchase - such as the Powercast P2110B module [88], that incorporates the RF-DC and DC-DC converter (disabled during testing). The RF-DC converter topology selection for the rectifier from the discreet elements is generally a trade-off between the rectified output voltage and the power conversion efficiency. Naturally, the increase in the number of diodes leads to higher voltage drops across the diodes and, subsequently, lower efficiency. As more diodes are added, the more efficiency drops due to the voltage drop across the diodes. Therefore, for this reason, the RF-DC converter multiplier design will be employed, as it provides a high enough output voltage level and power conversion efficiency.

The investigation of the different signal parameter impact on the power conversion efficiency is divided into 3 specific research directions, which are as follows:

1. Signal waveform impact on the conversion efficiency,
2. Multitone signal subcarrier impact on the conversion efficiency,
3. The matching network impact on conversion efficiency.

The first research investigates the signal waveform's impact on conversion efficiency. In this study, the signals with the constant and variable envelope (multitone signals with different signal bandwidths) were employed during the RF-DC power conversion measurements. The RF-DC converter used in the evaluation was the RF-DC voltage doubler with the matching network.

In the second research direction, the multitone signal subcarriers' impact on the power conversion efficiency was assessed. In this assessment, multitone signals with different PAPR levels were used. The number of HPAPR, LPAPR, and RPAPR multitone signal subcarriers varied from 4 to 256. The measurements were performed with the prototyped RF-DC voltage doubler with the matching network and the commercially available Powercast P2110B module.

One of the components influencing the RF signal power conversion is the matching network. Therefore, the third research direction was dedicated to the study of the impact of the matching network on the power conversion efficiency for the voltage doublers topology. The RF-DC power conversion measurements employed two RF-DC power converters: voltage doubler with the matching network that has a good match for the specified sub-GHz frequency range with the 50 Ω input impedance, and RF-DC converter voltage doublers converter without the matching network. The focus of the study was on the impact of the matching network on

power conversion efficiency; therefore, signals with different waveforms and subcarrier numbers were used in the RF-DC measurements.

The component values of the RF-DC rectifier with the matching network and the voltage doubler without the matching network are given in Table 3.3. and general schematic of the prototyped rectifier is shown in Fig. 3.4. The picture of the RF-DC converter prototyped boards: voltage doubler with matching network, a) voltage doubler without matching network b), and Powercast module P2110B c) is shown in Fig. 3.5.

Table 3.3

Parameters of Experimental RF-DC Rectifiers

Rectifiers	***Components***					
	C*1, *pF	***L*1, nH**	***L*2, nH**	***D1, D2***	***C*3, µF**	***R*1, kΩ**
RF-DC voltage doubler rectifier without matching network	–	–	–	HSMS-285C	1 ± 10 %	7.5 ± 0.1 %
RF-DC voltage doubler rectifier with matching network	3 ± 0.1	18 ± 5 %	18 ± 5 %	HSMS-285C	1 ± 10 %	7.5 ± 0.1 %

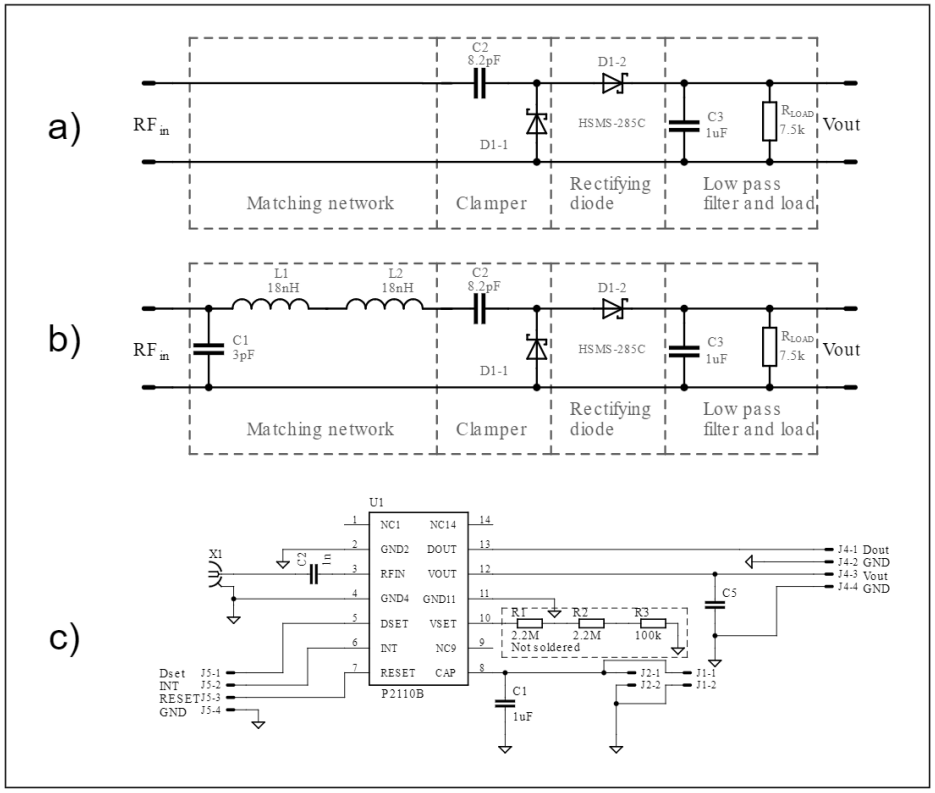

Fig. 3.4. The RF-DC rectifiers schematics: a) RF-DC voltage doubler without matching network; b) RF-DC voltage doubler with matching network; c) Powercast P2110B module.

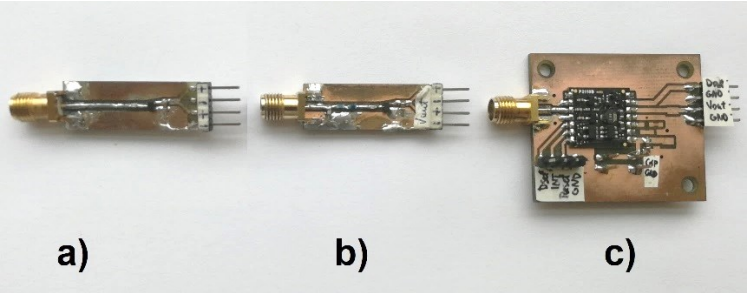

Fig. 3.5. The RF rectifier prototypes: a) RF-DC voltage doubler without matching network, b) RF-DC voltage doubler with matching network, c) Powercast P2110B converter module.

The generation of the signals is performed using universal software radio peripheral (USRP) software-defined radio device (SDR) B210 from the company Ettus Research company. The device has a diverse capability and can generate or receive signals in the frequency range from 70 MHz up to 6 GHz, with an instantaneous real-time bandwidth of 56 MHz. This study uses this device to generate multitone signal waveforms, FM tonal modulated signals, CHIRP, and sine.

The measurement setup of the RF-DC measurements is shown in Fig. 3.6. It consists of two parts: part A) – where the average input power level for the signal is calculated, and B), where the RF-DC measurements are performed, and the DC voltage is measured across the rectifier's load resistance. The devices used in the measurements consist of a host PC with MATLAB/SIMULINK software, the USRP SDR B210, digital oscilloscope Tektronix DPO-72004C and PSMU unit Keysight B2901A. A more precise signal generator, Rohde & Schwarz R&S SMR30 and later SMC100A, is used as a reference signal. The latter is used for automated measurements due to the simple USB interface with the GPIB commands. The RF signal average output power is calculated using a digital oscilloscope in 50Ω input mode (Tektronix MSO5204B or Tektronix DPO72004C) and is calculated using built-in functions. The signal generator's signal is fed to the RF-DC conversion board using an SMA cable. The RF-DC rectifier output is connected to a load resistor. During the experiments, the voltage across the load resistor is measured with either multimeter INSTEK GDM-8246 or power supply management unit Keysight B2901A. The output power of the RF-DC rectifier is calculated by squaring the rectified DC voltage across the load resistance, formula shown in equation (3.1). The efficiency is calculated by dividing the output power by an input power level and then converting it to a percentage, formula shown in equation (3.2). The measurement with the Keysight PSMU is automated using MATLAB scripts developed by the author (See Annex 1, Annex 2, Annex 3) over the USB cable with GPIB commands. The created MATLAB scripts use the hardware to perform the RF-DC measurements, such as the average input signal power level from the oscilloscope and the output voltage from the RF-DC rectifier across the load resistance.

$$P_{OUTPUT} = \frac{U_{LOAD}^2}{R_{LOAD}} \tag{3.1}$$

where P_{OUTPUT} – output power of RF-DC rectifier (power across the load resistor), U_{LOAD} – voltage across the resitor, R_{LOAD}–load resitor value.

$$\eta = \frac{P_{OUTPUT}}{P_{INPUT}} \cdot 100 \quad (3.2)$$

where η – power conversion efficiency in percentage, P_{OUTPUT} – output power of RF-DC rectifier, P_{INPUT} – input power of signal fed to the RF-DC rectifier.

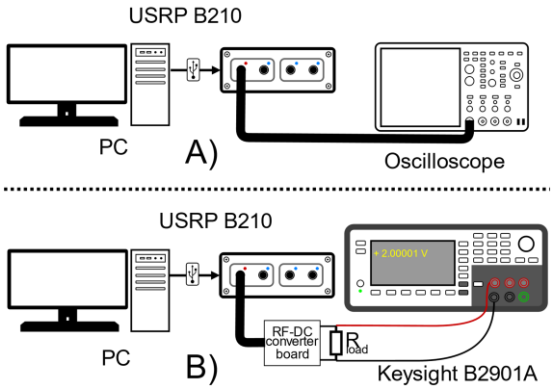

Fig. 3.6. RF-DC Measurement setup.

The RF-DC measurement workflow is as follows: the signal is generated by SDR B210, which is controlled by the MATLAB/SIMULINK software. The Simulink model creates the required baseband signal, then transferred to the SDR hardware USRP B210. The generated baseband signal is then transferred to the carrier frequency. After that, the generated signal is forwarded to a specified output channel.

The following signal waveforms were created with this software setup: multitone signals with high PAPR level (HPAPR), multitone signals with low PAPR level (LPAPR), multitone signals sub-carriers generated with random seed (RPAPR), FM tonally modulated signal, CHIRP signal, sine.

3.1. Signal waveform impact on the power conversion efficiency

3.1.1. Objective

The objective of this chapter is to study the signal waveform impact on the RF-DC power conversion efficiency. In this study, the research focuses on the signal bandwidth and subcarriers' impact on the RF-DC conversion efficiency.

3.1.2. Tasks

To evaluate the impact of the signal waveform on the RF-DC conversion efficiency, measurement series with the specified types of signals were performed. The employed signal waveforms consist of constant and varying envelope signals and are already introduced at the beginning of Chapter 3. The waveforms of the HPAPR, LPAPR, and RPAPR multitone signals with subcarriers in the range from 4 to 256 are employed. More detailed information regarding

the used signal parameters is shown in Table 3.4. The multitone signals subcarriers were varied in range from 4 to 256, the input power from -17 dBm to 0 dBm power level.

Table 3.4

RF Signal Parameters

Signal waveform	Sine	HPAPR	LPAPR	RPAPR	FM	CHIRP
Average power level	–25 dBm to 2 dBm					
Signal bandwidth	-	50 kHz, 500 kHz, 5 MHz			5 MHz	150 kHz
Subcarriers	1	8			Modulation index 4.8, 48	-
PAPR level, dB	3	10–33	6–7.5	7.6–12	3	3

3.1.3. Measurement setup and experiments

The measurements are divided into two parts: 1) the signal average input power level is measured for all the signals employed in this experiment, and 2) the signal is fed to the rectifier and the rectified voltage level is measured for the corresponding input signal power level.

The measurements were performed with the RF-DC voltage doubler with the matching network rectifier. As the RF-DC power conversion efficiency is dependent on the load resistor value, the measurements were performed with the 3 different load resistors. As already concluded in the previous section, the rectifier's most optimal resistance value for the sine wave ranges from 7.5 kΩ to 10 kΩ. Therefore, measurements were performed with other resistance values, for example, 1kΩ that will emulate a load that requires a much higher current and 100kΩ value resistor, which will mimic a load that requires minimal current. The RF-DC rectifier performance was measured with different signal waveforms and compared to the sine waveform.

In the next experiment series, the RF-DC conversion measurements with 3 different signal waveforms with 8 subcarriers were performed to evaluate the power conversion efficiencies: HPAPR multitone, LPAPR multitone, RPAPR multitone at input power levels from –25dBm to +2 dBm power level, and with 3 signal bandwidth settings: 50 KHz, 500 KHz, 5 MHz, the parameters given in Table 3.4.

Table 3.5

RF-DC Rectifier Frequency Characterization Parameters

Input power, dBm	–10, –6, –2, 0, 2
frequency, MHz	863–870
Load resistor, kΩ	1, 10, 100

The characterization of the RF-DC converter was also performed in the frequency range from 863MHz to 870MHz at different input power levels with a constant load resistor. The investigation of the rectifier with the sine waveform at the average input power levels at –10dBm, at –6dBm, at –2 dBm, and 2dBm in the frequency range from the 863 to 870 MHz was performed to evaluate not only the frequency impact on the power conversion efficiency but also the input power level impact. Parameters are given in Table 3.5.

3.1.4. Experimental results

This section shows the RF-DC voltage doubler with the matching network rectifiers' performance with different signal waveforms, signal bandwidths, input power levels, and 3 different load resistor values.

The power conversion efficiency measurements were performed with 3 different load resistor values employing an RF-DC voltage doubler with the matching network; the results are shown in Fig. 3.7. The highest power conversion efficiency of 62 % is achieved with the load resistance of 10 kΩ. In contrast, other resistance values provide much lower efficiency and will be used to compare the different signal waveforms. The peak efficiency for the matched RF-DC rectifier with the 10 kΩ resistance load is achieved at the input power level of 0 dBm. At the -20 dBm power level, the power conversion efficiency with the 1 kΩ load is 10 %, with the load resistance of 10 kΩ, the conversion efficiency is 28 %, with the load of 100 kΩ, the conversion efficiency is 12%. In the tested range of the average input power levels, the conversion efficiency with the 1 kΩ load does not exceed 35 %, with the 100 kΩ resistance load, the efficiency does not exceed 16 %, and with the 10 kΩ load resistance, the efficiency peaks around 63 %.

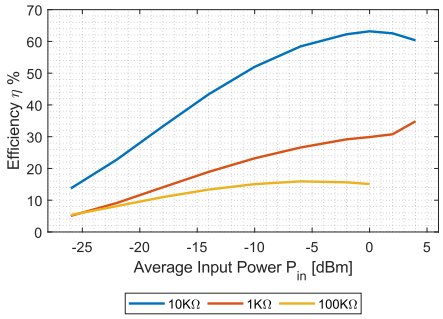

Fig. 3.7. Matched RF-DC voltage doubler with matching network conversion efficiency depending on different load resistances at different input power levels

The rectifier's performance dependence measurement of the signal frequency was performed with the load resistance of the 10 kΩ. The measurement consisted of the sine wave swept in the range from 863 to 870 MHz at 6 different power levels: –10 dBm, –6dBm, –2 dBm, 0dBm, 2dBm. The results are shown in Fig. 3.8. At the average input power level of –10 dBm, the power conversion efficiency is 50 %, at the –6 dBm input power level, the power conversion efficiency is around 57 %, at the input power level of –2 dBm the power conversion

efficiency is 61 %, at 0dBm input power level, the efficiency is about 63 %, and at 2 dBm input power level, the power conversion efficiency is also around 63 % in the specified frequency range with slight deviation across the frequency range.

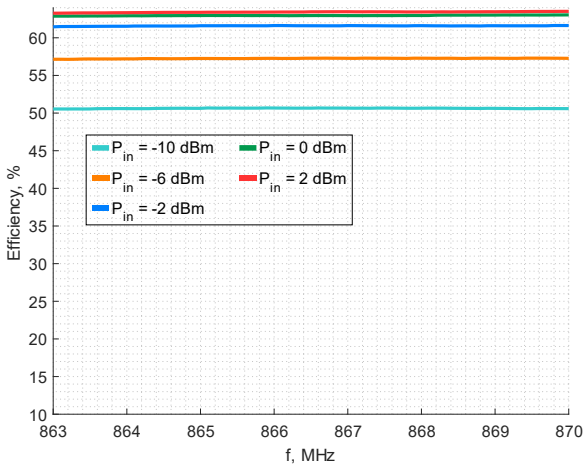

3.8 Fig. Matched RF-DC voltage multiplier conversion efficiency depending on sine signal frequency at different input power levels

After confirming the RF-DC rectifier's uniform performance across the frequency range from 863 to 870 MHz and different input signal power levels, another measurement series were performed. The 3 multitone signals were employed with 3 different bandwidths. In these measurements, HPAPR multitone with high PAPR level, LAPR multitone signal with low PAPR level, and RPAPR multitone signal with three different bandwidths: 50 KHz, 500 KHz, 5MHz with 8 subcarriers were employed. The rectified DC voltage a) and the power conversion efficiency b) of power conversion with the multitone signal bandwidths of 5 MHz, 500 KHz, and 50 KHz at 3 load resistor values are shown respectively in Fig. 3.9 to 3.11. For reference, the single-tone sine signal is also added to the figures.

The investigation of the performance of the rectifier with the multitone signal with the 5 MHz bandwidth shows that the power conversion of the HPAPR multitone signal resulted in a peak efficiency of 27 % at the 100 kΩ, 12 % at 10 kΩ and 2 % at 1 kΩ load resistor value, the conversion of the LPAPR multitone signal resulted in the peak efficiency of 33 % at the 100 kΩ, 63 % at 10 kΩ and 18 % at 1 kΩ load resistor value, the conversion of the RPAPR multitone signal resulted in the peak efficiency of 27 % at the 100 kΩ, 59 % at 10 kΩ and 16 % at 1 kΩ load resistor value. In comparison, the LPAPR and RPAPR multitone signals' power conversion efficiency was similar to the sine wave. However, the power conversion with the HPAPR signal yielded much less efficiency. Depending on the resistance load, the conversion efficiency between the LPAPR, RPAPR, and sine waveforms differed up to 7 %. The highest power conversion efficiency, around 58 to 65 % for multitone signals, except the HPAPR signal, is obtained using the 10 kΩ load resistance at the input power level of 0dBm. With the 100 kΩ load resistance, the peak power conversion efficiency is about 30%, with fluctuations up to 5% at 0 dBm input power level. With the load resistance value of 1 kΩ, the peak efficiency is around 18%, with fluctuations up to 5 % at –5 dBm input power level.

The rectifier's performance with the multitone signals with 500 kHz and 50 kHz bandwidth (see Fig. 3.10 and 3.11) shows a similar performance level with minor fluctuation of the power conversion efficiency. The power conversion efficiency measurements of the RF-DC rectifier with the matching network employing the multitone signals show that for this type of converter, the HPAPR multitone will convert much less power that the LPAPR and RPAPR waveforms at 8 subcarriers.

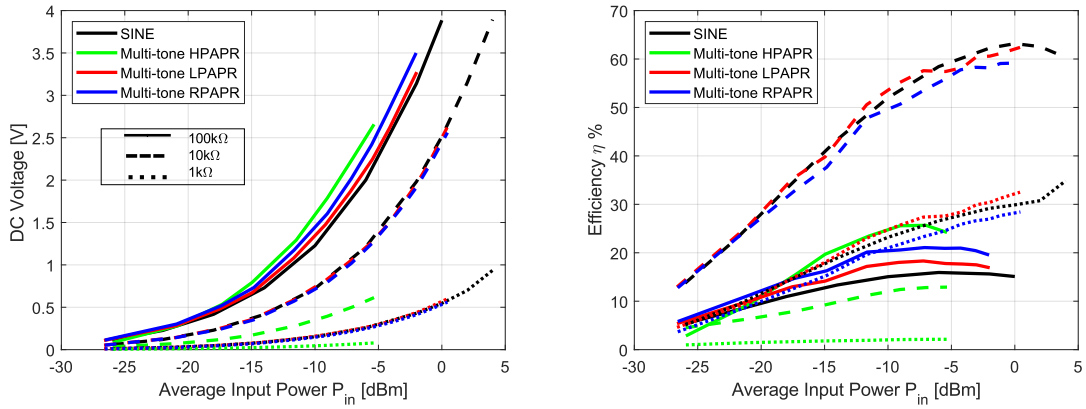

a) b)

Fig. 3.9. Matched RF-DC voltage doubler output voltage and conversion efficiency depending on the waveform and input power level with 5MHz bandwidth [35].

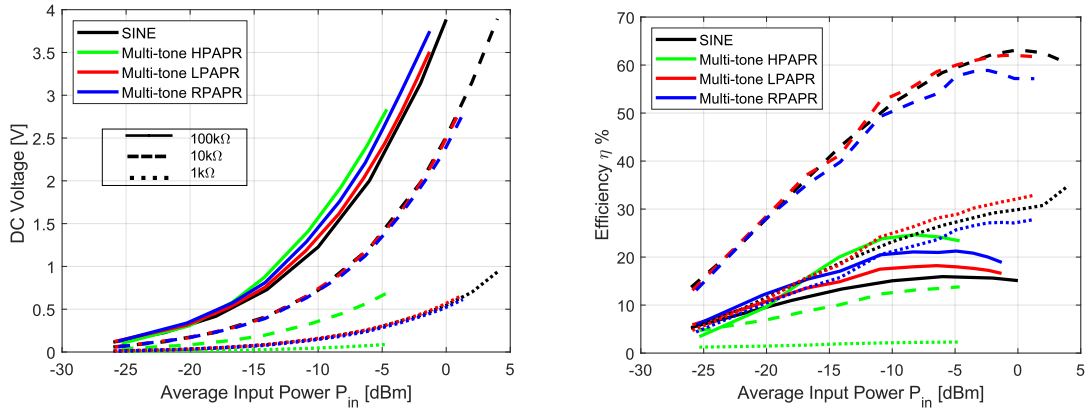

a) b)

Fig. 3.10. Matched RF-DC voltage doubler a) output voltage and b) conversion efficiency depending on the waveform with 500 kHz bandwidth [35].

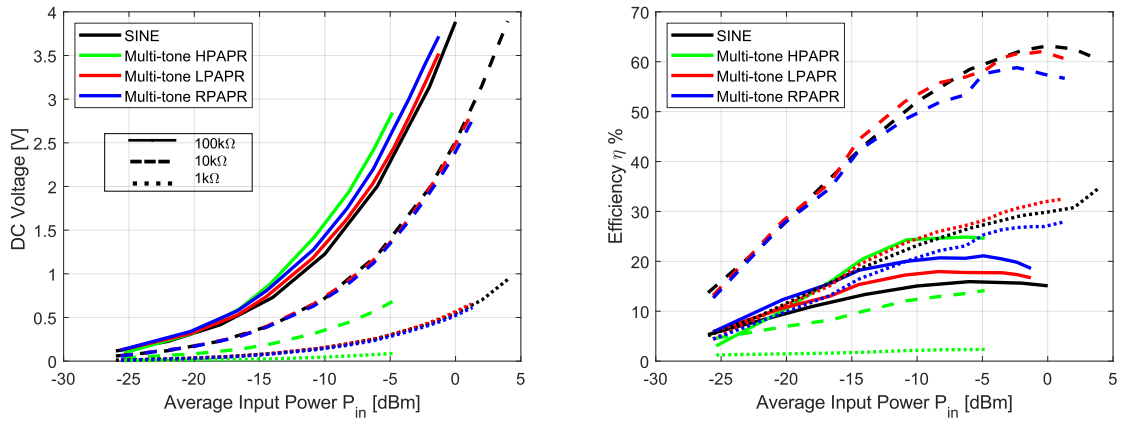

a) b)

Fig. 3.11. Matched RF-DC voltage doubler a) output voltage and b) conversion efficiency depending on the waveform and input power level with 50 kHz bandwidth [35].

The power conversion of the constant envelope signal produced similar power conversion efficiency as the sine waveform. The FM signal with 2 different modulation indexes was generated, and the voltage doublers rectified DC voltage and power conversion efficiency are shown in Fig. 3.12. At the lower input power level in the range from –17 dBm to –6 dBm, the difference between the sine waveform and FM modulated signal with a high modulation index is 10 %. However, with the input power increase, this difference decreases.

The linearly increasing frequency in a narrow-band CHIRP signal yields similar power conversion efficiency as the sine waveform, as shown in Fig. 3.13. At the lower input power level range from –17 to –11 dBm, the CHIRP signal is up to 15 % less efficient. However, with the input power level from –5 to 1 dBm, the efficiency with the CHIRP signal yield up to 10 % more. The RF-DC rectifier with the constant envelope signals delivers a similar output voltage at the same load resistance as the reference signal - sine wave.

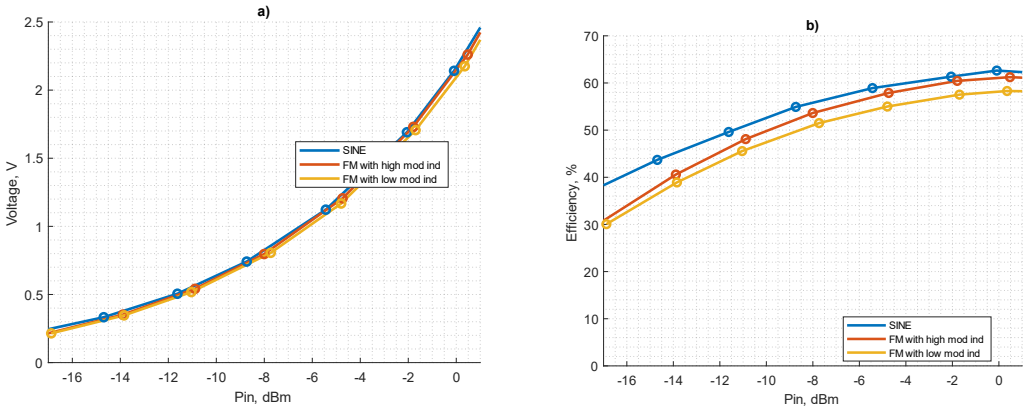

Fig. 3.12. Rectified a) DC voltage and b) conversion efficiency with FM tonal modulated signal with high modulation index and low modulation index employing RF-DC voltage doubler converter with matching network.

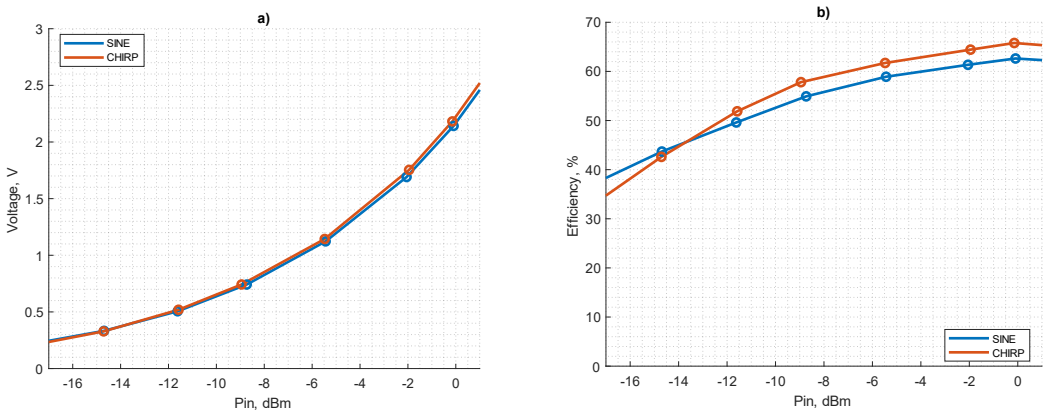

Fig. 3.13. Rectified a) DC voltage and b) conversion efficiency with CHIRP signal employing RF-DC voltage doubler converter with matching network at 7.5 kΩ.

3.1.5. Summary of the signal waveform impact on the power conversion efficiency

The reviewed signal waveforms in the RF-DC conversion with the voltage doubler with matching network show that the constant envelope signals and the LPAPR and RPAPR multitone waveforms provide similar power conversion efficiency as the sine with the voltage doubler rectifier with matching network. The multitone signal bandwidth impact on the rectifier is minimal and provides similar power conversion efficiency with the 50 kHz, 500 kHz, or 5 MHz bandwidth.

3.2. Impact of the number of multitone signal subcarriers on power conversion efficiency

3.2.1. Objective

This section is dedicated to the study of the subcarrier impact on the conversion efficiency with the RF-DC voltage doubler rectifiers with and without matching networks, and the Powercast P2110B module. This section will review 3 different multitone signal waveforms with a number of subcarriers ranging from 4 to 256. The RF-DC conversion load resistance impact will be evaluated with the different signal waveforms and subcarriers.

3.2.2. Tasks

To investigate the subcarrier number impact on the power conversion efficiency, the RF-DC measurement series will be performed with three types of signal waveforms: HPAPR, LPPAR, and RPAPR, with the number of subcarriers in the range from 4 to 256. The area of interest in these measurements is the multitone signal subcarrier impact on the power conversion efficiency, and in this case, with the HPAPR multitone waveform.

3.2.3. Measurement setup

The RF-DC power conversion measurement series were performed with 3 multitone signals: HPAPR, LPAPR, and RPAPR, with subcarriers ranging from 4 to 256. The

measurement setup and the signal generation algorithms are already described at the beginning of Chapter 3. In these experiments, the multitone signals were generated with a bandwidth of 5MHz. It has been already established in the previous measurement series that the larger signal bandwidth will not impact the power conversion efficiency for the RF-DC voltage doubler. For reference, the sine signal was also generated and added for comparison. The summary of signal parameters is given in Table 3.6.

Table 3.6

RF Signal Parameters

Signal waveform	Sine	HPAPR	LPAPR	RPAPR
Average power level	–17 dBm to 0 dBm			
Signal bandwidth	-	5 MHz		
Subcarriers	1	4–256		
PAPR level, dB	3	10–33	6–7.5	7.6–12

3.2.4. Experimental results

In these experiments, the multitone subcarrier impact on the RF-DC conversion efficiency was evaluated with 3 different signal waveforms: HPAPR, LPAPR, and RPAPR multitone. The RF-DC voltage doubler rectifiers' performance with the matching network is given in Figs. 3.14–3.16. The rectified DC voltage across the load resistance value is shown in graph a), and the power conversion efficiency is given in graph b).

The prototyped RF-DC rectifier's performance with the matching network employing the HPAPR multitone signal with different subcarriers is given in Fig. 3.14. The use of the multitone signals in the RF-DC power conversion with the voltage doubler topology shows that the power conversion depends not only on the signal waveform but also on the number of subcarriers. The HPAPR multitone use with the matched rectifier shows that the increase of the subcarrier number decreases the converted output voltage across the resistance load. The power conversion efficiency overall is lower than using the sine signal. The power conversion employing HPAPR multitone with the 4 subcarriers provides peak efficiency up to 45 %, 8 subcarriers up to 36 %, 16 subcarriers up to 26 %, 32 subcarriers 17 %, 64 subcarriers up to 10 %, 128 subcarriers up to 6 %, 256 subcarriers up to 2 %. The average input power level for the higher subcarrier number was decreased due to the increasing peak-to-peak voltages of the multitone signal. The average input power level has been reduced to prevent damaging the RF-DC converter diodes and meet the safe voltage operation point for the rectifier.

The power conversion of the RF-DC voltage doubler topology with the matching circuit employing the LAPR multitone signal is shown in Fig. 3.16. Similar rectified voltage levels and power conversion efficiency across all selected subcarriers numbers ranging from 4–256 subcarriers could be observed. At the lower input power level at –17 dBm power level, the LPAPR multitone rectification yields 7 % less efficiency than conversion with the sine

waveform, gradually decreasing the difference between the two signal waveforms at the average input power level of the –12 dBm.

The rectified DC voltage and the efficiency of the RF-DC voltage doubler with the matching network with the RPAPR input signal with subcarriers in the range from 4–256 are shown in Fig. 3.16. The RPAPR multitone signal for the RF-DC rectifier with the matching network shows overall lower power conversion efficiency than the use of the sine signal. The converted power from the Signal's frequency impact; multitone signals are lower consistently from 2 % to 10 % depending on the number of subcarriers compared to the sine signal.

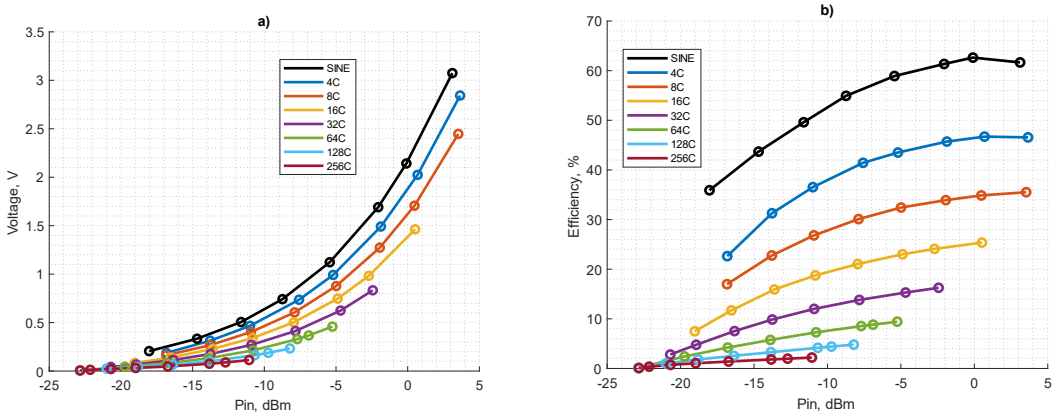

Fig. 3.14. Rectified a) DC voltage and b) conversion efficiency with HPAPR multitone signal with subcarrier count from 4 to 256 employing the RF-DC voltage doubler converter with matching network.

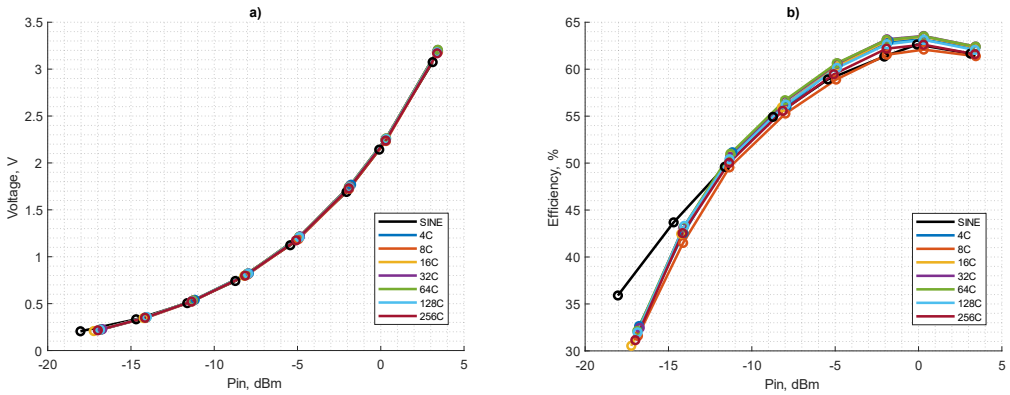

Fig. 3.15. Rectified a) DC voltage and b) conversion efficiency with LPAPR multitone signal with subcarrier count from 4 to 256 employing the RF-DC voltage doubler converter with matching network.

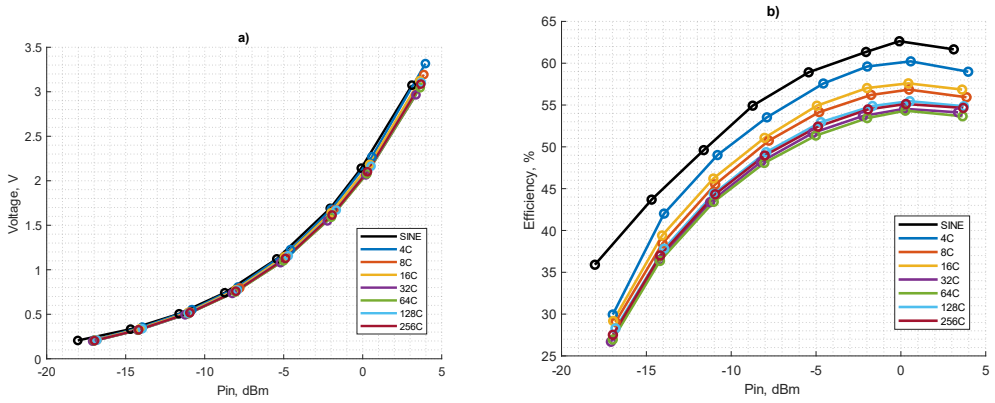

Fig. 3.16. Rectified a) DC voltage and b) conversion efficiency with RPAPR multitone signal (random carrier amplitude and phase) with subcarrier count from 4 to 256 employing the RF-DC voltage doubler converter with matching network.

To evaluate the difference between the rectified DC voltage with sine signal and other signal waveforms, another quantifying unit for comparison was necessary - the mean square difference between the rectified DC voltage with the signal waveform is compared to the DC voltage using the sine waveform:

$$MSE = \frac{\sum_{n=1}^{N}(\hat{s}_n - s_n)^2}{N} * 100 \quad (3.3)$$

where MSE – mean squared error in percent, $\hat{s}-$ signal for comparison, $s-$ reference signal, $N-$ number of comparison and reference signal pair samples.

The mean square difference between the rectified DC voltage with the RF-DC voltage doubler with the matching network is shown in Table 3.7. The results show that the mean square difference for the rectified voltage with the LPAPR and RPAPR multitone signal waveforms with the subcarriers in the range from 4 to 256, 2 FM modulated signals have a difference of less than 2% in comparison to the rectified voltage using a sine wave as an input signal.

Table 3.7.

Mean squared difference of the rectified voltage with different signal waveforms.

Signal waveform	subcarriers	Mean squared difference between rectified DC voltage compared to rectified DC voltage using sine, in percentage	
		Voltage doubler with matching network	Powercast P2110B module
FM with high mod index	-	0.83 %	2.17 %
FM with low mod index	-	0.13%	1.04 %
LPAPR multitone	4	0.59 %	1.77 %
	8	0.39 %	1.71%
	16	0.48 %	1.76 %
	32	0.63 %	1.96 %
	64	0.62 %	1.88 %

	128	0.51 %	1.68 %
	256	0.33 %	1.38 %
RPAPR multitone	4	1.16 %	3.47 %
	8	0.25 %	2.65 %
	16	0.11 %	1.57 %
	32	0.50 %	0.69 %
	64	0.20 %	1.59 %
	128	0.05 %	2.33 %
	256	0.10 %	1.74 %

The performance of the prototyped RF-DC voltage doubler with the matching network using multitone signals was also compared with the commercially available RF-DC conversion module Powercast P2110B. The performance of the commercially available RF-DC converter is shown in Fig. 3.17, where the rectified voltage a) and the power conversion efficiency b) depending on the HPAPR multitone input signal average power level and different subcarrier value is shown.

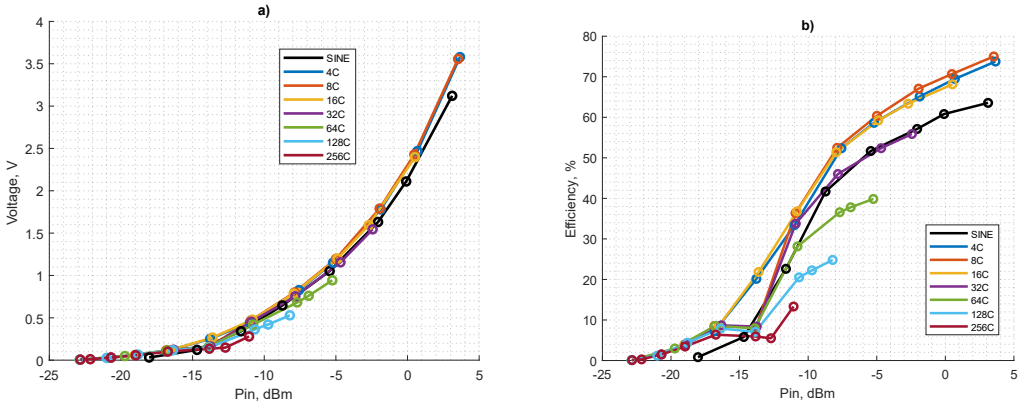

Fig. 3.17. Rectified a) DC voltage and b) conversion efficiency with high PAPR multitone signal with subcarrier count from 4 to 256 employing the RF-DC converter module Powercast P2110B.

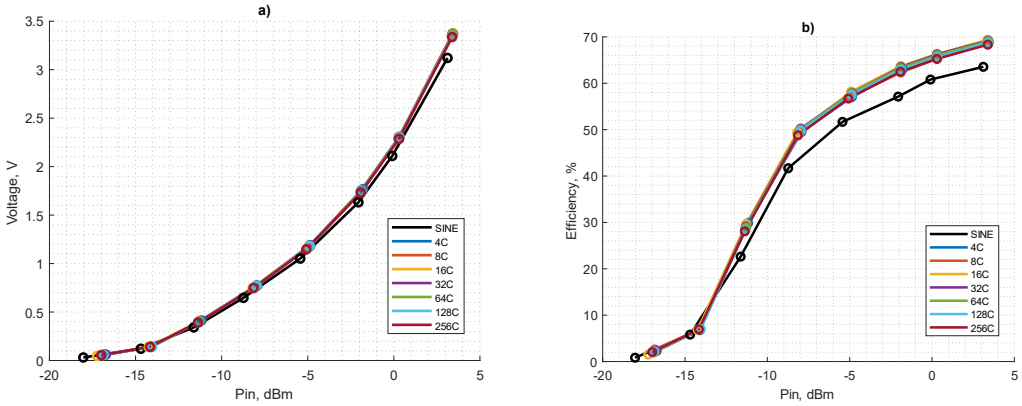

Fig. 3.18. Rectified a) DC voltage and b) conversion efficiency with low PAPR multitone signal with subcarrier count from 4 to 256 employing the RF-DC converter module Powercast P2110B.

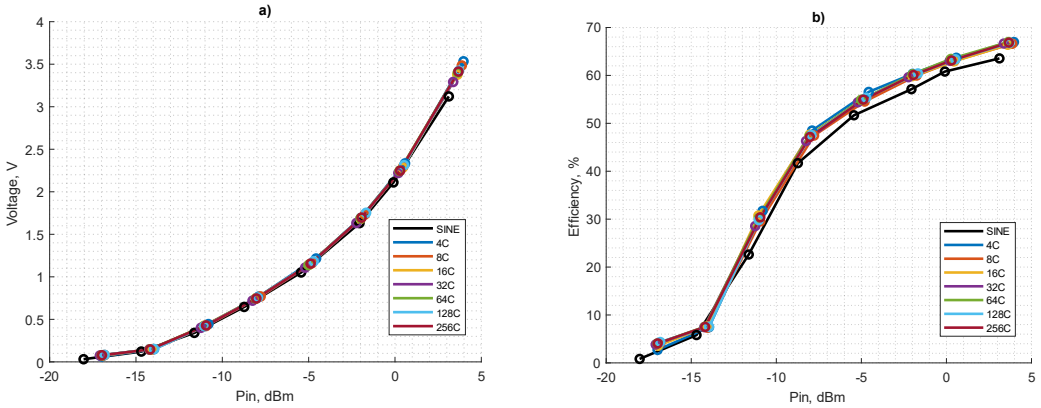

Fig. 3.19. Rectified a) DC voltage and b) conversion efficiency with RPAPR multitone signal (random carrier amplitude and phase) with subcarrier count from 4 to 256 employing the RF-DC converter module Powercast P2110B.

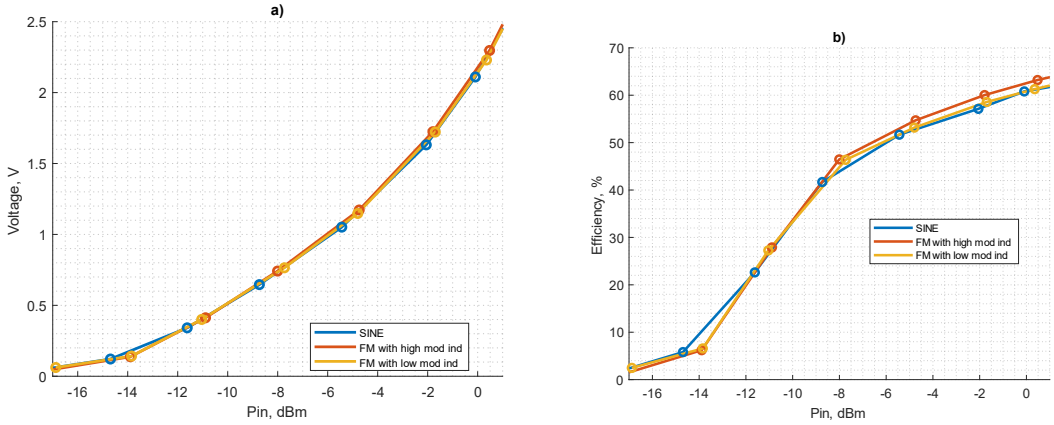

Fig. 3.20. Rectified a) DC voltage and b) conversion efficiency with an FM tonal modulated signal with high modulation index and low modulation index employing the RF-DC converter module Powercast P2110B.

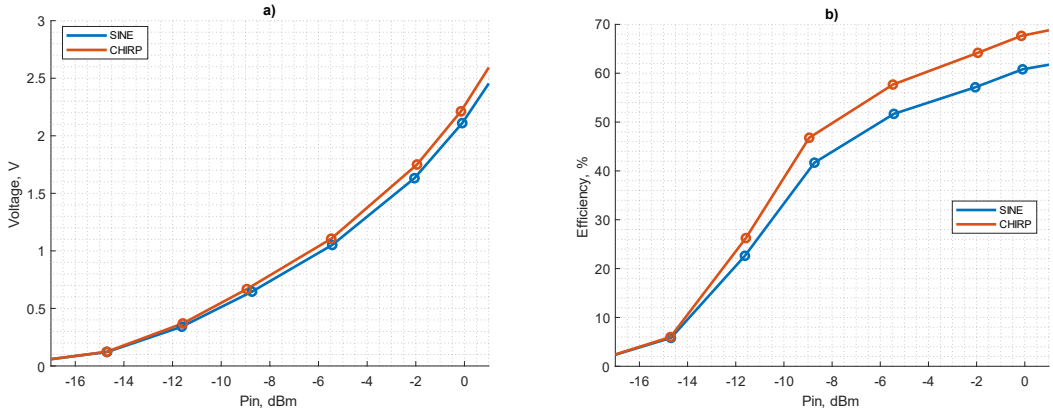

Fig. 3.21. Rectified a) DC voltage and b) conversion efficiency with CHIRP signal employing the RF-DC converter module Powercast P2110B.

The Powercast overall converter's performance with HPAPR multitone signal waveform shows a similar trend as with the RF-DC voltage doubler with the matching network: increasing the number of subcarriers leads to the decrease of the overall power conversion efficiency at

the same input power level. However, the efficiency decrease with the Powercast module is less steep compared to the voltage doubler. The power conversion efficiency with the HPAPR multitone signal with 4, 8, 16 subcarriers yields up to 10 % more efficiency than the rectification of the sine signal waveform, respectively, 68 %, 70 % and 67 % efficiency, at the 0 dBm input power level. In contrast, the sine waveform power conversion gives only 61 % efficiency. The Powercast module's power conversion with HPAPR multitone signal with 32 subcarriers yields the same power conversion efficiency as the sine waveform. The power conversion efficiency with the HPAPR multitone signals with 64 and more subcarriers decreases as the subcarrier number increases and yields lower efficiency.

RF-DC power conversion of the Powercast modules using the LPAPR and RPAPR multitone signals shows a similar trend as the RF-DC voltage doubler rectifier with a matching network. The number of subcarriers of the LPAPR and RPAPR multitone signal has minimal impact on the power conversion efficiency with the Powercast module. The converter delivers the same power conversion efficiency irrespective of the tested subcarrier number (see Fig. 3.18 and 3.19). The power conversion efficiency with the LPAPR multitone will provide up to 8 % higher efficiency than the sine waveform for the input power level from – 13 dBm to 2 dBm, with the subcarriers in the range from 4 to 256, reaching 70 % efficiency at 3 dBm input power level with the LPAPR waveforms and 63 % with the sine waveform.

The RPAPR signal waveform power conversion with the Powercast module performs similarly to the sine waveform, reaching a peak efficiency of 65 %, with up to 2 % fluctuation from the power conversion efficiency compared to a sine wave.

The rectified DC voltage and the power conversion efficiency performance with the FM tonal modulated FM signals, CHIRP is similar, with less than 2 % efficiency difference between the power conversion efficiency using a sine wave, shown in Fig. 3.20 and 3.21.

The comparison of the rectified DC voltage means the square difference between a sine wave and other signal waveforms with the Powercast P2110B module is shown in Table 3.6. The Powercast module exhibits RF-DC power conversion trends similar to the voltage doubler circuit with the matching network. The rectified LPAPR and RPAPR multitone signals and tonally modulated FM signals give a similar output DC voltage as the sine waveform.

The previous experimental data shows that the power conversion efficiency is dependent on the signal waveform, input power level, and resistance load with the sine wave; it is hypothesized that the power conversion with different waveform signals will also be dependent on the input power level and load resistance. The RF-DC conversion is also dependent on the frequency. However, the performed frequency measurements show the voltage doubler with the matching network can be considered frequency independent in the specified ISM frequency range from 863 to 870 MHz. Therefore, additional RF-DC power conversion experiments were performed, where the load resistance value varied from 1kΩ to 200 kΩ. The following measurements with the variable resistor load were performed with a voltage doubler converter. Another measurement series were performed with the RF-DC voltage doubler with the matching network using different level multitone signals with a number of subcarriers from 4 to 64.

The LPAPR multitone signal has similar PAPR level as the RPAPR multitone signal. Therefore, only HPAPR and the LPAPR multitone signal waveforms were investigated for the power conversion efficiency dependence from the load resistance value, see Figs. 3.22 and 3.23, where the rectified DC voltage is shown in part a) and the power conversion efficiency is shown in part b). The results show that using the HPAPR multitone signal, the resistance value at which the most efficiency is achieved changes depending on the number of subcarriers. For example, when using the HPAPR multitone signal with the 4 subcarriers, the most optimal load resistance value is 23 kΩ, with 8 subcarriers multitone signal 35 kΩ, with 16 subcarriers multitone signal 55 kΩ, with 32 subcarriers multitone signal 73 kΩ, with 64 subcarriers multitone signal 81 kΩ, also, with the subcarrier increase, the peak efficiency achievable decreases. The advantage of the HPAPR signal is that the rectifier's DC voltage is higher at higher ohmic load resistance than using other signal waveforms, which can be beneficial when the harvested input power level is low.

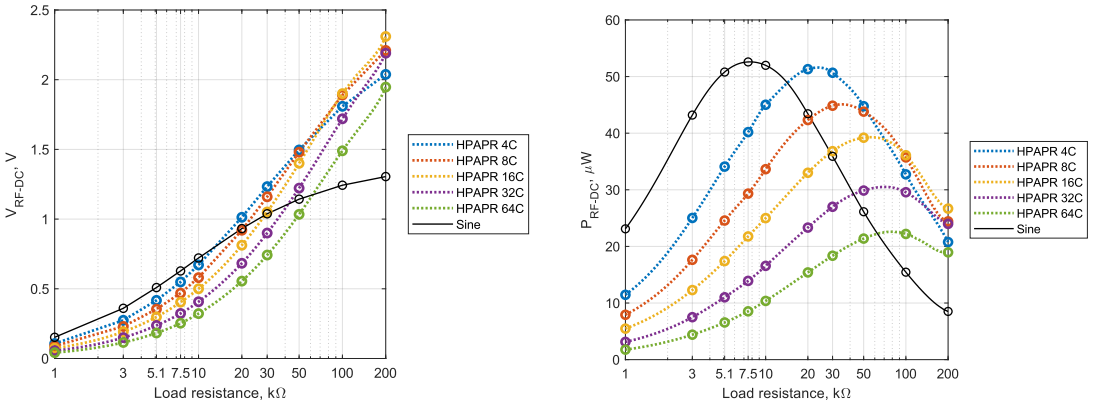

Fig. 3.22. Rectified a) DC voltage and b) conversion efficiency with high PAPR level multitone signal with subcarrier count from 4 to 64 employing the RF-DC voltage doubler converter with matching network with different load resistance value at -10 dBm input power level.

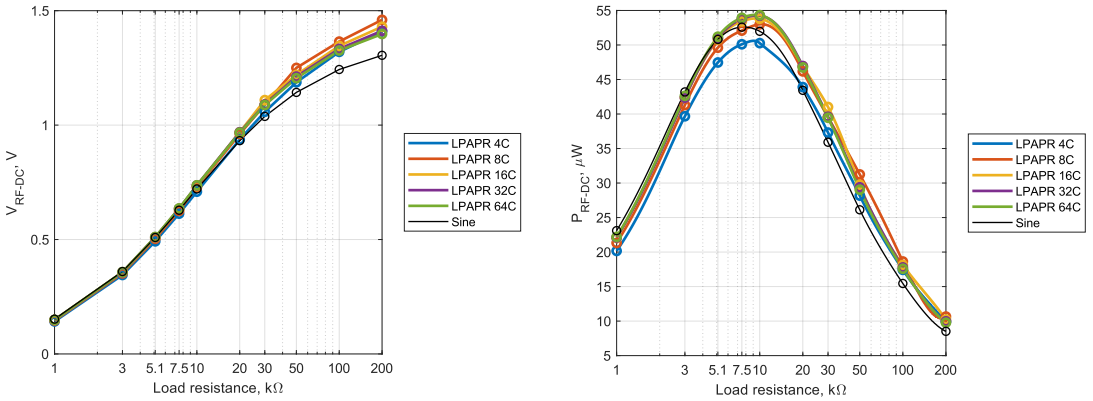

Fig. 3.23. Rectified a) DC voltage and b) conversion efficiency with low PAPR level multitone signal with subcarrier count from 4 to 64 employing the RF-DC voltage doubler converter with matching network with different load resistance value at -10 dBm input power level

The rectification of the LPAPR signal waveform depending on the load resistor value shows similar DC voltage and the power conversion efficiency as with the sine waveform. The resistance value at which the voltage doubler with the matching network achieves the peak power conversion stays in the same range: 9 to 10 kΩ. The peak power conversion efficiency with the corresponding load resistance value and the rectified DC voltage levels for the different signal waveforms are given in Table 3.8.

Table 3.8.

RF-DC voltage doubler with the matching network peak voltage and power parameters depending on the load resistance

Signals	Carrier number	Matched resistance load value, kΩ	Output voltage at the matched resistance load, V	Conversion efficiency, %
Sine	1	7.72	0.64	52.59
Multitone signal with same amplitudes and phases (HPAPR)	4	23.77	1.10	51.59
	8	35.88	1.27	45.00
	16	55.88	1.48	39.29
	32	73.50	1.49	30.50
	64	81.00	1.35	22.59
Multitone signal with same amplitudes and different phases (LPAPR)	4	9.119	0.67	50.6
	8	10.20	0.735	53.01
	16	9.41	0.711	53.85
	32	9.41	0.714	54.27
	64	9.41	0.715	54.37

3.2.5. Summary of impact of the number of multitone signal subcarriers on the power conversion efficiency

The FM modulated, CHIRP, LPAPR, and RPAPR multitone signal use in the power conversion with the RF-DC voltage doubler rectifier with the matching network with subcarriers in the range from 4 to 256 give less than 2% of the rectified mean square voltage difference compared to the use of the sine waveform. These measurement results also show that signals used in wireless communications with low PAPR levels can be used in the WPT or energy harvesting. The measurements with the voltage doubler with the matching network using the HPAPR multitone signals in the ISM sub-GHz frequency range from 863 to 870 MHz show that the load resistance value must be adjusted appropriately depending on the number of subcarriers to reach the peak power conversion.

3.3. Matching network impact on the RF-DC conversion efficiency

3.3.1. Objective

This experiment series is dedicated to the study of the matching network impact on the RF-DC power conversion efficiency. This section studies the voltage doubler with and without the matching network with the HPAPR multitone signal.

3.3.2. Tasks

This research aims to evaluate the impact of the matching network on the power conversion efficiency; therefore, the same rectifier with and without the matching network was prototyped. The RF-DC rectifier topology was selected to be the voltage doubler. The RF-DC power conversion efficiency measurements were performed with high PAPR level multitone signals.

3.3.3. Measurement setup and experiments

The measurements are divided into two parts: 1) the signal average input power level is measured for all the signals employed in this experiment; and 2) the signal is fed to the rectifier and the rectified voltage level is measured for the corresponding input power level.

The measurements of the rectified DC voltage across the load resistor were performed with the two RF-DC voltage doubler boards: one with the matching network, another without the matching network, employing high PAPR level multitone signal – HPAPR. The number of multitone signal subcarriers was varied in range from 4 to 256. The multitone signal bandwidth was set to 5 MHz, and the input power level was changed in the range from – 17 dBm to 0 dBm power level; the signal parameters are shown in Table 3.9.

Table 3.9

RF Signal Parameters

Signal waveform	Sine	HPAPR	LPAPR	RPAPR	FM	CHIRP
Average power level	–17 dBm to 0 dBm					
Signal bandwidth	-	5 MHz			5 MHz	150 kHz
Subcarriers	1	4–256			Modulation index 4.8, 48	-
PAPR level, dB	3	10–33	6–7.5	7.6–12	3	3

3.3.4. Experimental results

The power conversion measurements have been performed for the RF-DC rectifier with matching network and without matching network with the voltage doubler topology. The power conversion measurements with different signal waveforms have been produced, including constant envelope and varying envelope signals.

The measurements were performed with the multitone signal with a high PAPR level using the rectifier without the matching network. Figure 3.24 shows the performance of RF-DC

voltage doublers without the matching network with the high PAPR level multitone signals: a) rectified DC voltage in and b)power conversion efficiency. The rectified DC voltage level is dependent on the number of subcarriers. Fig. 3.25 shows the average rectified DC voltage level and the power conversion efficiency with HPAPR multitone signals at – 12 dBm input power level depending on the subcarriers. The power conversion efficiency depends on the number of subcarriers. The trend is an inverse parabolic curve, where the highest power conversion level is achieved with the 32 subcarriers, and power conversion with other subcarrier values will convert less voltage level and, therefore, less efficiency.

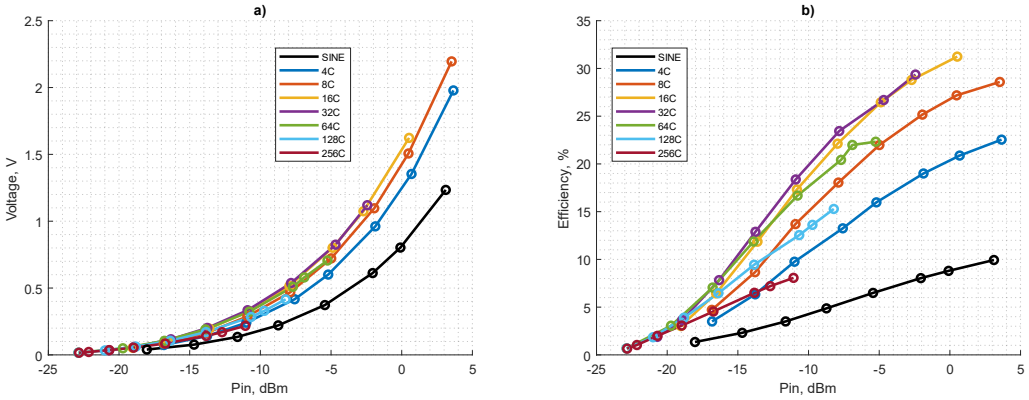

Fig. 3.24. Rectified a) DC voltage and b) conversion efficiency with high PAPR multitone signal with subcarrier count from 4 to 256 employing the RF-DC voltage doubler converter without matching network.

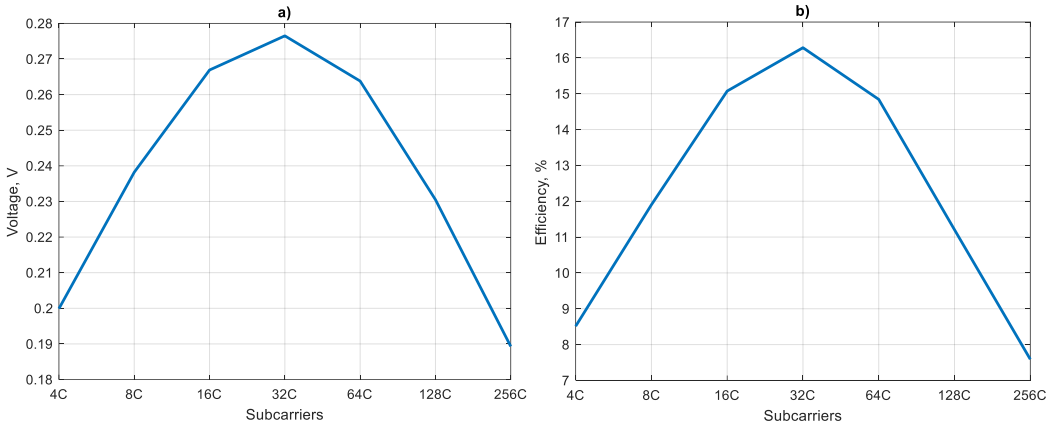

Fig. 3.25. Rectified a) DC voltage and b) conversion efficiency with high PAPR multitone signal input signal at –12 dBm power level with subcarrier count from 4 to 256 employing the RF-DC voltage doubler converter without matching network.

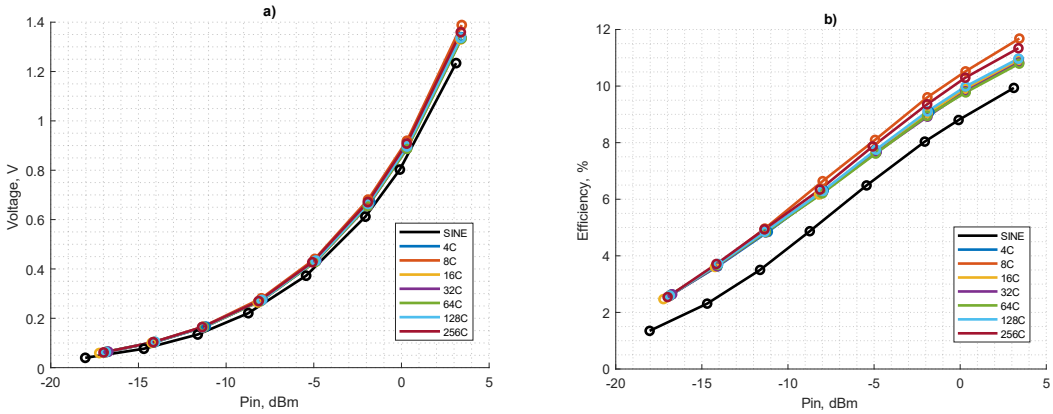

Fig. 3.26. Rectified a) DC voltage and b) conversion efficiency with low PAPR multitone signal with subcarrier count from 4 to 256 employing the RF-DC voltage doubler converter without matching network.

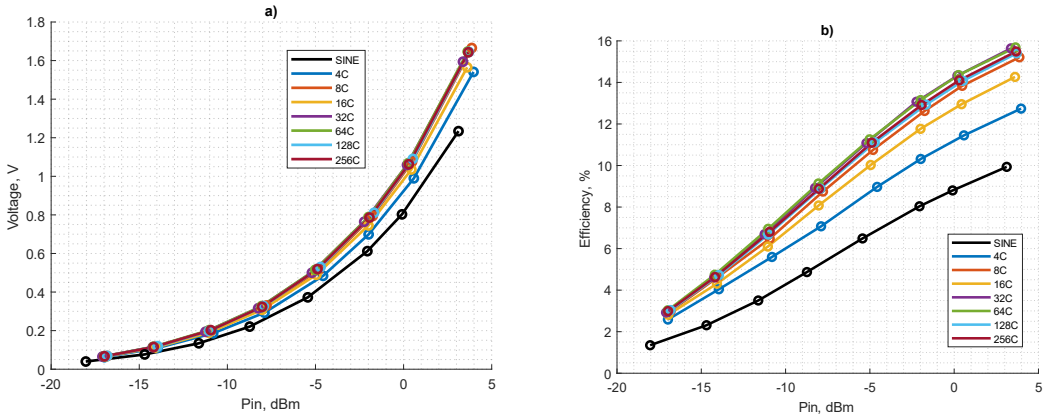

Fig. 3.27. Rectified a) DC voltage and b) conversion efficiency with RPAPR multitone signal with subcarrier count from 4 to 256 employing the RF-DC voltage doubler converter without matching network.

The converter's performance with the low PAPR multitone signal is relatively low, and power conversion efficiency at 3dBm input power level reaches less than 12 %. Similar performance is also observed with the sine waveform, shown in Fig.3.26. The subcarrier impact on the power conversion efficiency is negligible, and in the range of subcarriers from 4 to 256 changes only less than 1 %.

A similar power conversion efficiency level is also observed with the RPAPR multitone signals with the subcarriers in the range from 4 to 256, shown in Fig. 3.27., where at the input power level of 3dBm, the efficiency does not exceed 16 %. As the subcarrier amplitudes and phases are randomly generated, the subcarrier impact on the power conversion efficiency is a few percent above the multitone signal compared to the sine wave.

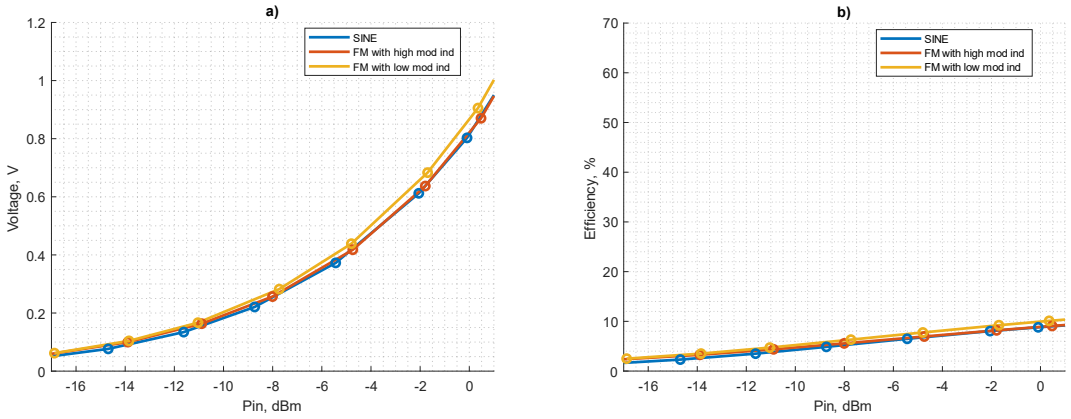

Fig. 3.28. Rectified a) DC voltage and b) conversion efficiency with FM tonal modulated signal with high modulation index and a low modulation index employing RF-DC voltage doubler converter without matching network.

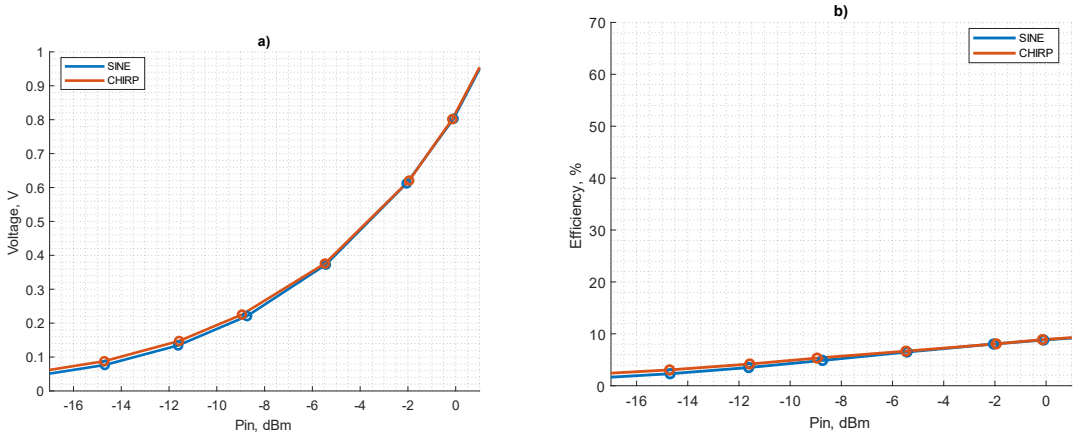

Fig. 3.29. Rectified a) DC voltage and b) conversion efficiency with CHIRP signal employing RF-DC voltage doubler converter with matching network

The voltage doublers RF-DC power conversion with the FM modulated signal waveform, shown in Fig. 3.28 and CHIRP signal, shown in Fig. 3.29, performs very similarly when employing the sine waveform and the difference between these values is less than a few percent, reaching the peak efficiency 9 % at the 1 dBm input power level.

The matching network circuit impact on the power conversion depending on the subcarriers is shown in Fig. 2.30 – 2.31. The rectifiers converted voltage level, and the power conversion efficiency is shown at the different subcarriers.

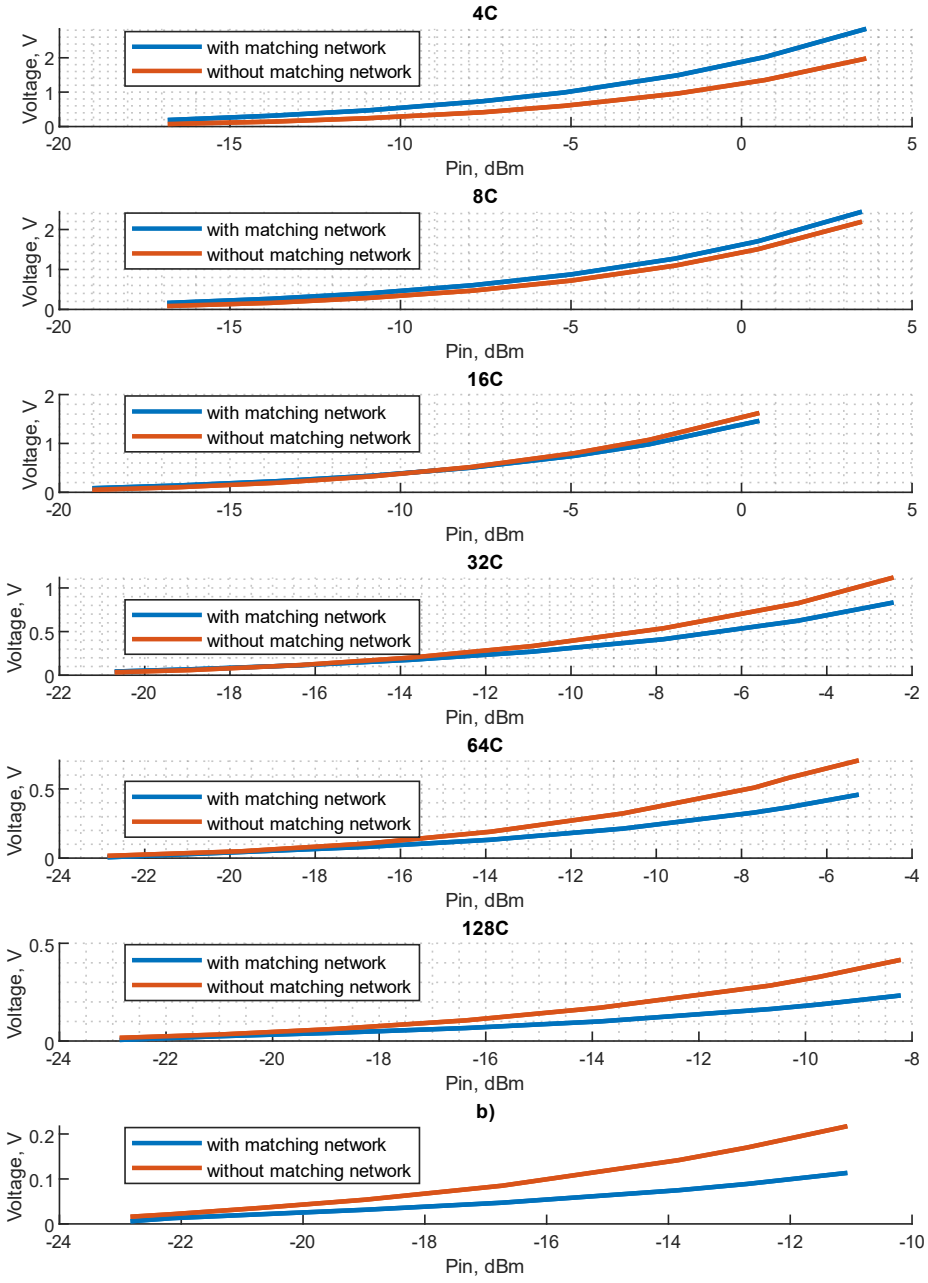

Fig. 3.30. Rectified DC voltage with PAPR multitone signal with subcarrier count from 4 to 256 employing the RF-DC voltage doubler converter with and without matching network.

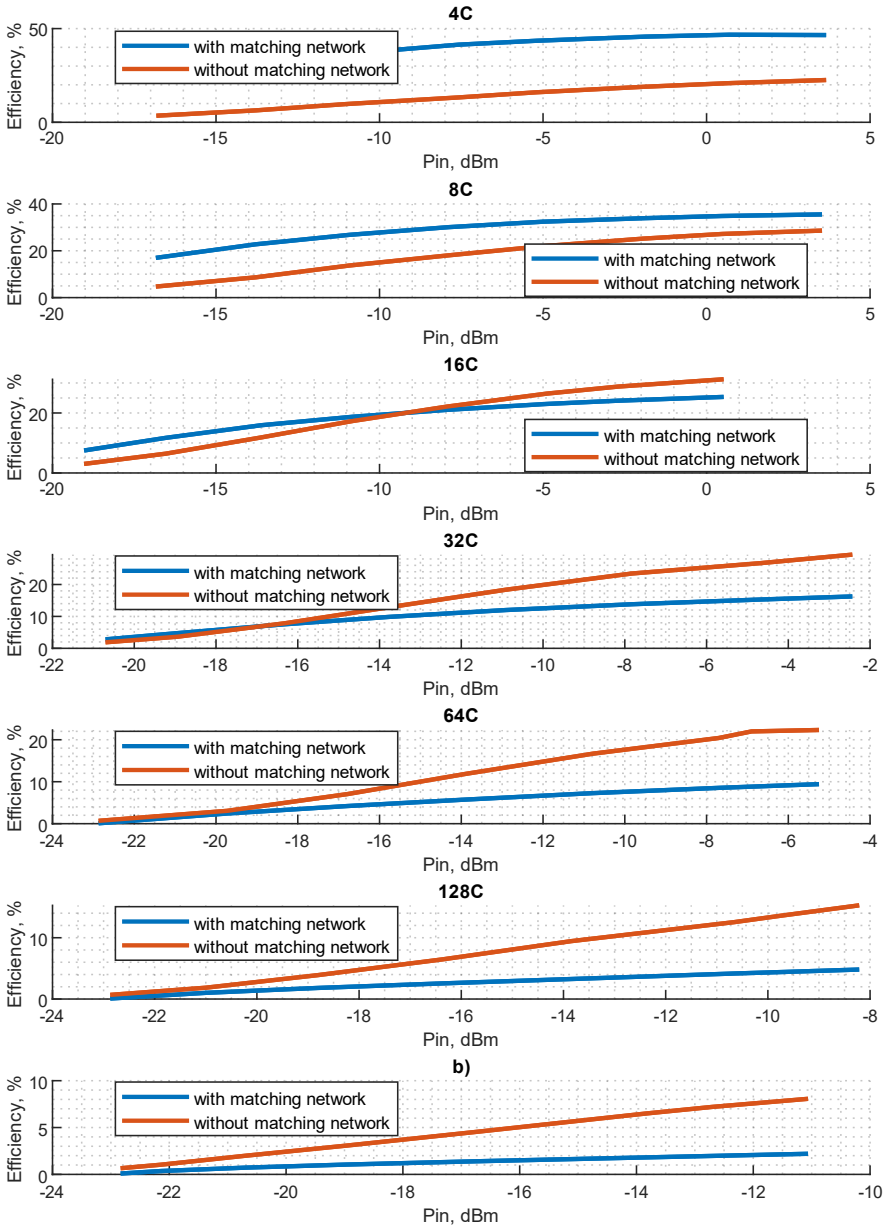

Fig. 3.31. The power conversion efficiency with PAPR multitone signal with subcarrier count from 4 to 256 employing the RF-DC voltage doubler converter with and without matching network.

The RF-DC voltage doublers' performance results with the matching network and without the matching network with the HPAPR multitone signal are shown in Fig. 3.31. The trend of the rectified voltage level for a converter with the matching network is as follows: as the number of multitone subcarriers increase, the rectified voltage level decreases, i.e., the rectified voltage

at -10 dBm input power level with the 4 tone signals gives around 0.53 V, with 8 tones 0.45 V, with 16 tones 0.37 V, with 64 tones 0.31 V, with 64 tones 0.23 V, with 128 tones 0.18 V.

Another trend is observed for the voltage doubler rectifier without the matching network. The higher subcarrier number HPAPR multitone signal used in power conversion gives a smaller DC voltage level. The rectified voltage level with the HPAPR multitone signal with an average input power level of -10 dBm power level with 4 tone signal gives 0.28 V, with the 8 tones gives 0.37 V, with 32 tones provide 0.38 V, with 64 tone signal 0.36 V, with 128 tone signal gives 0.31 V DC voltage across the resistor.

However, above specific subcarrier number values, the rectifier without the matching network outperforms the rectifier with the matching network. In this experiment, using the HPAPR signal with the subcarriers up to 8 subcarriers, the rectified DC voltage is higher employing the converter with the matching network; with the 16 subcarriers HPAPR multitone signal, the rectified DC voltage is around the same value, with the subcarrier value above 16, the rectifier without the matching network gives higher DC voltage level.

3.3.5. Summary of impact of matching network on the RF-DC conversion efficiency

The impact of the matching network on voltage doubler topology with different signal waveforms has been evaluated. The power conversion employing LPAPR multitone signals with the rectifier without the matching network has a similar performance as the sine waveform and the RPAPR multitone signals. In comparison, the impact of the number of multitone subcarriers is limited with the LPAPR multitone and the RPAPR multitone, where efficiency fluctuates correspondingly less than 2 % and 4 % for the tones in the range from 4 to 256. The situation is different with the high PAPR level multitone signals. The power conversion trend of the rectifier with a matching network shows that the increase in subcarrier value will lead to a decrease in the power conversion efficiency. For the RF-DC converter without the matching network, the situation is similar. However, there is a corresponding subcarrier value, where the increase of the subcarrier will yield a higher efficiency level than the converter with matching network. The use of the CHIRP signal in power conversion also shows similar power conversion efficiency to the sine waveform, as this signal has the same PAPR level as the sine waveform.

3.4. Conclusions on experimental study on RF-DC conversion efficiency

In the current chapter, the impact of properties of the RF power-carrying signals on RF-DC conversion efficiency for the prototyped RF-DC rectifiers – voltage doubler with and without matching network is evaluated. The experimental study is performed in ISM 863-870 MHz frequency range. The analysed signals have a constant or varying envelope, different levels of average input power, different bandwidths, number of multicarriers, and PAPR level.

During the study, the following main conclusions have been made:

- The constant envelope signals (sine, FM modulated, CHIRP) and the LPAPR and RPAPR multitone waveforms provide the same power conversion efficiency in the case of the voltage doubler rectifier with a matching network.
- The impact of the multitone signal bandwidth on the rectifier performance is minimal for all observed cases (50 KHz, 500 KHz, or 5 MHz).
- The adjustment of the load resistance in correspondence to the the number of HPAPR subcarriers increases the RF-DC conversion efficiency for the voltage doubler with the matching network.
- The number of subcarriers in the employment of LPAPR and RPAPR multitone power-carrying signals and the voltage doubler without a matching network does not sufficiently impact the RF-DC conversion efficiency.
- The increase in number of HPAPR subcarriers leads to a decrease in the power conversion efficiency in the case of a voltage doubler with a matching network.

4. Experimental study on WPT performance

The development of the wireless channel models presents tradeoffs between the precision of the model – depicted by the number of physical effects and material properties considered - and the computational time and resources. While the most precise model is desirable, the computational time and power are strictly limiting factors, meaning that reasonably simplified models can have broader applications. However, the results in different environments may present discrepancies that cannot be accounted for with the simulations. The experimental study of the WPT performance aids in developing the theoretical model by narrowing the set of physical properties of the channel down to the most significant ones.

For this reason, experimental studies of the WPT performance in the laboratory were performed. The experimental studies focused on determining the essential transmission parameters by their impacts on the amount of the harvested energy using RF-DC converters. In this investigation, the parameters of interest that influence the WPT are:

- distance between the transmitting and receiving antennas;
- antenna type impact on the harvesting level indoors;
- signal's frequency impact;
- signal's waveform impact.

4.1. MEASUREMENT SETUP

This section describes the measurement setup used to perform the experimental studies mentioned on the parameters of the WPT. The measurements were performed using the setup demonstrated in Fig 4.1. The signal is generated in real-time using MATLAB/SIMULINK software and transferred to software-defined radio (SDR) USRP B210. The signals generated by the SDR were also amplified using an external amplifier based on the MMG3006NT1 and MW7IC008N integrated circuits. In the receiver, the antenna's output is connected to the RF-DC converter, and the output power of the RF-DC converter is measured using the Keysight PSMU B2910A device.

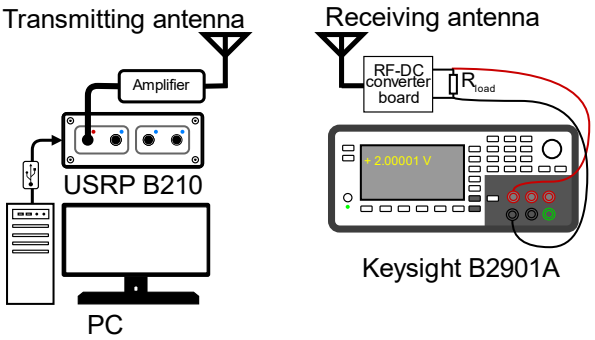

Fig. 4.1. Measurement setup for WPT parametric characterization [89].

4.2. Study of the factors influencing the WPT efficiency

The first study aimed to determine how the power-carrying signal's frequency impacts the received power level. The measurements were performed for several power-carrying signal frequencies and distances between the two antennas. The signal waveform was a sine wave with a 22.3 dBm power level. This experiment swept the power-carrying signal's frequency from 863 MHz to 870 MHz (ISM band), with antenna distances varied from 0.6 to 3 m (1.73 to 8.6 wavelengths), measuring the average output power of the receiving antenna on the 50 Ω load. The antennas were placed at 1m in height. Two different pairs of antennas were employed for the measurements: LP0410 directional antennas with a gain of 6 dBi each VERT900 omnidirectional antennas with a gain of 3 dBi each. The used antennas are shown in Figure 4.2.

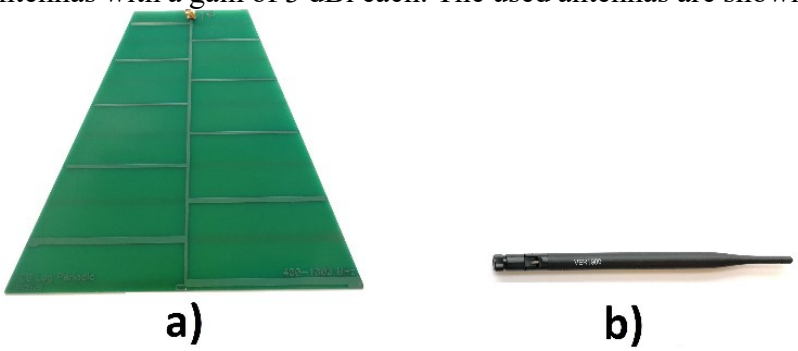

Fig. 4.2. Antennas used for the experimental setup: a) LP0410, b) VERT900.

The second study aimed to investigate how the different power-carrying signal waveforms influence the harvested voltage from WPT and the impact of the signal characteristics such as the signal's central frequency, bandwidth, and waveform. This experiment was performed for the voltage doubler-based prototype and the commercially available Powercast P2110B module [90]. The load of the Powercast was also set to 7.5 kΩ. The purpose of performing measurements with different RF-DC converters is to compare the performance of the commercially available RF-DC converter to the developed prototype.

This study employed power-carrying signals with different waveforms.
The signals are:

- Waveforms are formed by adding a certain number of sine waves (subcarriers) with different frequencies arranged to form a uniform spectrum with equal amplitudes and phases. Such signals posse a high peak-to-average power ratio (high PAPR) and, therefore, for notational simplicity, were termed HPAPR signals. The HPAPR signals considered in the present study have 4, 8, 16, 32, and 64 subcarriers.
- Waveforms are formed by adding a certain number (4-256) of sine waves with different frequencies (forming a uniform spectrum) and with amplitudes and phases generated using Zadoff-Chu sequences and an inverse fast Fourier transform (IFFT). Such signals exhibit a low peak-to-average power ratio (low PAPR), and hereafter are referred to as LPAPR signals.
- Waveforms are formed by adding a certain number (4-256) of sine waves with different frequencies (forming a uniform spectrum) and random amplitudes and phases following a uniform distribution. The PAPR level for this kind of signal can take arbitrary values, depending on a random combination of amplitude and phase values. This signal, therefore, is referred to as RPAPR.

The third study investigated how the frequency-modulated (FM) power-carrying signal with different modulation indexes influences the harvested voltage from WPT. The

investigation of such waveform is motivated by the potential applications for simultaneous wireless information and power transfer (SWIPT).

4.2.1. Signal frequency impact on the WPT efficiency.

This subsection investigates the WPT measurements and the rectified voltage level depending on the signal waveform, the distance between the transmitting and receiving antennas and different antenna types. The first study results are presented in Fig. 4.3 and 4.4. The directional antenna LP0410 is given in Fig 4.3, along with the omnidirectional antenna VERT900 in Fig.4.4. The curves in these figures display the output power of the receiver's antenna at the said distances between the antennas expressed with wavelengths for every power-carrying signal's frequency.

The theoretical power level that could be acquired in the free space with the selected antennas is shown for the 865.5MHz frequency for reference. This theoretical estimation is based on the Friis transmission formula shown in equation (4.1). Friis transmission Equation is used to characterize the behavior of free-space wireless signal transmission without addressing the properties of the wireless channel:

$$P_r = P_t + D_t + D_r + 20 \cdot log_{10}\left(\frac{\lambda}{4\pi d}\right) \quad (4.1)$$

where P_r is the power of the receiving antenna; P_t is the power of the transmitting antenna; D_t and D_r are the directivities of the corresponding antennas; λ is the wavelength; d is the distance between the antennas.

For the directional antenna, LP0410 Fig. 4.3 shows that the actually received power level in an enclosed space is much smaller for the antenna distance ranging from 1.7 to 5 wavelengths than directional antennas. The trend of received power decreasing with distance corresponds to what the theoretical curve demonstrates. However, for distances 5 to 8.6 wavelengths, the measured received power level coincides with the theoretical formula. At some of the measured wavelengths, for example, at 6.2 and 7.4 wavelengths, the signal frequency shows little impact on the received power level. As for the other distances, the results show that the signal's frequency that results in greater received power is strongly dependent on the antenna's position, which indicates that signals propagate differently in an enclosed space.

Measurement results with the directional antenna VERT900 in Fig 4.4 show that using an omnidirectional antenna for the WPT, the projected harvested power level trend in free space coincides with the experimental measurements. Although the harvested power levels follow the theoretical WPT harvested power levels in free space, there are high peaks at the distances of 0.7, 3.2,4.6, 5.1, and 7.5 wavelengths. In the measurements with the omnidirectional antenna, the harvested power level is strongly dependent on the signal's frequency, like in the case of the directional antenna. The highest power level at the antenna input was reached from 0.7 to 2.8, 5 to 8.6 wavelengths with 860 MHz signal frequency. However, in the range from 2.9 to 5 wavelengths, the 873 MHz signal's frequency provided the highest power level at the antenna input.

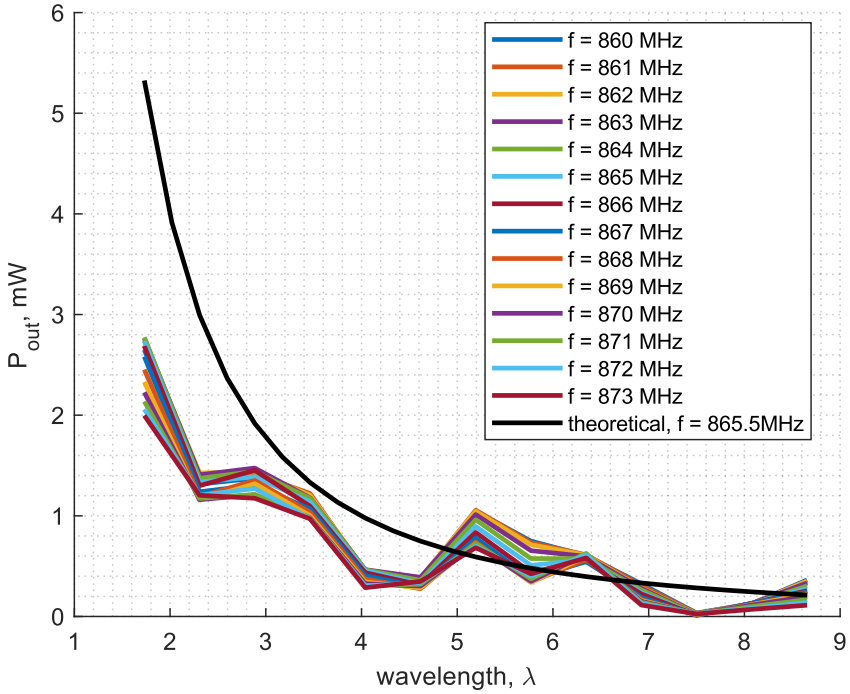

Fig. 4.3. WPT received power level depending on the central frequency using directional antennas LP0410.

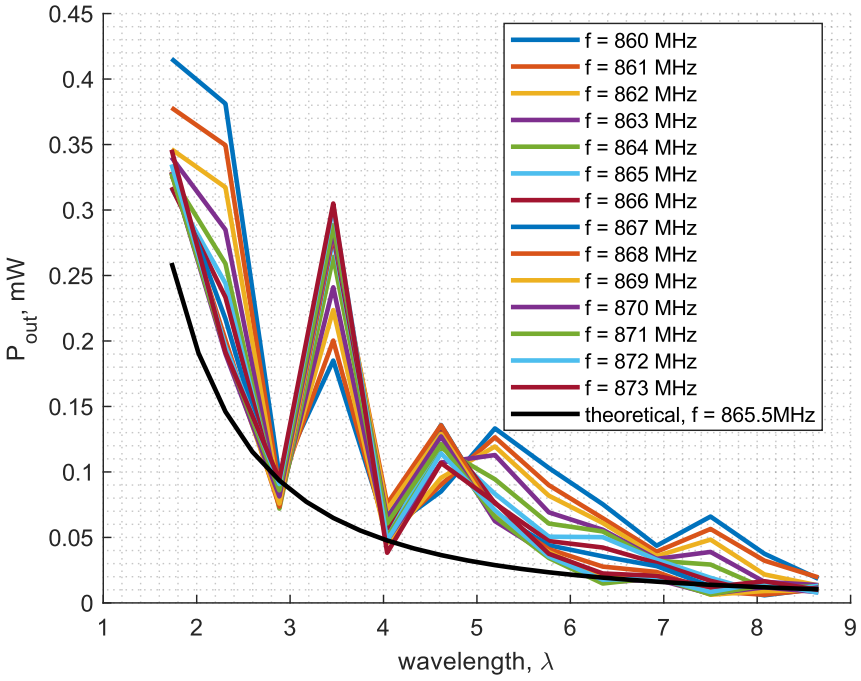

Fig. 4.4. WPT received power level depending on the central frequency using omnidirectional antennas VERT900.

The results of this study indicate that the model of the WPT system is more complex and cannot be precisely estimated by just the Friis transmission equation, as the received power varies with the placement of the antennas.

4.2.2 Signal waveform impact on the WPT efficiency

This subsection is dedicated to studying the signal waveform impact on WPT with different signals, such as multitone signals, tonally modulated FM signals, CHIRP and sine wave as the reference signal.

The results of the second study are presented in Figs. 4.5-4.10. Figure 4.5 shows the output voltage measurements of voltage doubler-based RF-DC converter's for the omnidirectional VERT900 and directional LP0410 antennas using LPAPR power-carrying signal with different numbers of subcarriers. The distances between the antennas are the same as in the previous study. Fig. 4.6 shows the same measurements done for the Powercast RF-DC converter. The sine wave results with the same carrier frequency and average power level are compared.

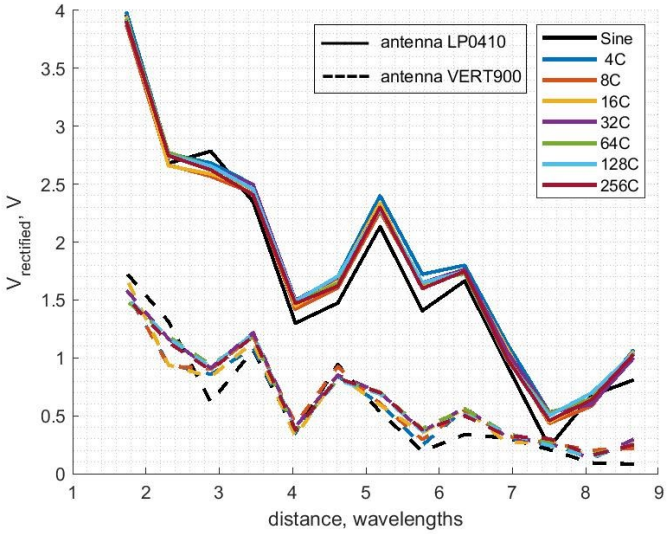

Fig. 4.5. The harvested voltage level of voltage doubler-based RF-DC converter with matching network for a different number of LPAPR subcarriers.

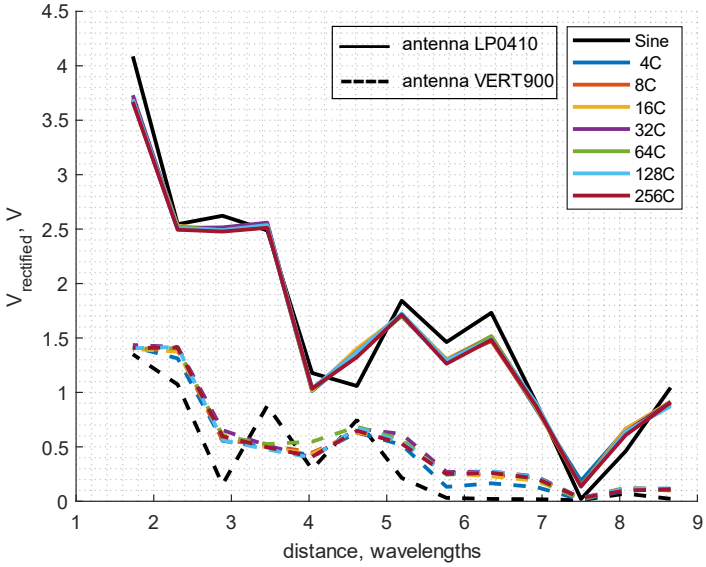

Fig. 4.6. The harvested voltage level of Powercast P2110B module for a different number of LPAPR subcarriers.

Fig. 4.6 demonstrates that using directional antennas produces a greater harvested voltage level than omnidirectional antennas. Different waveforms show no significant differences in the harvested voltage for distances < 2.2 wavelengths. With distances of more than 4 wavelengths, the LPAPR signals show a greater harvested voltage than the sine wave. For distances less than 4 wavelengths, the number of subcarriers has little effect on the harvested voltage. Using directional antennas with antenna distances of more than 4 wavelengths, the LPAPR signal with 4 subcarriers has greater harvested voltage than the waveforms with different numbers of subcarriers, although by a small amount. In the case of an omnidirectional antenna, the waveform that gives the highest amount of harvested voltage is different for each antenna placement.

Fig. 4.6 also confirms that the use of the directional antenna results in a greater amount of harvested voltage. Different waveforms showed no gain in harvested voltage over the sine wave power-carrying signal in the case of the directional antennas. In the case of the omnidirectional antennas, LPAPR with 16 subcarriers showed better performance than other waveforms.

The results in Fig. 4.5 and 4.6 show that the voltage doubler-based RF-DC converter demonstrates similar performance to the Powercast P2110B (with directional antennas). The voltage doubler shows superior performance for distances of more than 4 wavelengths. In the case of an omnidirectional antenna, the Powercast P2110B demonstrates the greater harvested voltage, although just for 16, 64, and 128 subcarriers.

Fig. 4.7 and 4.8 show the measurement results for the voltage doubler and Powercast using the RPAPR power-carrying signal waveform with different subcarrier numbers. The measurements for the sine wave are overlayed for comparison. Fig. 4.7 and 4.8 demonstrate that the RPAPR waveforms do not increase the harvested voltage compared to the sine wave when the distances between the antennas are less than 3 wavelengths. In Fig. 4.7, for distances above 4 wavelengths, the RPAPR multitone signals show increased performance, with 256 subcarriers showing the best performance (with directional antennas). Fig. 4.8 shows that the RPAPR multitone signal does not provide any advantages over the sine waveform for almost all distances, apart from the case of an omnidirectional antenna at 6 wavelengths distance.

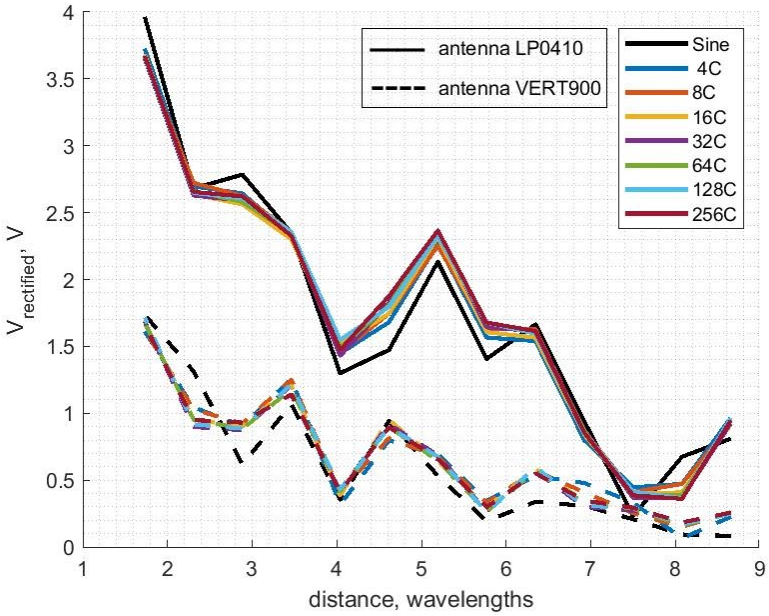

Fig. 4.7. The harvested voltage level of voltage doubler-based RF-DC converter with matching network for a different number of RPAPR subcarriers.

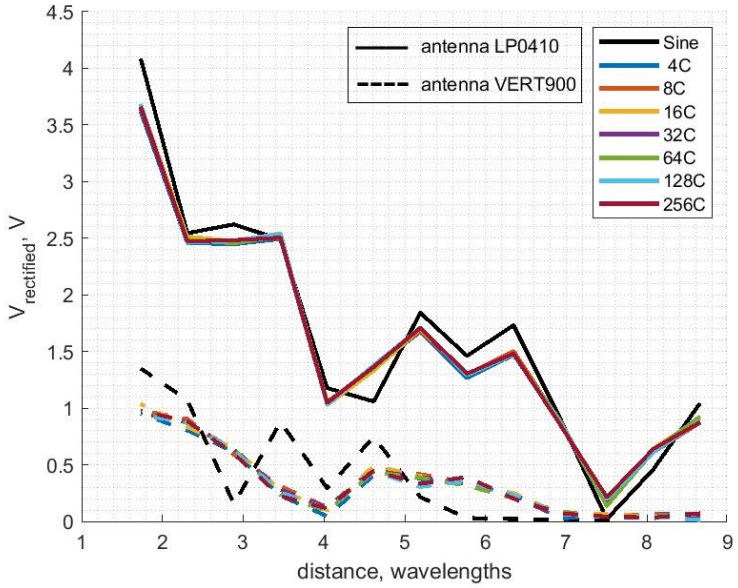

Fig. 4.8. The harvested voltage level of Powercast P2110B module for a different number of RPAPR subcarriers.

Fig. 4.7 and 4.8 also show that the two RF-DC converters perform similarly at close distances. At greater distances (more than 4 wavelengths), the voltage doubler-based RF-DC converter performs better than the Powercast P2110B.

Fig. 4.9 and 4.10 show the measurement results for the voltage doubler and Powercast using HPAPR power-carrying signal waveform with different subcarrier numbers. The measurements using HPAPR were done only for an omnidirectional antenna, as the use of a directional antenna exceeded the input power limitations of the RF-DC converters. In Fig. 4.9, the HPAPR multitone signals deliver significantly lower harvested voltage than a sine wave. However, Fig. 4.10 shows that HPAPR multitone signals benefit the amount of harvested voltage compared to the sine wave. The 8 subcarrier HPAPR signal gave the most voltage. For the HPAPR signals, the Powercast demonstrates better results than the voltage doubler-based RF-DC converter.

Comparing the results in Fig. 4.5-4.10, the LPAPR signal demonstrates better performance than other waveforms in the case of directional antennas. In comparison, the HPAPR shows better performance in the case of omnidirectional antennas.

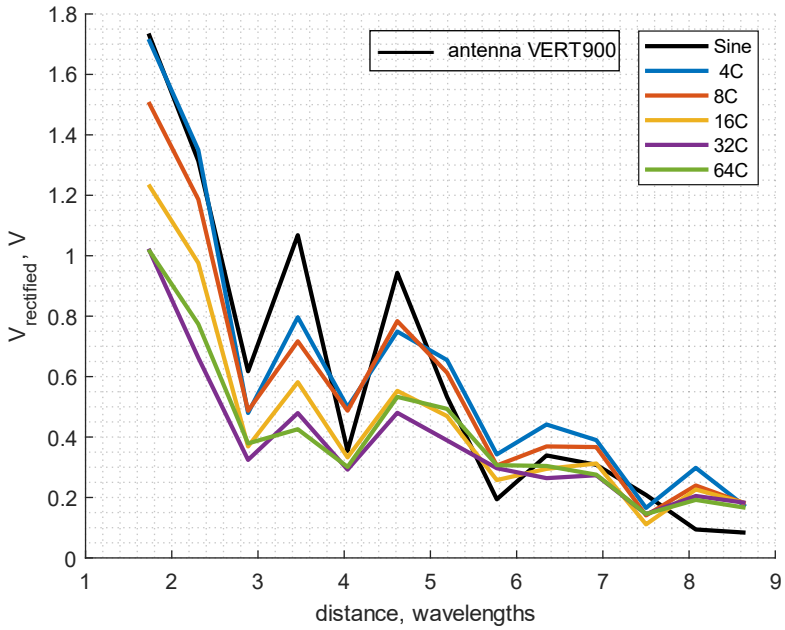

Fig. 4.9. The harvested voltage level of voltage doubler-based RF-DC converter with matching network for a different number of HPAPR subcarriers.

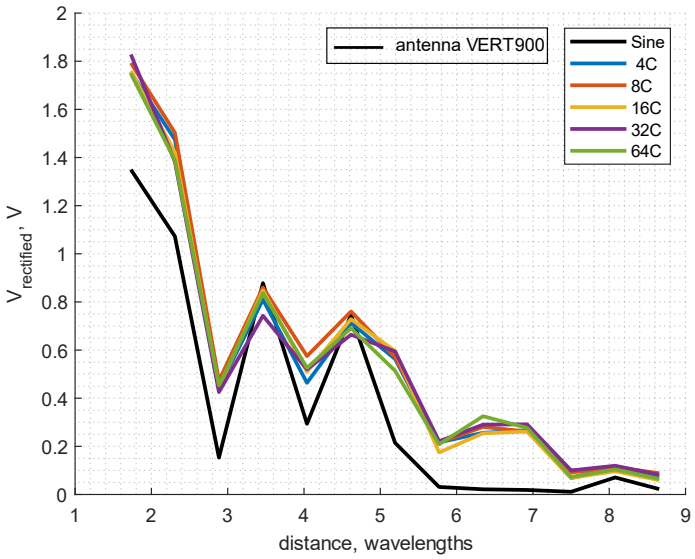

Fig. 4.10. The harvested voltage level of Powercast P2110B module for different number of HPAPR subcarriers.

4.2.3. Impact of constant envelope signal waveform on the WPT efficiency

This subsection is dedicated to the investigation of the converted voltage level in the WPT system depending on the different signal modulation with the same PAPR level and constant envelopes, such as the tonally modulated FM signals, CHIRP, and sine.

The results of the third study are compiled in Figs. 4.11-4.13. The distances between the antennas are measured in wavelengths, with a central frequency of 865.5MHz. Figure 4.18 shows the power level of the directional and omnidirectional antennas at antenna distances from

1.73 to 8.7 wavelengths. Results are presented for 4.8 (low) and 48 (high) FM modulation indexes and the same sine wave from the previous studies, taken for comparison. The results further approve that directional antennas are more beneficial for wireless power transfer applications, giving greater received power. Fig. 4.11 demonstrates that the FM signals give a similar received power as the sine waveform.

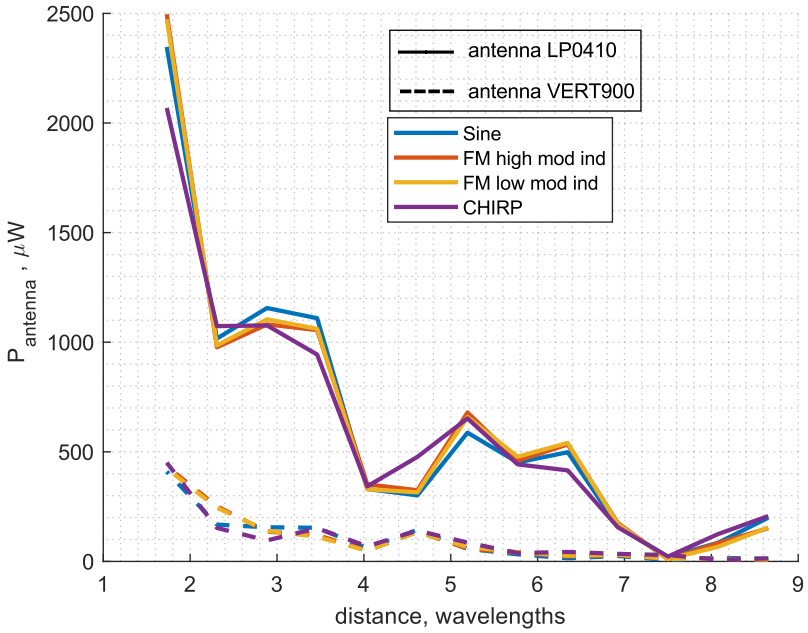

Fig. 4.11. Received average power level at the antennas' output depending on the WPT distance [91].

Figures 4.12 and 4.13 compare the WPT performance of the voltage doubler-based and Powercast RF-DC converters using directional (Figure 4.12) and omnidirectional (Figure 4.13) antennas. The results in Figures 4.12 and 4.13 also confirm that the FM modulated signals can be used for WPT with the same efficiency as sinusoidal signals giving additional opportunity to implement simultaneous information and power transmission (SWIPT). The results also show that the voltage doubler-based RF-DC converter performs better than the Powercast. In the case of the voltage doubler converter, the WPT performance with the CHIRP signal is similar to the FM modulated signals and sine waveform with both antenna types. The converted voltage in the case of the Powercast module shows a different situation, where the CHIRP signal waveform performs similarly to the other measured constant envelope signals.

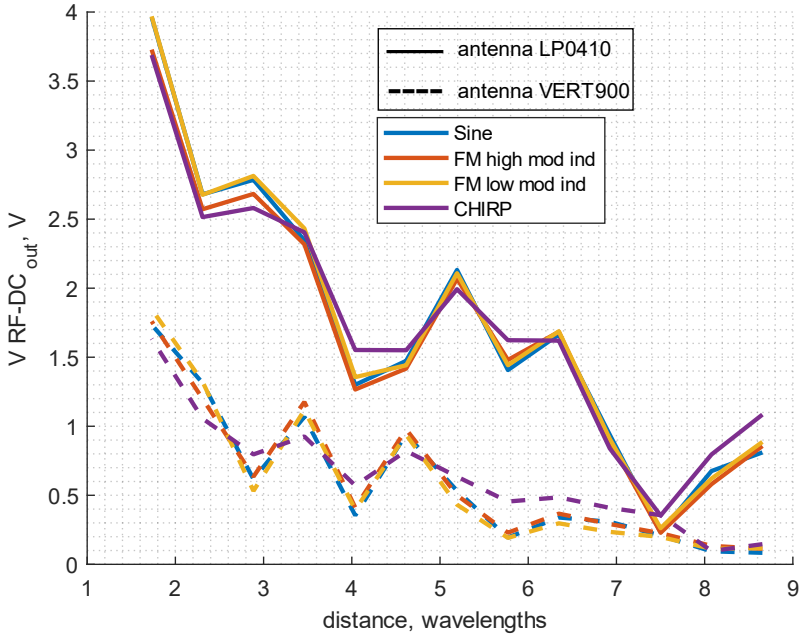

Fig. 4.12. Impact of WPT distance on the RF-DC converted voltage with the RF-DC voltage doubler with the matching network using constant envelope signals [91].

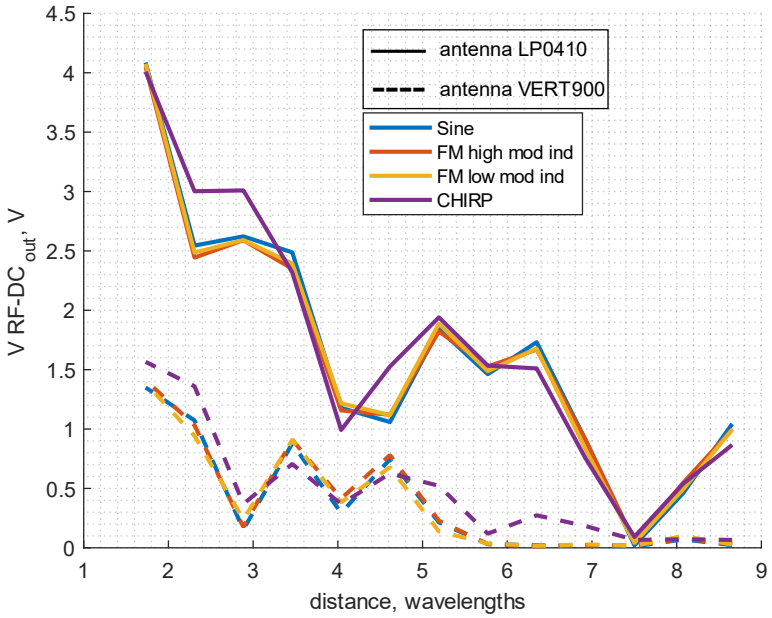

Fig. 4.13. Impact of WPT distance on the RF-DC converted voltage with the RF-DC converter Powercast P2110B module using constant envelope signals [91].

4.3. Conclusions of experimental study on WPT performance

The experimental studies provided in this section aimed to investigate wireless power transfer considering different parameters of power-carrying signals, different types of antennas and the distance between them in the case of a direct line of sight. For the study, the prototyped

RF-DC rectifiers voltage doubler and Powercast P2110B module have been used in ISM 863-870 MHz frequency range with directional and omnidirectional antennas.

The performed study showed the following:

- The use of more complex waveforms has particular benefits for WPT – the use of multicarrier signals allows for more efficient energy harvesting. In contrast, the use of FM signals opens possibilities for simultaneous information and power transmission.
- The level of the received average power on the harvester side has a dependence on the signal frequency, which could be explained by the difference in the multipath propagation for observed frequencies in ISM 863–870 MHz range for enclosed space.
- The voltage doubler-based RF-DC converter matches and even exceeds the performance of the commercially available Powercast P2110B RF-DC converter.
- The Friis equation does not provide sufficient approximation to estimate the average received power at the harvester side and evaluate WPT performance for enclosed space.
- The constant envelope signals with the exact power level yield a similar converted voltage level and, therefore, can be combined with SWIPT systems. The simultaneous data and power can be delivered to the needed device (sensor node).

Conclusions

Over the recent decade, the growing numbers of autonomous Wireless Sensor Nodes employed in the Internet of Things and the underlying Wireless Sensor Networks created a demand for alternative approaches for powering autonomous SNs. Such emerging technology that replaces the constant need for batteries in the operation of the SN is the RF Wireless Power Transfer.

This work was dedicated to the experimental study of the RF signal parameter impact on the RF-DC power conversion efficiency and the wireless power transfer performance. The main subject of research was the employment of the voltage doubler for wireless power transfer in ISM 863-870 MHz frequency range with different types of power-carrying signals.

The following tasks have been performed to reach the set goal:

- Theoretical analysis of the RF-DC rectifier, including the development of a model and the optimization of its parameters was performed.
- Prototypes for different RF-DC converter solutions were designed and fabricated.
- Experimental study on the RF-DC power conversion efficiency of the developed RF-DC converter modules, depending on the RF signal parameters was performed.
- Experimental study on the wireless power transfer performance of the developed RF-DC converter modules depending on the RF signal parameters and antenna type was performed.

The following RF-DC conversion efficiency optimization abilities have been investigated as a result of the research:

- The appropriate adjustment of the voltage doubler converter's load resistance to the number of subcarriers, in case of equal synphase multitone signals with uniformly distributed subcarriers, increase the power conversion efficiency.
- The exclusion of the matching network for the voltage doubler, applying equal synphase multitone signals with uniformly distributed subcarriers, increases the RF-DC power conversion efficiency.
- CHIRP signals, tonally modulated FM, and the amplitude modulated signals with PAPR level below 10dB provide equal power conversion efficiency.

The efficiency analysis of the different WPT signal waveforms has been performed and the results show that the application of the CHIRP, FM tonally modulated, and the amplitude modulated signals with PAPR level below 10dB in the case of the direct line of sight ensures the same WPT performance as a sine signal.

The obtained knowledge can be used for autonomous sensor node deployment, harvesting circuit topology optimization, as well as for estimation of the effect of a power-carrying signal waveform on the overall WPT system efficiency for an indoor environment use case.

Bibliography

[1] "Ericsson Mobility Report 2021," 2021. [Online]. Available: https://www.ericsson.com/492615/assets/local/reports-papers/mobility-report/documents/emr-quarterly2021-update.pdf.

[2] D. Pradeep Kumar Reddy and J. Mohana, *Wireless power transfer: Between Distance and Efficiency*, vol. 8, no. 4. 2016.

[3] The Institution of Engineering and Technology, *Wireless Power Transfer: Theory, technology, and applications*. Institution of Engineering and Technology, 2018.

[4] E. K. Hansen, G. G. Hammershoj Olesen, and M. Mullins, "Home smart home: A danish energy-positive home designed with daylight," *Proc. IEEE*, vol. 101, no. 11, pp. 2436–2449, 2013.

[5] J. Yang, Y. Kwon, and D. Kim, "Regional Smart City Development Focus: The South Korean National Strategic Smart City Program," *IEEE Access*, vol. 9, pp. 7193–7210, 2021.

[6] O. Elijah, T. A. Rahman, I. Orikumhi, C. Y. Leow, and M. N. Hindia, "An Overview of Internet of Things (IoT) and Data Analytics in Agriculture: Benefits and Challenges," *IEEE Internet Things J.*, vol. 5, no. 5, pp. 3758–3773, 2018.

[7] K. Shafique, B. A. Khawaja, F. Sabir, S. Qazi, and M. Mustaqim, "Internet of things (IoT) for next-generation smart systems: A review of current challenges, future trends and prospects for emerging 5G-IoT Scenarios," *IEEE Access*, vol. 8, pp. 23022–23040, 2020.

[8] D. Chen, N. Chen, X. Zhang, H. Ma, and Z. Chen, "Next-Generation Soil Moisture Sensor Web: High-Density in Situ Observation over NB-IoT," *IEEE Internet Things J.*, vol. 8, no. 17, pp. 13367–13383, 2021.

[9] K. Pallavi, J. D. Mallapur, and K. Y. Bendigeri, "Remote sensing and controlling of greenhouse agriculture parameters based on IoT," *2017 Int. Conf. Big Data, IoT Data Sci. BID 2017*, vol. 2018-Janua, pp. 44–48, 2018.

[10] A. Ahad, M. Tahir, and K. L. A. Yau, "5G-based smart healthcare network: Architecture, taxonomy, challenges and future research directions," *IEEE Access*, vol. 7, pp. 100747–100762, 2019.

[11] N. Ranjan, S. Bhandari, H. P. Zhao, H. Kim, and P. Khan, "City-wide traffic congestion prediction based on CNN, LSTM and transpose CNN," *IEEE Access*, vol. 8, pp. 81606–81620, 2020.

[12] J. Botero-Valencia, L. Castano-Londono, D. Marquez-Viloria, and M. Rico-Garcia, "Data reduction in a low-cost environmental monitoring system based on LoRa for WSN," *IEEE Internet Things J.*, vol. 6, no. 2, pp. 3024–3030, 2019.

[13] "2020 Ericson massive_iot_whitepaper.pdf." .

[14] X. Lu, P. Wang, D. Niyato, D. I. Kim, and Z. Han, "Wireless networks with rf energy harvesting: A contemporary survey," *IEEE Commun. Surv. Tutorials*, vol. 17, no. 2, pp. 757–789, 2015.

[15] M. A. Houran, X. Yang, and W. Chen, "Magnetically coupled resonance wpt: Review of compensation topologies, resonator structures with misalignment, and emi diagnostics," *Electron.*, vol. 7, no. 11, 2018.

[16] J. Eidaks, R. Kusnins, R. Babajans, D. Cirjulina, J. Semenjako, and A. Litvinenko, "Fast and Accurate Approach to RF-DC Conversion Efficiency Estimation for Multi-Tone Signals," *Sensors*, vol. 22, no. 3, p. 787, Jan. 2022.

[17] N. Shinohara, K. Nishikawa, T. Seki, and K. Hiraga, "Development of 24 GHz rectennas for fixed wireless access," *2011 30th URSI Gen. Assem. Sci. Symp. URSIGASS 2011*, pp. 3–6, 2011.

[18] W. S. High-impedance, “A 5 . 8-GHz Band Highly Efficient 1-W Rectenna,” vol. 69, no. 7, pp. 3558–3566, 2021.
[19] N. Singh, B. K. Kanaujia, M. T. Beg, Mainuddin, T. Khan, and S. Kumar, “A dual polarized multiband rectenna for RF energy harvesting,” *AEU - Int. J. Electron. Commun.*, vol. 93, no. February, pp. 123–131, 2018.
[20] Young-Ho Suh and Kai Chang, “A high-efficiency dual-frequency rectenna for 2.45- and 5.8-GHz wireless power transmission,” *IEEE Trans. Microw. Theory Tech.*, vol. 50, no. 7, pp. 1784–1789, Jul. 2002.
[21] C. Wang, B. Yang, and N. Shinohara, “Study and Design of a 2.45-GHz Rectifier Achieving 91% Efficiency at 5-W Input Power,” *IEEE Microw. Wirel. Components Lett.*, vol. 31, no. 1, pp. 76–79, 2021.
[22] T. C. Yo, C. M. Lee, C. M. Hsu, and C. H. Luo, “Compact circularly polarized rectenna with unbalanced circular slots,” *IEEE Trans. Antennas Propag.*, vol. 56, no. 3, pp. 882–886, 2008.
[23] Y. T. Chang, S. Claessens, S. Pollin, and D. Schreurs, “A Wideband Efficient Rectifier Design for SWIPT,” *2019 IEEE Wirel. Power Transf. Conf. WPTC 2019*, pp. 26–29, 2019.
[24] D. Wang and R. Negra, “Design of a dual-band rectifier for wireless power transmission,” *2013 IEEE Wirel. Power Transf. WPT 2013*, pp. 127–130, 2013.
[25] M. Ito *et al.*, “High efficient bridge rectifiers in 100MHz and 2.4GHz bands,” *IEEE Wirel. Power Transf. Conf. 2014, IEEE WPTC 2014*, pp. 64–67, 2014.
[26] J. H. Chou, D. B. Lin, K. L. Weng, and H. J. Li, “All polarization receiving rectenna with harmonic rejection property for wireless power transmission,” *IEEE Trans. Antennas Propag.*, vol. 62, no. 10, pp. 5242–5249, 2014.
[27] M. H. Ouda, P. Mitcheson, and B. Clerckx, “Robust Wireless Power Receiver for Multi-Tone Waveforms,” *2019 49th Eur. Microw. Conf. EuMC 2019*, pp. 101–104, 2019.
[28] C. Song, Y. Huang, J. Zhou, J. Zhang, S. Yuan, and P. Carter, “A high-efficiency broadband rectenna for ambient wireless energy harvesting,” *IEEE Trans. Antennas Propag.*, vol. 63, no. 8, pp. 3486–3495, 2015.
[29] F. Bolos, J. Blanco, A. Collado, and A. Georgiadis, “RF Energy Harvesting from Multi-Tone and Digitally Modulated Signals,” *IEEE Trans. Microw. Theory Tech.*, vol. 64, no. 6, pp. 1918–1927, Jun. 2016.
[30] A. Quddious, M. A. Antoniades, P. Vryonides, and S. Nikolaou, “Voltage-Doubler RF-to-DC Rectifiers for Ambient RF Energy Harvesting and Wireless Power Transfer Systems,” *Recent Wirel. Power Transf. Technol.*, pp. 1–19, 2020.
[31] A. Collado and A. Georgiadis, “Optimal waveforms for efficient wireless power transmission,” *IEEE Microw. Wirel. Components Lett.*, vol. 24, no. 5, pp. 354–356, 2014.
[32] S. A. Rotenberg, S. K. Podilchak, P. D. H. Re, C. Mateo-Segura, G. Goussetis, and J. Lee, “Efficient Rectifier for Wireless Power Transmission Systems,” *IEEE Trans. Microw. Theory Tech.*, vol. 68, no. 5, pp. 1921–1932, 2020.
[33] M. Terauds, L. Malbranque, and V. Smolaninovs, “Application of LoRaWAN for Interactive E-ink Based Schedule Board,” in *2020 IEEE Microwave Theory and Techniques in Wireless Communications (MTTW)*, 2020, pp. 222–226.
[34] A. Collado and A. Georgiadis, “Improving wireless power transmission efficiency using chaotic waveforms,” *IEEE MTT-S Int. Microw. Symp. Dig.*, pp. 1–3, 2012.
[35] A. Litvinenko, J. Eidaks, S. Tjukovs, D. Pikulins, and A. Aboltins, “Experimental Study of the Impact of Waveforms on the Efficiency of RF-to-DC Conversion Using a Classical Voltage Doubler Circuit,” in *2018 Advances in Wireless and Optical Communications (RTUWO)*, 2018, pp. 257–262.
[36] A. Litvinenko, J. Eidaks, and A. Aboltins, “Usage of signals with a high PAPR level for

efficient wireless power transfer," *2018 IEEE 6th Work. Adv. Information, Electron. Electr. Eng. AIEEE 2018 - Proc.*, pp. 5–9, 2018.
[37] J. Eidaks, A. Litvinenko, A. Aboltins, and D. Pikulins, "Signal Waveform Impact on Efficiency of Low Power Harvesting Devices in WSN," *Proc. 2019 IEEE Microw. Theory Tech. Wirel. Commun. MTTW 2019*, vol. 1, pp. 57–61, 2019.
[38] J. Eidaks, A. Litvinenko, J. P. Chiriyankandath, M. A. Varghese, D. D. Shah, and Y. K. T. Prathakota, "Impact of signal waveform on RF-harvesting device performance in wireless sensor network," *2019 IEEE 60th Annu. Int. Sci. Conf. Power Electr. Eng. Riga Tech. Univ. RTUCON 2019 - Proc.*, 2019.
[39] J. Eidaks, A. Litvinenko, A. Aboltins, and D. Pikulins, "Waveform Impact on Wireless Power Transfer Efficiency using Low-Power Harvesting Devices," *Electr. Control Commun. Eng.*, vol. 15, no. 2, pp. 96–103, 2019.
[40] K. Mitani, Y. Kawamura, W. Kitagawa, and T. Takeshita, "Circuit modeling for common mode noise on AC/DC converter using sic device," *2019 21st Eur. Conf. Power Electron. Appl. EPE 2019 ECCE Eur.*, pp. 1–10, 2019.
[41] D. Pikulin, "Complete bifurcation analysis of DC-DC converters under current mode control," *J. Phys. Conf. Ser.*, vol. 482, no. 1, 2014.
[42] D. Pikulins, "Exploring types of instabilities in switching power converters: The complete bifurcation analysis," *Elektron. ir Elektrotechnika*, vol. 20, no. 5, pp. 76–79, 2014.
[43] D. O. Pederson, "A historical review of circuit simulation," *IEEE Solid-State Circuits Mag.*, vol. 3, no. 2, pp. 43–54, 2011.
[44] H. Liu and N. Wong, "Autonomous volterra algorithm for steady-state analysis of nonlinear circuits," *IEEE Trans. Comput. Des. Integr. Circuits Syst.*, vol. 32, no. 6, pp. 858–868, 2013.
[45] G. De Luca, P. Bolcato, and W. H. A. Schilders, "Proper initial solution to start periodic steady-state-based methods," *IEEE Trans. Circuits Syst. I Regul. Pap.*, vol. 66, no. 3, pp. 1104–1115, 2019.
[46] X. Y. Z. Xiong, L. J. Jiang, J. E. Schutt-Aine, and W. C. Chew, "Volterra Series-Based Time-Domain Macromodeling of Nonlinear Circuits," *IEEE Trans. Components, Packag. Manuf. Technol.*, vol. 7, no. 1, pp. 39–49, 2017.
[47] N. N. Krylov, N.N.B.; Krylov, N.N.; Bogoliubov, *Introduction to Nonlinear Mechanics*. NJ, USA: Princeton University Press: Princeton, 1995.
[48] E. M. Baily, *Steady-State Harmonic Analysis of Non-Linear Networks*. Stanford, CA, USA: Stanford University: , USA, 1968.
[49] Q.-J. Zhang, E. Gad, B. Nouri, W. Na, and M. Nakhla, "Simulation and Automated Modeling of Microwave Circuits: State-of-the-Art and Emerging Trends," *IEEE J. Microwaves*, vol. 1, no. 1, pp. 494–507, 2021.
[50] M. S. Nakhla and J. Vlach, "A Piecewise Harmonic Balance Technique for Determination of Periodic Response of Nonlinear Systems," *IEEE Trans. Circuits Syst.*, vol. 23, no. 2, pp. 85–91, 1976.
[51] S. Egami, "Nonlinear, Linear Analysis and Computer-Aided Design of Resistive Mixers," *IEEE Trans. Microw. Theory Tech.*, vol. 22, no. 3, pp. 270–275, 1974.
[52] A. R. Kerr, "A Technique for Determining the Local Oscillator Waveforms in a Microwave Mixer," *IEEE Trans. Microw. Theory Tech.*, vol. 23, no. 10, pp. 828–831, 1975.
[53] R. G. Hicks and P. J. Khan, "Numerical Analysis of Nonlinear Solid-State Device Excitation in Microwave Circuits," *IEEE Trans. Microw. Theory Tech.*, vol. 30, no. 3, pp. 251–259, 1982.
[54] F. Filicori, M. R. Scalas, and C. Naldi, "Nonlinear circuit analysis through periodic

spline approximation," *Electron. Lett.*, vol. 15, no. 19, p. 597, 1979.
[55] P. D. Cooley, J.W.; Lewis, P.A.W.; Welch, *The Fast Fourier Transform and Its Applications*. IEEE Trans. Educ., 1969.
[56] M. B. Gilmore', R.J.; Steer2, *Nonlinear Circuit Analysis Using the Method of Harmonic Balance-A Review of the Art. Part I. Introductory Concepts.* Int. J. Microw. Millim. Wave Comput. Aided Eng., 1991.
[57] V. Rizzoli, A. Lipparini, and E. Marazzi, "A General-Purpose Program for Nonlinear Microwave Circuit Design," *IEEE Trans. Microw. Theory Tech.*, vol. 31, no. 9, pp. 762–770, 1983.
[58] V. Rizzoli, C. Cecchetti, and A. Lipparini, "A General-Purpose Program for the Analysis of Nonlinear Microwave Circuits Under Multitone Excitation by Multidimensional Fourier Transform," in *17th European Microwave Conference, 1987*, 1987, pp. 635–640.
[59] E. Ngoya, A. Suárez, R. Sommet, and R. Quéré, "Steady state analysis of free or forced oscillators by harmonic balance and stability investigation of periodic and quasi-periodic regimes," *Int. J. Microw. Millimeter-Wave Comput. Eng.*, vol. 5, no. 3, pp. 210–223, May 1995.
[60] M. Gourary, S. Ulyanov, M. Zharov, S. Rusakov, K. K. Gullapalli, and B. J. Mulvaney, "A robust and efficient oscillator analysis technique using harmonic balance," *Comput. Methods Appl. Mech. Eng.*, vol. 181, no. 4, pp. 451–466, Jan. 2000.
[61] M. M. Gourary, S. G. Rusakov, S. L. Ulyanov, and M. M. Zharov, "Improved harmonic balance technique for analysis of ring oscillators," in *2009 European Conference on Circuit Theory and Design*, 2009, pp. 327–330.
[62] Peng Li and L. T. Pileggi, "Efficient harmonic balance simulation using multi-level frequency decomposition," in *IEEE/ACM International Conference on Computer Aided Design, 2004. ICCAD-2004.*, pp. 677–682.
[63] W. Dong and P. Li, "Accelerating harmonic balance simulation using efficient parallelizable hierarchical preconditioning," in *Proceedings of the 44th annual conference on Design automation - DAC '07*, 2007, p. 436.
[64] Wei Dong and Peng Li, "Hierarchical Harmonic-Balance Methods for Frequency-Domain Analog-Circuit Analysis," *IEEE Trans. Comput. Des. Integr. Circuits Syst.*, vol. 26, no. 12, pp. 2089–2101, Dec. 2007.
[65] Wei Dong and Peng Li, "A Parallel Harmonic-Balance Approach to Steady-State and Envelope-Following Simulation of Driven and Autonomous Circuits," *IEEE Trans. Comput. Des. Integr. Circuits Syst.*, vol. 28, no. 4, pp. 490–501, Apr. 2009.
[66] L. Han, X. Zhao, and Z. Feng, "An efficient graph sparsification approach to scalable harmonic balance (HB) analysis of strongly nonlinear RF circuits," in *2013 IEEE/ACM International Conference on Computer-Aided Design (ICCAD)*, 2013, pp. 494–499.
[67] R. J. Gutmann and J. M. Borrego, "Power Combining in an Array of Microwave Power Rectifiers," in *MTT-S International Microwave Symposium Digest*, vol. 79, pp. 453–455.
[68] Jiapin Guo and Xinen Zhu, "An improved analytical model for RF-DC conversion efficiency in microwave rectifiers," in *2012 IEEE/MTT-S International Microwave Symposium Digest*, 2012, pp. 1–3.
[69] J. Guo, H. Zhang, and X. Zhu, "Theoretical Analysis of RF-DC Conversion Efficiency for Class-F Rectifiers," *IEEE Trans. Microw. Theory Tech.*, vol. 62, no. 4, pp. 977–985, Apr. 2014.
[70] T. Hirakawa and N. Shinohara, "Theoretical Analysis and Novel Simulation for Single Shunt Rectifiers," *IEEE Access*, vol. 9, pp. 16615–16622, 2021.
[71] N. Pan, D. Belo, M. Rajabi, D. Schreurs, N. B. Carvalho, and S. Pollin, "Bandwidth Analysis of RF-DC Converters Under Multisine Excitation," *IEEE Trans. Microw.*

Theory Tech., vol. 66, no. 2, pp. 791–802, Feb. 2018.
[72] T. Ohira, "Power efficiency and optimum load formulas on RF rectifiers featuring flow-angle equations," *IEICE Electron. Express*, vol. 10, no. 11, pp. 20130230–20130230, 2013.
[73] "PCBWAY Online PCB Quote." [Online]. Available: https://www.pcbway.com/orderonline.aspx.
[74] S. Hageman, "What PCB material do I need to use for RF?," *What PCB material do I need to use for RF?* [Online]. Available: https://www.edn.com/what-pcb-material-do-i-need-to-use-for-rf/.
[75] ROGERS CORPORATION, "RO4000 Series High Frequency Circuit Materials," 2018. [Online]. Available: https://rogerscorp.com/-/media/project/rogerscorp/documents/advanced-electronics-solutions/english/data-sheets/ro4000-laminates-ro4003c-and-ro4350b---data-sheet.pdf.
[76] "Silicon Schottky Diode: BAT63," 2003. [Online]. Available: https://www.infineon.com/dgdl/Infineon-BAT63SERIES-DS-v01_01-en.pdf?fileId=db3a304314dca38901151817843c0df4.
[77] Skyworks Solutions, "Surface Mount Mixer and Detector Schottky Diodes," *Datasheet*, 2018. [Online]. Available: https://www.skyworksinc.com/Products/Diodes/SMS7621-Series.
[78] "HSMS-285x Series Datasheet," *HSMS-285x Series Datasheet*. [Online]. Available: https://www.broadcom.com/products/wireless/diodes/schottky/hsms-285c. [Accessed: 30-Aug-2018].
[79] "HSMS-286x Series Datasheet." [Online]. Available: https://www.broadcom.com/products/wireless/diodes/schottky/hsms-286c. [Accessed: 30-Aug-2018].
[80] "Infineon BAT17 simulation parameters." [Online]. Available: https://www.infineon.com/dgdl/Infineon-Schottky-SPAR.zip-SM-v01_00-EN.zip?fileId=5546d46269e1c0190169ecdfa07c4744.
[81] "Powercast P2110B RF Powerharvester Receiver," *Powercast Corporation*, 2016. [Online]. Available: http://www.powercastco.com/wp-content/uploads/2016/12/P2110B-Datasheet-Rev-3.pdf. [Accessed: 27-Aug-2018].
[82] B. Clerckx and E. Bayguzina, "Low-Complexity Adaptive Multisine Waveform Design for Wireless Power Transfer," *IEEE Antennas Wirel. Propag. Lett.*, vol. 16, no. 1, pp. 2207–2210, 2017.
[83] R. Ibrahim *et al.*, "Novel Design for a Rectenna to Collect Pulse Waves at 2.4 GHz," *IEEE Trans. Microw. Theory Tech.*, vol. 66, no. 1, pp. 357–365, 2018.
[84] H. W. Pflug and H. J. Visser, *Wireless power transfer: Discrete rectifier modeling and analysis*. 2016.
[85] M. H. Ouda, P. Mitcheson, and B. Clerckx, "Optimal Operation of Multitone Waveforms in Low RF-Power Receivers," *2018 IEEE Wirel. Power Transf. Conf. WPTC 2018*, pp. 1–4, 2019.
[86] T. Hirakawa, C. Wang, and N. Shinohara, "RF-DC conversion efficiency improvement for microwave transmission with pulse modulation," *Wirel. Power Transf.*, vol. 6, no. 1, pp. 57–66, 2019.
[87] J. Eidaks, J. Sadovskis, A. Litvinenko, and D. Pikulins, "Experimental Analysis of LoRa Signals Employment for RF Energy Harvesting," *Proc. 2020 IEEE Work. Microw. Theory Tech. Wirel. Commun. MTTW 2020*, pp. 201–205, 2020.
[88] "P2110B 915 MHz RF Powerharvester Receiver," *Powercast Corporation*, 2016. [Online]. Available: http://www.powercastco.com/wp-content/uploads/2016/12/P2110B-Datasheet-Rev-3.pdf. [Accessed: 27-Aug-2018].

[89] A. Litvinenko, R. Kusnins, A. Aboltins, J. Eidaks, D. Laksis, and J. Sadovksis, “About Simultaneous Information and Power Transfer in WSN using Frequency Modulation,” in *2020 IEEE 8th Workshop on Advances in Information, Electronic and Electrical Engineering, AIEEE 2020 - Proceedings*, 2021.
[90] “P2110B 915 MHz RF Powerharvester,” 2016.
[91] A. Litvinenko, R. Kusnins, A. Aboltins, J. Eidaks, D. Laksis, and J. Sadovksis, “About Simultaneous Information and Power Transfer in WSN using Frequency Modulation,” *2020 IEEE 8th Work. Adv. Information, Electron. Electr. Eng. AIEEE 2020 - Proc.*, 2021.

Annex 1.

Matlab automated input power level and rectified DC voltage measurement script

```
clc;clear all;
close all;

%%   stop(timer_usrp_gain_OSC); stop(timer_measure_p);stop(timer_delayed_stop_simulink_OSC);
%%   stop(timer_usrp_gain_PSMU); stop(timer_measure_v);stop(stop_simulink_PSMU);
%% Signal parameter used as global variable.
global G_simulink G Vscale P PK_to_PK Scale V signal col gain_index timer_measure_p  timer_measure_v
enable_oscillocope
gain_index = 1;

enable_oscillocope = 0
enable_psmu        = 1
%% =======User input==============================%%
components = '';  % 3C9_10L
pcb = 'P1';  % 1 = HSMS285C doubler matched, 2 = HSMS285C doubler not matched, 3 = Powercast.
                    % 4 = HSMS285C doubler Rogers,  5 = SMS7630 doubler  6 = SMS7630 rectifier FR4, 7 =
HSMS2850 FR4 rectifier

%%
%% Oscilloscope GPIB comands ================================================
measurment_all = 'MEASUrement?' ;
meas1_get_Power_value = 'MEASUrement:MEAS8:VALue?' ;
meas1_get_Power_unit  = 'MEASUrement:MEAS8:UNIts?' ;
meas1_get_pk_pk_value = 'MEASUrement:MEAS5:VALue?' ;
meas1_get_CH1_scale  = 'CH1:SCAle?' ;
meas1_set_CH1_scale  = 'CH1:SCALE 33E-03' ;

%% gpib_init() ==============================================================
%  GPIB Initialization TETRONIX DPO72004C comands
% use tmtool to get device info
% Oscilloscope: File/recall/Power_measurement_2021.setup

%v1 = 1; % input variable for v.object
if (enable_oscillocope)
   v1 = instrfind('Type', 'visa-gpib', 'RsrcName', 'GPIB0::1::INSTR', 'Tag', '');
   if isempty(v1)
      v1 = visa('KEYSIGHT', 'GPIB0::1::INSTR');
   else
      fclose(v1);
      v1 = v1(1);
   end
   fopen(v1);
   %
   fprintf(v1, meas1_set_CH1_scale );
end
```

```
if (enable_psmu)
   v2 = instrfind('Type', 'visa-usb', 'RsrcName', 'USB0::0x0957::0x8B18::MY51143304::0::INSTR', 'Tag', '');
   if isempty(v2)
      v2 = visa('KEYSIGHT', 'USB0::0x0957::0x8B18::MY51143304::0::INSTR');
   else
      fclose(v2);
      v2 = v2(1);
   end
   fopen(v2);

      %% Instrument Configuration and Control----------------------------------
   set_reset          = '*RST' ;
   set_output_on      = ':OUTP ON' ;
   set_output_off     = ':OUTP OFF' ;
   set_voltage_mode   = ':SOUR:FUNC:MODE VOLT' ;
   set_current_mode   = ':SOUR:FUNC:MODE CURR' ;
   set_voltage_output = ':SOUR:VOLT 3' ;
   set_current_output = ':SOUR:CURR 1E-3' ;
   set_voltage_limit  = ':SENS:VOLT:PROT 10' ;
   set_current_limit  = ':SENS:CURR:PROT 1E-9' ;
   set_voltage_range  = ':SOUR:VOLT:RANG 20' ;
   set_voltage_auto   = ':SENS:VOLT:RANG:AUTO ON' ;
   set_current_auto   = ':SENS:CURR:RANG:AUTO ON' ;
   set_voltage_read   = ':SENS:FUNC ""VOLT""' ;
   set_voltage_read_measurement_time = ':SENS:VOLT:NPLC 1e-4'; % Measurement speed1 PLC (power
line cycle)
   set_voltage_read_aperture_time = ':SENS:VOLT:APER 1e-4';
   get_voltage        = ':MEAS:VOLT?' ;
   %% Instrument initialization and setup ----------------------------------
   fprintf(v2, set_reset);
   pause(1);
   fprintf(v2, set_current_mode);
   fprintf(v2, set_voltage_range);
   fprintf(v2, set_voltage_limit);
   fprintf(v2, set_current_limit);
   fprintf(v2, set_output_on);
   fprintf(v2, set_voltage_read);
   fprintf(v2, set_voltage_read_aperture_time);
   fprintf(v2, set_voltage_read_measurement_time);
   Voltage = [];
end

%% Carriers, GAIN  ============================================================
N = [4 8 16 32 64 128 256];
Gain_100uW = [245 335 460 647 922 1306]; % Pout = 100 uW. These gain values
% are for 4, 8, 16, 32, 64 and 128 tones for HPAPR signal
G_HPAPR = [  100    150 210 314 413 606    815    1150
          135  203       289       413       579       823    1091         1562
          130  194       288       406       571 818    1055  1544
```

```
            124  183      279      395      563      815    1184       1550
            11   219      366      546      809 1175          1294     1578
            13   220      368      546      775      1163     1306     1575
            38   181      338      500      731      1100     1275     1575 ];

    G_LPAPR = [ 106 151    214    309    437    621    784    1120
            140  201    280    410    580    820    1054       1510
            190  285    405    575    835    1178    1507     2140
            290  410    573    835    1190  1667    2140     3050
            410  595    828    1200         1706    2397     3090     4400
            510  740    1020       1495    2120    2980     3830     5430
            805  1175     1638     2360     3340     4790     6155     8750 ];

    G_RPAPR  = [236    352 511 711 1040   1394   1865   2750
            236   340     492      708      992    1404   1812         2672

            240   352     504      712      1012     1416     1868     2688

            240   352     504      712      1008     1412     1864     2684

            240   348     508      716      1012     1428     1848     2720

            244   356     504      720      1040     1468     1888     2720

            240   348     512      716      1024     1432     1848     2724 ];
    G_SINE = [ 260     405      580     800     1150     1680     2100     3000 ];

    % G_FMH = [ 0.03   0.0445 0.0635  0.0886  0.1285  0.18    0.2334  0.34 ];
    % G_FML = [ 0.0295 0.043  0.06    0.088   0.123   0.1755  0.222   0.32  ];
    %% Average INPUT POWER LEVELS
    PIN_HPAPR  = [18.294589e-6  40.072259e-6  76.767252e-6  162.73208e-6  292.99132e-6  623.26412e-6
1.1255963e-3 2.1310829e-3];

    P2P_HPAPR_V   = [211.5929e-3  305.94635e-3  411.95019e-3  590.8e-3  788.37795e-3  1.1652231  1.552
2.121723  ];

    PIN_LPAPR  = [20.053833e-6  38.827585e-6  75.394193e-6  162.68936e-6  310.16211e-6  657.08334e-6
996.89804e-6 2.1186961e-3];

    P2P_LPAPR_V   = [153.80001e-3  200.16389e-3  265.22072e-3  376.67561e-3  505.81641  731.42066e-3
892.6154e-3 1.3119003];

    PIN_RPAPR  = [19.553013e-6  39.541833e-6  85.052477e-6  163.35901e-6  329.19148e-6  624.26177e-6
1.1066305e-3 2.4134531e-3    ];
    P2P_RPAPR_V   = [158.88525e-3  215.7759e-3  301.47393e-3  404.17993e-3  559.87194e-3  766.25974e-3
1.0435556 1.5029059 ];

    PIN_SINE  = [      18.294589e-6  40.072259e-6  76.767252e-6  162.73208e-6  292.99132e-6  623.26412e-6
1.1255963e-3 2.1310829e-3];
    P2P_SINE_V = [  ];
```

```
PIN_SINE_SDR   = [ 20e-6   40e-6     80e-6    160e-6 320e-6   650e-6    1.01e-3   2.17e-3];
P2P_SINE_V_SDR = [ 131e-3  170e-3    233e-3   300e-3 404e-3   573e-3    707e-3    1.093 ];

%%  SCALE PARAMETERS ==========================================================
% Vscale_SINE =[ "15E-3" "23E-3" "27E-3" "36E-3" "44E-3" "60E-3" "80E-3" "120E-3" ];
Vscale_SINE =[   "200-3" "200-3" "200-3" "200-3" "200-3" "200-3" "200-3" "200-3"];
% Vscale_HPAPR =[ "30E-3" "51E-3" "68E-3" "95E-3" "135E-3" "195E-3" "248E-3" "355E-3"
%               "35E-3" "51E-3" "68E-3" "95E-3" "135E-3" "195E-3" "248E-3" "355E-3"
%               "35E-3" "51E-3" "65E-3" "95E-3" "135E-3" "195E-3" "238E-3" "340E-3"
%               "35E-3" "51E-3" "68E-3" "90E-3" "135E-3" "188E-3" "258E-3" "355E-3"
%               "9E-2"  "51E-3" "85E-3" "115E-3" "190E-3" "245E-3" "295E-3" "355E-3"
%               "9E-3"  "51E-3" "84E-3" "115E-3" "178E-3" "245E-3" "285E-3" "345E-3"
%               "1.3E-3" "51E-3" "82E-3" "112E-3" "160E-3" "245E-3" "295E-3"  "345E-3" ];

Vscale_HPAPR =[  "400E-3" "400E-3" "400E-3" "400E-3" "400E-3" "400E-3" "400E-3" "400E-3"
             "400E-3" "400E-3" "400E-3" "400E-3" "400E-3" "400E-3" "400E-3" "400E-3"
             "400E-3" "400E-3" "400E-3" "400E-3" "400E-3" "400E-3" "400E-3" "400E-3"
             "400E-3" "400E-3" "400E-3" "400E-3" "400E-3" "400E-3" "400E-3" "400E-3"
             "400E-3" "400E-3" "400E-3" "400E-3" "400E-3" "400E-3" "400E-3" "400E-3"
             "400E-3" "400E-3" "400E-3" "400E-3" "400E-3" "400E-3" "400E-3" "400E-3"
             "400E-3" "400E-3" "400E-3" "400E-3" "400E-3" "400E-3" "400E-3" "400E-3" ];

% Vscale_LPAPR =[ "20E-3" "27E-3" "35E-3" "50E-3" "66E-3" "95E-3" "115E-3" "170E-3"
%               "20E-3" "27E-3" "35E-3" "50E-3" "66E-3" "95E-3" "115E-3" "170E-3"
%               "20E-3" "27E-3" "35E-3" "50E-3" "66E-3" "95E-3" "115E-3" "170E-3"
%               "20E-3" "27E-3" "35E-3" "50E-3" "66E-3" "95E-3" "115E-3" "170E-3"
%               "20E-3" "27E-3" "35E-3" "50E-3" "66E-3" "95E-3" "115E-3" "170E-3"
%               "20E-3" "27E-3" "35E-3" "50E-3" "66E-3" "95E-3" "115E-3" "170E-3"
%               "20E-3" "27E-3" "35E-3" "50E-3" "66E-3" "95E-3" "115E-3" "170E-3" ];
Vscale_LPAPR =[  "200-3" "200-3" "200-3" "200-3" "200-3" "200-3" "200-3" "200-3"
             "200-3" "200-3" "200-3" "200-3" "200-3" "200-3" "200-3" "200-3"
             "200-3" "200-3" "200-3" "200-3" "200-3" "200-3" "200-3" "200-3"
             "200-3" "200-3" "200-3" "200-3" "200-3" "200-3" "200-3" "200-3"
             "200-3" "200-3" "200-3" "200-3" "200-3" "200-3" "200-3" "200-3"
             "200-3" "200-3" "200-3" "200-3" "200-3" "200-3" "200-3" "200-3"
             "200-3" "200-3" "200-3" "200-3" "200-3" "200-3" "200-3" "200-3" ];


% Vscale_RPAPR =[ "25E-3" "33E-3" "44E-3" "62E-3" "82E-3" "110E-3" "1580E-3" "220E-3"
%               "25E-3" "33E-3" "44E-3" "62E-3" "82E-3" "110E-3" "1580E-3" "220E-3"
%               "23E-3" "32E-3" "41E-3" "56E-3" "78E-3" "105E-3" "148E-3" "210E-3"
%               "27E-3" "37E-3" "50E-3" "70E-3" "92E-3" "135E-3" "175E-3" "250E-3"
%               "32E-3" "43E-3" "62E-3" "880E-3" "120E-3" "168E-3" "225E-3" "310E-3"
%               "30E-3" "41E-3" "56E-3" "80E-3" "110E-3" "156E-3" "205E-3" "280E-3"
%               "30E-3" "41E-3" "57E-3" "80E-3" "110E-3" "156E-3" "205E-3" "290E-3" ];
Vscale_RPAPR =[  "300-3" "300-3" "300-3" "300-3" "300-3" "300-3" "300-3" "300-3"
             "300-3" "300-3" "300-3" "300-3" "300-3" "300-3" "300-3" "300-3"
             "300-3" "300-3" "300-3" "300-3" "300-3" "300-3" "300-3" "300-3"
             "300-3" "300-3" "300-3" "300-3" "300-3" "300-3" "300-3" "300-3"
```

```
                "300-3" "300-3" "300-3" "300-3" "300-3" "300-3" "300-3" "300-3"
                "300-3" "300-3" "300-3" "300-3" "300-3" "300-3" "300-3" "300-3"
                "300-3" "300-3" "300-3" "300-3" "300-3" "300-3" "300-3" "300-3" ];

    % Vscale_FMH =[ "18E-3" "23E-3" "30E-3" "40E-3" "54E-3" "76E-3" "100E-3" "135E-3" ];
    % Vscale_FML =[ "21E-3" "27E-3" "35E-3" "50E-3" "70E-3" "95E-3" "125E-3" "170E-3" ];

    %% Timer setup ============================================================
    % t = 20 + 15*8 s = 140 seconds
    sampling_speed_OSC = 1 ;
    sampling_speed_PSMU = 2 ;
    measurement_samples_OSC = 10;
    measurement_samples_PSMU = 10;

    fprintf("\n measurement_samples = %i ;  % (5 for PSMU, 10 for Osc) \n\n",measurement_samples_OSC );
    measurement_delay  = 5;
    sim_delay = 22 ;
    sim_period_OSC  = measurement_delay + measurement_samples_OSC/sampling_speed_OSC  + 20 ;  %% +2 for osc ;+5 for psmu
    sim_period_PSMU = measurement_delay + measurement_samples_PSMU/sampling_speed_PSMU ;  %% +2 for osc ;+5 for psmu ~ 3
    sim_period_repetitions = 8;  %% 8 gain values for each carrier
    T_OSC = sim_period_OSC * sim_period_repetitions + measurement_delay;
    T_PSMU = sim_period_PSMU * sim_period_repetitions + measurement_delay;
    time_kill_simulation_OSC = sim_delay + T_OSC ;
    time_kill_simulation_PSMU = sim_delay + T_PSMU;  %155

    SIM_TIME_oscilloscope_minutes = time_kill_simulation_OSC*(7*3+1)/60
    SIM_TIME_PSMU_minutes = time_kill_simulation_PSMU*(7*3+1)/60
    %% Timers
    timer_usrp_gain_OSC = timer('StartDelay', sim_delay, 'Period', sim_period_OSC, 'TasksToExecute', sim_period_repetitions, 'ExecutionMode', 'fixedRate');
    timer_usrp_gain_OSC.TimerFcn = @(~,~)usrp_set_gain_measure_P(v1) %t.StartFcn = {@gpib_measure_power(v)}; % t.StopFcn = { @gpib_measure_power(v), 'My stop message'};
    timer_measure_p = timer('StartDelay', measurement_delay, 'Period', sampling_speed_OSC , 'TasksToExecute', measurement_samples_OSC, 'ExecutionMode', 'fixedRate');
    timer_measure_p.TimerFcn = @(~,~)measure_power(v1) %t.StartFcn = {@gpib_measure(v)}; % t.StopFcn = { @gpib_measure(v), 'My stop message'};


    timer_usrp_gain_PSMU = timer('StartDelay', sim_delay, 'Period', sim_period_PSMU, 'TasksToExecute', sim_period_repetitions, 'ExecutionMode', 'fixedRate');
    timer_usrp_gain_PSMU.TimerFcn = @(~,~)usrp_set_gain_measure_V(v2) %t.StartFcn = {@gpib_measure_power(v)}; % t.StopFcn = { @gpib_measure_power(v), 'My stop message'};



    timer_measure_v = timer('StartDelay', measurement_delay , 'Period', sampling_speed_PSMU/20 ,'TasksToExecute',measurement_samples_PSMU, 'ExecutionMode', 'fixedSpacing');
```

```
timer_measure_v.TimerFcn = @(~,~)measure_voltage(v2) %t.StartFcn = {@gpib_measure(v)}; % t.StopFcn = { @gpib_measure(v), 'My stop message'};


timer_delayed_stop_simulink_OSC = timer('StartDelay', time_kill_simulation_OSC, 'Period', 1, 'TasksToExecute', 1, 'ExecutionMode', 'singleShot');
timer_delayed_stop_simulink_OSC.TimerFcn = @(~,~)delayed_stop_simulink() %t.StartFcn = {@gpib_measure_power(v)}; % t.StopFcn = { @gpib_measure_power(v), 'My stop message'};

timer_delayed_stop_simulink_PSMU = timer('StartDelay', time_kill_simulation_PSMU, 'Period', 1, 'TasksToExecute', 1, 'ExecutionMode', 'singleShot');
timer_delayed_stop_simulink_PSMU.TimerFcn = @(~,~)delayed_stop_simulink() %t.StartFcn = {@gpib_measure_power(v)}; % t.StopFcn = { @gpib_measure_power(v), 'My stop message'};



%% Oscilloscope Measurements::::::::::::::::::::::::::::::::::::::::::::::::
if (enable_oscillocope)
   sdr_channel = 2;
   Pin_HPAPR= [];
   PK_HPAPR = [];
   Scale_HPAPR= [];
   Pin_LPAPR= [];
   PK_LPAPR = [];
   Scale_LPAPR= [];
   Pin_RPAPR= [];
   PK_RPAPR= [];
   Scale_RPAPR= [];
   Pin_SINE= [];
   PK_SINE = [];
   Scale_SINE= [];



   %% ============================ HPAPR SIGNAL ================================
   G = G_HPAPR;
   Vscale = Vscale_HPAPR;
   for col = 1:1:length(N)
      P = [];
      PK_to_PK=[];
      Scale = [];
      G_simulink = G(col,1); % Defines gain value
      signal = 'HPAPR'; % defines signal type
      stop(timer_usrp_gain_OSC); % Stops all timers, that will be needed next in code
      stop(timer_measure_p); % in case they are on
      SIG = repmat([1;zeros(N(col)-1,1)]+1j*eps,64,1)*20; % signal mattrix
      start(timer_usrp_gain_OSC);
      start(timer_delayed_stop_simulink_OSC); % starts a timer, which will stop simulink
```

```
    sim('auto_papr/AUTO_PAPR'); % starts simulink simulation
    figure(1)
    plot(P)
    Pin_HPAPR(col,:) = P;
    PK_HPAPR(col,:) = PK_to_PK;
    Scale_HPAPR(col,:) = Scale;
    plot(Pin_HPAPR(col,:));
end

%% % ============================ LPAPR SIGNAL ============================
G = G_LPAPR;
Vscale = Vscale_LPAPR;
for col = 1:length(N)
    P = [];
    PK_to_PK=[];
    Scale = [];
    G_simulink = G(col,1);
    signal = 'LPAPR';
    stop(timer_usrp_gain_OSC);
    stop(timer_measure_p);
    seq_Init = lteZadoffChuSeq(1,N(col)+1); % Uses Zadoff Chu Sequence to generate phases
    SEQ = ifft( seq_Init(1:N(col),1)); % inverse fast fourier transform
    SIG=(repmat(SEQ,64,1) * 20); % generates a signal matrix
    start(timer_usrp_gain_OSC);
    start(timer_delayed_stop_simulink_OSC);
    sim('auto_papr/AUTO_PAPR');
    Pin_LPAPR(col,:) = P;
    PK_LPAPR(col,:) = PK_to_PK;
    Scale_LPAPR(col,:) = Scale;
    plot(Pin_LPAPR(col,:));
end

%% ============================ RPAPR SIGNAL ============================
P = [];
PK_to_PK=[];
Scale = [];
G = G_RPAPR;
Vscale = Vscale_RPAPR;
for col = 1:length(N)
    P = [];
    PK_to_PK=[];
    Scale = [];
    G_simulink = G(col,1);
    signal = 'RPAPR';
    stop(timer_usrp_gain_OSC);
    stop(timer_measure_p);
    prev = rng(0,'v5uniform');
    randsig=(randn(N(col),1)+1j*randn(N(col),1)); % Generates random imgainary numbers
    randsig_norm=randsig/rms(randsig)/0.25; % ?????
    SIG  =  (repmat(randsig_norm,64,1)); % Defines signal matrix
```

```
    start(timer_usrp_gain_OSC);
    start(timer_delayed_stop_simulink_OSC);
    sim('auto_papr/AUTO_PAPR');
    Pin_RPAPR(col,:) = P;
    PK_RPAPR(col,:) = PK_to_PK;
    Scale_RPAPR(col,:) = Scale;
    plot(Pin_RPAPR(col,:));
end
%% ============================== SINE SIGNAL ================================
P = [];
PK_to_PK=[];
Scale = [];
gain_index = 1;
G = G_SINE;
Vscale = Vscale_SINE;
for col = 1:1
    P = [];
    PK_to_PK=[];
    Scale = [];
    G_simulink = G(col,1);
    signal = 'SINE';
    stop(timer_usrp_gain_OSC);
    SIG = [ones(256,1)]/10000;
    start(timer_usrp_gain_OSC);
    start(timer_delayed_stop_simulink_OSC);
    sim('auto_sine/AUTO_SINE');
    Pin_SINE(col,:) = P;
    PK_SINE(col,:) = PK_to_PK;
    Scale_SINE(col,:) = Scale;
    plot(Pin_SINE(col,:));
end

%% Saving data
%%
time = datestr(now, 'yyyy_mm_dd__HH_MM')
fname = sprintf('.\\data\\SDR_SIG__%s.mat', time);
save( fname,'Pin_HPAPR',   'PK_HPAPR',  'Scale_HPAPR','Pin_LPAPR', 'PK_LPAPR','Scale_LPAPR',...
          'Pin_RPAPR', 'PK_RPAPR',   'Scale_RPAPR',  'Pin_SINE',  'PK_SINE', 'Scale_SINE'     )

%% ---------------------------------------------------------------------
%% Close GPIB device

fclose(v1);
stop(timer_usrp_gain_OSC);
stop(timer_measure_p);
fprintf('Measurement finished!!  \n\n\n\n\n\n\n\n\n\n')
for i= 1 : 5
    beep
    pause(0.3)
end
```

```
end



%% PSMU MEASUREMENT----------------------------------------------------

if (enable_psmu)
   sdr_channel = 1;
   V_LPAPR = [];
   V_HPAPR = [];
   V_RPAPR = [];
   V_SINE  = [];
   % ============================= HPAPR SIGNAL ==============================
   gain_index = 1;
   G = G_HPAPR;
   for col = 1:length(N)
      V = [];
      G_simulink = G(col,1);
      signal = 'HPAPR';
      stop(timer_usrp_gain_PSMU);
      stop(timer_delayed_stop_simulink_PSMU);
      stop(timer_measure_v);
      SIG = repmat([1;zeros(N(col)-1,1)]+1j*eps,64,1)*20;
      start(timer_usrp_gain_PSMU);
      start(timer_delayed_stop_simulink_PSMU);
      sim('auto_papr/AUTO_PAPR');
      V_HPAPR(col,:) = V;
      plot(V_HPAPR(col,:));
   end
   % %% ============================= LPAPR SIGNAL ==========================
   gain_index = 1;
   G = G_LPAPR;
   for col = 1:length(N)
      V = [];
      G_simulink = G(col,1);
      signal = 'LPAPR';
      stop(timer_usrp_gain_PSMU);
      stop(timer_delayed_stop_simulink_PSMU);
      stop(timer_measure_v);
      seq_Init = lteZadoffChuSeq(1,N(col)+1);
      SEQ = ifft( seq_Init(1:N(col),1));
      SIG=(repmat(SEQ,64,1) * 20);
      start(timer_usrp_gain_PSMU);
      start(timer_delayed_stop_simulink_PSMU);
      sim('auto_papr/AUTO_PAPR');
      V_LPAPR(col,:) = V;
      plot(V_LPAPR(col,:));
    end
```

```
% ============================== RPAPR SIGNAL ================================
gain_index = 1;
G = G_RPAPR;
for col = 1:length(N)
   V = [];
   G_simulink = G(col,1);
   signal = 'RPAPR';
   stop(timer_usrp_gain_PSMU);
   stop(timer_delayed_stop_simulink_PSMU);
   stop(timer_measure_v);
   prev = rng(0,'v5uniform');
   randsig=(randn(N(col),1)+1j*randn(N(col),1));
   randsig_norm=randsig/rms(randsig)/0.25;
   SIG  =  (repmat(randsig_norm,64,1));
   start(timer_usrp_gain_PSMU);
   start(timer_delayed_stop_simulink_PSMU);
   sim('auto_papr/AUTO_PAPR');
   V_RPAPR(col,:) = V;
end
% ============================== SINE SIGNAL ================================
gain_index = 1;
G = G_SINE;
for col = 1:1
   V = [];
   G_simulink = G(1,1);
   signal = 'SINE';
   stop(timer_usrp_gain_PSMU);
   stop(timer_delayed_stop_simulink_PSMU);
   stop(timer_measure_v);
   SIG = [ones(256,1)]/10000;
   start(timer_usrp_gain_PSMU);
   start(timer_delayed_stop_simulink_PSMU);
   sim('auto_sine/AUTO_SINE');
   V_SINE(col,:) = V;
end
% ============================== SAVE TO FILE ================================
time = datestr(now, 'yyyy_mm_dd__HH_MM_SS') ;
fname = sprintf('.\\data\\%s_PAPR_%s___%s.mat',pcb,components, time);
save( fname,'V_HPAPR','V_LPAPR','V_RPAPR', 'V_SINE')
% Switch off measuring device, Close GPIB device-------------------------
fprintf(v2, set_output_off);
fclose(v2);
% --------------------------------------------------------------------------
%% Plot all signals
%%
figure(1)
sgtitle('HPAPR Voltage for all carriers')
for i = 1:7
subplot(7,1,i)
semilogy(V_HPAPR(i,:))
```

```
   xlabel('samples, x10'), ylabel('Voltage, V'); grid minor;
   title([sprintf('Carriers = %i', N(i) )]);
   xticks([0:10:80]);
   end

   figure(2)
   sgtitle('LPAPR Voltage for all carriers')
   for i = 1:7
   subplot(7,1,i)
   semilogy(V_LPAPR(i,:))
   xlabel('samples, x10'), ylabel('Voltage, V'); grid minor;
   title([sprintf('Carriers = %i', N(i) )]);
   xticks([0:10:80]);
   end

   figure(3)
   sgtitle('RPAPR Voltage for all carriers')
   for i = 1:7
   subplot(7,1,i)
   semilogy(V_RPAPR(i,:))
   xlabel('samples, x10'), ylabel('Voltage, V'); grid minor;
   title([sprintf('Carriers = %i', N(i) )]);
   xticks([0:10:80]);
   end
   figure(4)
   semilogy(V_SINE)
   xlabel('samples, x10'), ylabel('Voltage, V'); grid minor;
   title([sprintf('Sine SDR', N(i) )]);
   xticks([0:10:80]);

   %%
   R = 7500;
   stop(timer_usrp_gain_PSMU); %stop(timer_init_measurement_v);stop(timer_measure_v);


fprintf('Measurement finished!!  \n\n\n\n\n\n\n\n\n\n')
for i= 1 : 5
   beep
   pause(0.3)
end
end


%% gpib_measure(v)-----------------------------------------------------------------------------------------------
function usrp_set_gain_measure_P(v1)
global G G_simulink Vscale col gain_index timer_measure_p enable_oscillocope signal
if (gain_index > length(G) ) % makes sure gain_index doesn't exceed gain value in G matrix
   gain_index = 1;
end
if (enable_oscillocope)
```

```
        meas1_set_CH1_scale =  sprintf('CH1:SCALE %s',Vscale(col,gain_index));
        fprintf(v1, meas1_set_CH1_scale );
    end
    G_simulink = G(col,gain_index);
    fprintf(' G_sim = %i, col = %i, gain_index= %i, %s \n',G_simulink, col, gain_index, signal)
    if (strcmp(signal,'SINE'))
        set_param('AUTO_SINE/Slider Gain', 'Gain','G_simulink'); % Changes Slider Gain value in Simulink model (AUTO_PAPR) to G_simulink
        set_param('AUTO_SINE', 'SimulationCommand', 'update'); % set_param('modelname', 'SimulationCommand', 'update'
    else
        set_param('AUTO_PAPR/Slider Gain', 'Gain','G_simulink'); % Changes Slider Gain value in Simulink model (AUTO_PAPR) to G_simulink
        set_param('AUTO_PAPR', 'SimulationCommand', 'update'); % set_param('modelname', 'SimulationCommand', 'update')
    end
    gain_index = gain_index+1;
    start(timer_measure_p); % Function: measure_power
    end

    function measure_power(v1)
    global P PK_to_PK Scale
    meas1_get_Power_value = 'MEASUrement:MEAS8:VALue?' ;
    meas1_get_pk_pk_value = 'MEASUrement:MEAS5:VALue?' ;
    meas1_get_CH1_scale  = 'CH1:SCAle?' ;
    read_P = str2double(query(v1, meas1_get_Power_value));
    P = [P read_P];
    read_PK_to_PK =str2double(query(v1, meas1_get_pk_pk_value));
    PK_to_PK = [PK_to_PK read_PK_to_PK];
    read_Scale = str2double(query(v1, meas1_get_CH1_scale));
    Scale = [Scale read_Scale];
    plot(P);
    fprintf('P_RMS = %d W, Peak to Peak = %d, Vscale = %d, Scale = %2.f percent \n', read_P,read_PK_to_PK, read_Scale ,100*read_PK_to_PK/(10*read_Scale))
    end

    function usrp_set_gain_measure_V(v2)
    global G G_simulink col gain_index signal timer_measure_v signal
    if (gain_index > length(G) )
        gain_index = 1;
    end
    G_simulink = G(col,gain_index);
    fprintf(' G_sim = %i, col = %i, gain_index= %i, %s \n',G_simulink, col, gain_index, signal)
    if (strcmp(signal,'SINE'))
        set_param('AUTO_SINE/Slider Gain', 'Gain','G_simulink'); % Changes Slider Gain value in Simulink model (AUTO_PAPR) to G_simulink
        set_param('AUTO_SINE', 'SimulationCommand', 'update'); % set_param('modelname', 'SimulationCommand', 'update'
    else
```

```
        set_param('AUTO_PAPR/Slider Gain', 'Gain','G_simulink'); % Changes Slider Gain value in Simulink model (AUTO_PAPR) to G_simulink
        set_param('AUTO_PAPR', 'SimulationCommand', 'update'); % set_param('modelname', 'SimulationCommand', 'update')
    end
        gain_index = gain_index+1;
    start(timer_measure_v); % Function: measure_voltage
    end

    function measure_voltage(v2)
        global V
        read_V = str2double(query(v2, ':MEAS:VOLT?'));
        V = [V ; read_V];
        fprintf('V = %d V \n', read_V)
            plot(V);
    end

    function delayed_stop_simulink()
    global signal
    if (strcmp(signal,'SINE'))
        set_param('AUTO_SINE', 'SimulationCommand', 'stop');
    else
        set_param('AUTO_PAPR', 'SimulationCommand', 'stop');
    end
    end

    %%  stop(timer_usrp_gain_PSMU); stop(timer_measure_v);stop(stop_simulink_PSMU);
```

Annex 2.

RF-DC rectifier Received input power measurement script

```
% clc;clear all;
% close all;
global P PK_to_PK Scale  gain_index col
% P = [];  PK_to_PK = []; Scale = [];
gain_index = 1;
col =1;

%%                                    BPIB                                    comands
============================================================
measurment_all = 'MEASUrement?' ;
meas1_get_Power_value = 'MEASUrement:MEAS8:VALue?' ;
meas1_get_Power_unit  = 'MEASUrement:MEAS8:UNIts?' ;
meas1_get_pk_pk_value = 'MEASUrement:MEAS5:VALue?' ;
meas1_get_CH1_scale  = 'CH1:SCAle?' ;
meas1_set_CH1_scale  = 'CH1:SCALE 400E-03' ;

%%                                                                    gpib_init()
==========================================6=====================
%  GPIB Initialization TETRONIX DPO72004C comands
% use tmtool to get device info
% Oscilloscope: File/recall/Power_measurement_2021.setup
v1 = instrfind('Type', 'visa-gpib', 'RsrcName', 'GPIB0::1::INSTR', 'Tag', '');
if isempty(v1)
   v1 = visa('KEYSIGHT', 'GPIB0::1::INSTR');
else
   fclose(v1);
   v1 = v1(1);
end
fopen(v1);
% k = 10; P= P(1:10*k); PK_to_PK = PK_to_PK(1:10*k); Scale  = Scale(1:10*k);
tic
set_correct_Vdiv(v1);
pause(2)
for i = 1:10
measure_power(v1)
pause(1)
end
% P = []; PK_to_PK =  []; Scale =  [];
```

```
fprintf(v1,  'CH1:SCALE 400E-03' );
toc

plot(P)
% N = length(P)/400
%signal = 'FMH' ;
%signal = 'NOISE_C'
signal = 'SINE';
%signal = 'CHIRP'
pcb = '';  %  --

time = datestr(now, 'yyyy_mm_dd__HH_MM_SS')
fname = sprintf('WPT_%s_received_A2_%s_%s.mat',pcb, signal, time);
% save( fname,'P', 'PK_to_PK', 'Scale')

%% ---------------------------------------------------------------------------------------------------
%% Close GPIB device
fclose(v1);
for i =1:3
   beep
   pause(0.3)
end

%% gpib_measure(v)-------------------------------------------------------------------------------------
------------
function set_correct_Vdiv(v1)
fprintf(v1, 'CH1:SCALE 400E-03');
pause(1.5);
meas1_get_pk_pk_value = 'MEASUrement:MEAS5:VALue?' ;
fprintf(v1, meas1_get_pk_pk_value);
current_peak_to_peak = str2double(fscanf(v1))/10*1.1;
var = (split(sprintf('%d ', current_peak_to_peak)));  %  aa= char(SC(1,1)); [aa(1:10) aa(12)]
meas1_set_scale=  sprintf('CH1:SCALE %s',char(var(1,1)') )
fprintf(v1, meas1_set_scale );
end

function measure_power(v1)
global P PK_to_PK Scale
meas1_get_Power_value = 'MEASUrement:MEAS8:VALue?' ;
meas1_get_pk_pk_value = 'MEASUrement:MEAS5:VALue?' ;
meas1_get_CH1_scale  = 'CH1:SCAle?' ;
fprintf(v1, meas1_get_Power_value);
```

```
read_P = str2double(fscanf(v1));
P = [P read_P];
fprintf(v1, meas1_get_pk_pk_value);
read_PK_to_PK = str2double(fscanf(v1));
PK_to_PK = [PK_to_PK read_PK_to_PK];
fprintf(v1, meas1_get_CH1_scale );
read_Scale = str2double(fscanf(v1));
Scale = [Scale read_Scale];
plot(P);
%for i= 1:length(P)
fprintf('P_RMS = %d W, Peak to Peak = %d, Vscale = %d, Scale = %2.f percent \n',...
read_P,read_PK_to_PK, read_Scale ,100*read_PK_to_PK/(10*read_Scale))
%end
end
```

Annex 3.

RF-DC rectifier Voltage measurement script

```
%close all
    %% Setup
    v2 = instrfind('Type', 'visa-usb', 'RsrcName', 'USB0::0x0957::0x8B18::MY51143304::0::INSTR', 'Tag', '');
    if isempty(v2)
       v2 = visa('KEYSIGHT', 'USB0::0x0957::0x8B18::MY51143304::0::INSTR');
    else
       fclose(v2);
       v2 = v2(1);
    end
    fopen(v2);

    set_reset          = '*RST' ;
    set_output_on      = ':OUTP ON' ;
    set_output_off     = ':OUTP OFF' ;
    set_voltage_mode   = ':SOUR:FUNC:MODE VOLT' ;
    set_current_mode   = ':SOUR:FUNC:MODE CURR' ;
    set_voltage_output = ':SOUR:VOLT 3' ;
    set_current_output = ':SOUR:CURR 1E-3' ;
    set_voltage_limit  = ':SENS:VOLT:PROT 10' ;
    set_current_limit  = ':SENS:CURR:PROT 1E-9' ;
    set_voltage_range  = ':SOUR:VOLT:RANG 20' ;
    set_voltage_auto   = ':SENS:VOLT:RANG:AUTO ON' ;
    set_current_auto   = ':SENS:CURR:RANG:AUTO ON' ;
    set_voltage_read   = ':SENS:FUNC ""VOLT""' ;
    set_voltage_read_measurement_time = ':SENS:VOLT:NPLC 1e-4'; % Measurement speed1 PLC (power line cycle)
    set_voltage_read_aperture_time = ':SENS:VOLT:APER 1e-4';
    get_voltage        = ':MEAS:VOLT?' ;
    get_current        = ':MEAS:CURR?' ;

    %% Init intrument
    fprintf(v2, set_reset);
    pause(1);
    fprintf(v2, set_current_mode);
```

```
    fprintf(v2, set_voltage_range);
    fprintf(v2, set_voltage_limit);
    fprintf(v2, set_current_limit);
    fprintf(v2, set_output_on);
    fprintf(v2, set_voltage_read);
    fprintf(v2, set_voltage_read_aperture_time);
    fprintf(v2, set_voltage_read_measurement_time);
    samples = 400

    %% Measurement
    % V = [];
    A = exist('V')  ;
    if not(A)
       V = [];
    end

    tic
    for i = 1:samples
    fprintf(v2, get_voltage);
    read_V = str2double(fscanf(v2));
    V = [V  read_V];
    fprintf('V = %d V \n', read_V)
    plot(V, 'Linewidth', 2);
    pause(1e-3)
    end
    toc

    for i = 1:1:4
    beep
    pause(0.3)
    end

    %  k = 3; V = V(1:400*k);

    fprintf('\n[\b<strong> ========================================== </strong>
]\b \n');
    N = length(V)/samples;
    av(V,samples)
    %signal = 'LPAPR_256'
    %signal = 'NOISE_64C'
    signal = 'SINE'
    antena = 'A2' ; % A1 directional, A2 omni-directional
```

```
pcb = 'P3';
time = datestr(now, 'yyyy_mm_dd__HH_MM_SS');
fname = sprintf('WPT_%s_%s_%s__2PA_%s.mat', pcb, signal, antena,  time);
% save( fname,'V')
```